# Cloud Condensation Nuclei and Ice-Nucleating Particles over the Southern Ocean: Abundance and Properties during the Antarctic Circum-navigation Expedition

Von der Fakultät für Physik und Geowissenschaften
der Universität Leipzig
genehmigte

D I S S E R T A T I O N

zur Erlangung des akademischen Grades

Doktor der Meteorologie
Dr. rer. nat.

vorgelegt

von Christian Tatzelt, M.Sc. Meteorologie
geboren am 12.09.1991 in Leipzig

Gutachter: Prof. Dr. Mira Pöhlker
Prof. Dr. Zhijun Wu

Tag der Verleihung: 24.04.2023

**Bibliographische Beschreibung**

**Wolkennukleationskeime und Eiskeime über dem Südlichen Ozean: Anzahl und Eigenschaften während der „Antarctic Circum-navigation Expedition"**
Tatzelt, Christian
Universität Leipzig, Dissertation
106 Seiten, 137 Literaturzitate, 43 Abbildungen, 4 Tabellen, 4 Anlagen.

**Referat**  Aerosolpartikel, die als Wolkennukleations- oder Eiskeime fungieren, spielen eine Schlüsselrolle in den Entstehungs- und Vereisungsprozessen von Wolken. Mit ihren wolkenrelevanten Eigenschaften haben diese beiden Arten von Aerosolpartikeln einen starken Einfluss auf den Strahlungshaushalt der Erde. Messungen ihrer Häufigkeit und Eigenschaften sind selten, inbesondere in den entlegenen Regionen der Erde wie beispielsweise dem Südlichen Ozean.

In dieser Arbeit werden die Ergebnisse von in situ und filterbasierten Partikelmessungen einer Forschungsfahrt auf dem Südlichen Ozean in den Sommermonaten der Südhalbkugel gezeigt. Ein erstmaliger Überblick über die Anzahlkonzentrationen der Wolkennukleations- und Eiskeime über dem Südlichen Ozean wird gegeben. Unter Berücksichtigung weiterer Messergebnisse zur chemischen Zusammensetzung der Partikel und Betrachtungen zur Herkunft der Luftmassen werden Rückschlüsse auf die Herkunft und Quellen der gesammelten, wolkenrelevanten Aerosolpartikel gezogen, auch mit Hilfe einer Korrelationsanalyse.

Die Anzahlkonzentration der Wolkennukleationskeime schwankte innerhalb von zwei Größenordnungen, beispielsweise zwischen 3 und 590 cm$^{-3}$ bei 0.3 % Übersättigung. Die chemische Zusammensetzung der Wolkennukleationskeime variierte dabei stark, zwischen organischem und inorganischem Material. Der Hygroskopizitätsparameter zeigte keine Größenabhängigkeit, was für eine intern gemischte Population von Wolkennukleationskeimen spricht (kritische Partikeldurchmesser lagen im Mittel zwischen 30 und 110 nm). Der prozentuale Anteil von Seesalzpartikeln zur Anzahlkonzentration der Wolkennukleationskeime war im Mittel gering (kleiner 35 %).

Die Anzahlkonzentration der Eiskeime wurden im Temperaturbereich −4 bis −27 °C mittels einer filterbasierten Immersionsgefriermethode bestimmt. Die Anzahlkonzentrationen schwankten dabei im Bereich von bis zu drei Größenordnungen, beispielsweise zwischen 0.2 und 100 m$^{-3}$ bei einer Temperatur von −16 °C. In Küstennähe, mit Ausnahme von Antarktika, wurden erhöhte Anzahlkonzentrationen (über 10 m$^{-3}$ bei −16 °C) gemessen. Niedrigere, weniger variable Anzahlkonzentrationen wurden hingegen auf offener See gemessen. Diese Beobachtungen, zusammen mit den Ergebnissen zur Luftmassenherkunft, sprechen für eine Dominanz von terrestrischen und/oder küstennahen Quellen der Eiskeime in der Nähe von eisfreiem (nicht-Antarktischem) Festland. Dabei können in den unberührten, marinen Regionen die Eiskeime aus dem Meer selbst und/oder Ferntransport stammen.

Eine Korrelationsanalyse zeigte einen starken Zusammenhang zwischen der Massenkonzentration von Natrium und der Anzahlkonzentration an groben Aerosolpartikeln (größer 1 µm). Daraus folgt ein signifikanter Anteil an Seesalzpartikeln in dieser Partikelgröße. Die Anzahlkonzentration der Wolkennukleationskeime korrelierte stark mit den Anzahlkonzentrationen der Aitken- (10 bis 100 nm) bzw. Akkumulationskerne (100 bis 1000 nm). Diese Beobachtung, zusammen mit dem Fehlen einer Korrelation zwischen Natriummasse und Aitken- oder Akkumulationskernanzahl, unterstreicht die Relevanz von Partikeln die nicht Seesalz sind (vermutlich sekundär geformten Aerosolpartikel) für die Population der Wolkennukleationskeime.

**Bibliographic description**

**Cloud Condensation Nuclei and Ice-Nucleating Particles over the Southern Ocean: Abundance and Properties during the Antarctic Circum-navigation Expedition**
Tatzelt, Christian
Leipzig University, dissertation
106 pages, 137 references, 43 figures, 4 tables, 4 appendices.

**Abstract**  Aerosol particles acting as cloud condensation nuclei (CCN) or ice nucleating particles (INP) play a major role in the formation and glaciation of clouds. Thereby they exert a strong impact on the radiation budget of the Earth. Data on abundance and properties of both particle types are sparse, especially for remote areas of the world, such as the Southern Ocean (SO).
In this work, unique results from ship-borne aerosol-particle-related in situ measurements and filter sampling in the summertime SO region are presented. An overview of CCN and INP number concentrations on the Southern Ocean is provided and, using additional analyses on particle chemical composition and air-mass origin, insights regarding possible CCN and INP sources and origins are presented, with the help of a correlation analysis.
CCN number concentrations spanned 2 orders of magnitude, e.g. for a supersaturation of $0.3\,\%$ values ranged roughly from 3 to $590\,\mathrm{cm^{-3}}$. CCN showed variable contributions of organic and inorganic material. No distinct size-dependence of the CCN hygroscopicity parameter was apparent, indicating homogeneous composition across sizes (critical dry diameter on average between $30\,\mathrm{nm}$ and $110\,\mathrm{nm}$). The relative contribution of sea spray aerosol (SSA) to the CCN number concentration was on average small (below $35\,\%$).
Ambient INP number concentrations were measured in the temperature range from $-4$ to $-27\,^\circ\mathrm{C}$ using an immersion freezing method. Concentrations spanned up to 3 orders of magnitude, e.g. at $-16\,^\circ\mathrm{C}$ from 0.2 to $100\,\mathrm{m^{-3}}$. Elevated values (above $10\,\mathrm{m^{-3}}$ at $-16\,^\circ\mathrm{C}$) were measured when the research vessel was in the vicinity of land (excluding Antarctica). Lower, more constant concentrations were measured on the open ocean. This, along with results of backward-trajectory analyses, hints towards terrestrial and/or coastal INP sources being dominant close to ice-free (non-Antarctic) land. In pristine marine areas INP may originate from both oceanic sources and/or long range transport. A correlation analysis yielded strong correlations between sodium mass concentration and particle number concentration in the coarse mode (larger $1\,\mathrm{\mu m}$), unsurprisingly indicating a significant contribution of SSA to that mode. CCN number concentration was highly correlated with the number concentrations of Aitken (10 to $100\,\mathrm{nm}$) and accumulation mode particles (100 to $1000\,\mathrm{nm}$). This, together with a lack of correlation between sodium mass and Aitken and accumulation mode number concentrations, underlines the important contribution of non-SSA, probably secondarily formed particles, to the CCN population.

# Contents

# Chapter 1

# Introduction

An aerosol is a suspension of liquid or solid particulate matter in a gaseous medium (Hinds, 1999). Atmospheric aerosol particles have a number of properties of relevance for processes in the atmosphere, e.g. directly interacting with solar radiation (Haywood and Boucher, 2000). As aerosol particles have both natural and anthropogenic sources, they are a factor in understanding the human impact on the Earth's radiation budget and in consequence the changing climate (IPCC, 2021). While emission levels and their influence on the radiative budget of certain climate forcers, such as carbon dioxide, are well understood, knowledge on aerosol particles and their influences is still lacking. These findings are based on simulations of the year 2019 relative to 1750 presented in IPCC (2021). An excerpt of these results regarding radiative forcing is given in Fig. 1.1. One way of reducing the uncertainty concerning the human influence on atmospheric aerosol particles, pointed out by Carslaw et al. (2013), is better constraining conditions before human impact. In the pre-industrial time, aerosol particles were mainly of natural origin. Natural sources of aerosol particles are diverse (Andreae and Raemdonck, 1983; Pruppacher and Klett, 1997) and number concentrations vary over space and time (Asmi et al., 2013). Natural aerosol particles are generated from a variety of processes and can be categorised as being either of primary or secondary origin (Tomasi and Lupi, 2016). Primary aerosol particles are emitted directly as particles, such as volcanic dust, mineral dust, sea spray aerosol (SSA), biogenic material and ash from nature-induced forest fires and biomass burning. SSA is a mix of sea salt particles and ocean-derived organic species (de Leeuw et al., 2011). Secondary aerosol particles are the result of gas-to-particle conversion processes, such as sulphate ($SO_4^{2-}$) from sulphur dioxide ($SO_2$) and sulphur compounds (e.g. dimethyl sulphide, DMS; Minikin et al., 1998), natural nitrates from tropospheric nitrogen oxides ($NO_x$; Seinfeld and Pandis, 2006), and organic aerosols from biological volatile organic compounds (BVOC; O'Dowd et al., 2002; Riipinen et al., 2012; Gordon et al., 2017). Non-sea salt (nss) sulphate, i.e. the fraction of total sulphate not associated with sea salt, was found to originate from both natural (Covert et al., 1992; Raes, 1995) and anthropogenic sources (Savoie and Prospero, 1989). Emissions of marine microbial activity products, e.g. DMS, and subsequent oxidation is a natural source of nss-sulphate (Curran et al., 2003; Abram et al., 2010). Further, DMS oxidation products, e.g. methanesulfonic acid (MSA) or sulphuric acid, can condense onto pre-existing, smaller particles, resulting in these particles growing into the size range relevant for cloud activation (Kulmala et al., 2000; Chen et al., 2015).

From the multitude of properties that aerosol particles have, I focus in this thesis on their impact on the Earth's atmosphere, in particular via clouds. Aerosol particles influence cloud albedo (Twomey, 1974) and cloud life-time (Albrecht, 1989). Aerosol particles are capable of initiating droplet formation at levels of supersaturation ($SS$) lower than the supersaturation necessary for homogeneous droplet formation (Köhler, 1936). At which $SS$ particles activate is mainly dictated by their size, but also by their chemical composition (Dusek et al., 2006). If a particle is a suitable nucleus for condensation at atmospheric supersaturation conditions, it is called a cloud condensation nucleus (CCN). Quinn et al. (2017) found a large portion of the aerosol population with sizes
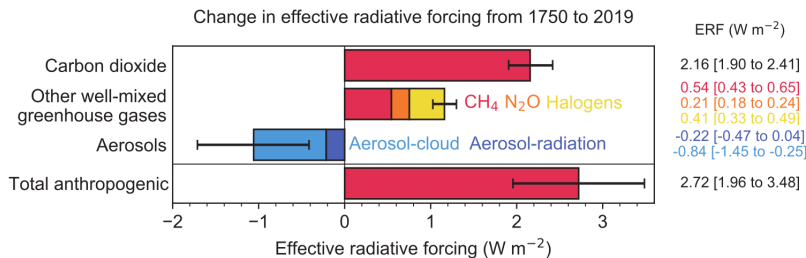
**Figure 1.1:** Estimated radiative forcing by anthropogenic emissions and drivers for 2019 relative to 1750. Adapted from Forster et al. (2021).
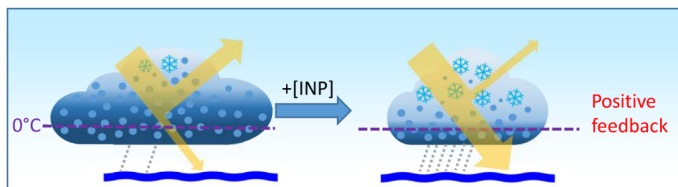


**Figure 1.2:** Illustration of the response of a mixed-phase cloud to an increasing INP number concentration and the resulting change in interaction with incoming solar radiation (yellow). Adapted from Murray et al. (2021).

between $10\,\text{nm}$ and $100\,\text{nm}$ to act as CCN at $SS > 0.5\,\%$. SSA was found to dominate the CCN population, but only at $SS = 0.1\,\%$ ($N_{\text{CCN},0.1}$) in the high latitudes of the Southern hemisphere (Quinn et al., 2017). Further, SSA contribution to the CCN population was found to increase with increasing wind speed (Gong et al., 2020b). Another group of cloud property-altering aerosol particles are ice-nucleating particles (INP). Capable of initiating droplet freezing at temperatures above $-39\,^{\circ}\text{C}$ (Pruppacher and Klett, 1997), INP alter the phase-state (frozen vs liquid) of clouds, which causes changes in cloud radiative properties (Cantrell and Heymsfield, 2005; DeMott et al., 2010; Hoose and Möhler, 2012; Vergara-Temprado et al., 2018). Furthermore, the phase-state influences the precipitation behaviour (Prenni et al., 2007; Sanchez-Marroquin et al., 2020) and life-time of clouds (Albrecht, 1989). Down the line, changes in cloud radiative properties and cloud life-time may have impacts on the Earth's climate (Lindzen, 1990; Murray et al., 2012). The effect of INP on mixed-phase clouds in a changing climate is illustrated in Fig. 1.2. Here, an increase in INP number results in an increase in ice-water and decrease in liquid water content, consequently leading to an increased transmission of incoming solar radiation. Generally, predicting the ice-nucleating properties of aerosol particles is ambitious and according to Murray et al. (2012) should be determined using quantitative experimentation. In conclusion, knowledge on the abundance of CCN and INP is a key parameter for the understanding Earth's changing climate.

Measurements of aerosol particles under pristine conditions are the key to better constraining conditions before human impact, as suggested in Carslaw et al. (2013). A starting point for the search of still-existing pristine conditions was an investigation of the global distribution of aerosol particles by Hamilton et al. (2014). With an atmospheric general-circulation model, they searched for regions of pre-industrial conditions by comparing simulations of atmospheric conditions in 1750 and 2000. The Southern Ocean (SO) region was found to feature pristine marine conditions during the Southern hemisphere's summer months, making it an excellent region for measurements of pristine aerosol conditions. This was one of the key motivations for the Study of Preindustrial-like Aerosol Climate Effects (ACE-SPACE; Schmale et al., 2019) project within the framework of the Antarctic Circum-navigation Expedition (ACE). During ACE, a research vessel (RV) went on all sectors of the SO in the Austral summer 2016/17 as shown in Fig. 1.3.

Prior to ACE, aerosol particles over the SO have been studied at a number of measurement
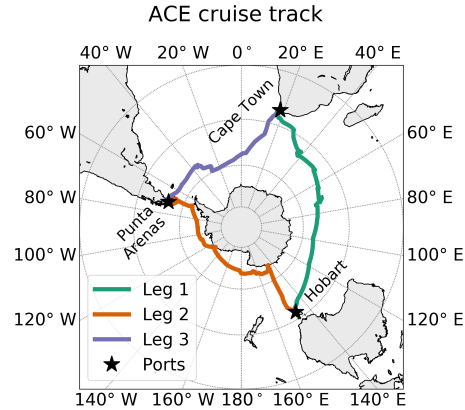
ACE cruise track



**Figure 1.3:** Hourly position of the research vessel (RV) *Akademik Tryoshnikov* during ACE. The ports visited as part of the cruise are indicated (stars). Leg 1 (green) from Cape Town (South Africa) to Hobart (Australia) between 20 December 2016 and 19 January 2017, Leg 2 (orange) from Hobart to Punta Arenas (Chile) between 22 January and 22 February 2017, and Leg 3 (purple) from Punta Arenas to Cape Town between 26 February and 19 March 2017.

stations and during several ship-based expeditions. An overview on these measurement campaigns is presented in Schmale et al. (2019) and I give a brief summary in the following. At Cape Grim Baseline Station (CGBS; 40.68°S, 144.68°E), long-term monitoring of atmospheric constituents is performed since 1976, including CCN since 2012 (Gras and Keywood, 2017). Based in Antarctica's Halley station (75.57°S, 25.51°W), in situ measurements of cloud and aerosol properties over coastal Antarctica and the Weddell Sea were performed in the Austral summer of 2015, during the Microphysics of Antarctic Clouds (MAC) field campaign (O'Shea et al., 2017). For the Macquarie Island Cloud and Radiation Experiment (MICRE), radiation and aerosol instrumentation was operated on Macquarie island (54°S, 159°E) from March 2017 to March 2018 (DeMott et al., 2018). One of the earliest ship-based expeditions with sufficient aerosol instrumentation was the British Southern Ocean (BSO) cruise between October 1992 and January 1993 (O'Dowd et al., 1997). Two research cruises within the Radiatively Important Trace Species (RITS) framework went on the SO, one in March 1993 (RITS 93) and one in December 1994 (RITS 94) (Bates and Quinn, 1997). The first Southern Ocean Cloud EXperiment (SOCEX-1) was conducted in July 1993 and the follow-up (SOCEX-2) in January–February 1995 (Boers et al., 1996, 1998). The 1st Aerosol Characterisation Experiment (ACE-1) went on the Australian sector of the SO in November–December 1995 to investigate atmospheric chemical processes and cloud micro-physics (Bates et al., 1998a). The Plankton-derived Emissions of trace Gases and Aerosols in the Southern Ocean (PEGASO) cruise went on the SO in January–February 2015, focusing on air-sea interactions of trace gases and aerosols (Dall'Osto et al., 2017; Fossum et al., 2018). The first Clouds, Aerosols, Precipitation, Radiation and atmospherIc Composition Over the southeRn oceaN cruise (CAPRICORN-1) was conducted in March 2015, with the second cruise (CAPRICORN-2) in March–April 2016 (Protat et al., 2017; Mace and Protat, 2018). During the Measurements of Aerosols, Radiation, and CloUds over the Southern oceans (MARCUS) cruise in October 2017 to April 2018, CCN were measured over the Indian Ocean and Australian sector of the SO (Humphries et al., 2021). In summary, all previously mentioned expeditions went on confined parts of the SO. An expedition spanning all sectors of the SO has not been attempted prior to ACE and marks the first time a circum-Antarctic data set on aerosol particles has been collected.

Of the earlier presented aerosol-related studies over the SO, the majority focused on aerosol particle properties in general, as well as their composition. During ACE-1, Quinn et al. (1998) found the marine boundary layer (MBL) aerosol population with dry particle diameters ($D_p$) between 50 and 300 nm (referred to as "accumulation mode") to be minimally influenced by primary aerosol (e.g.

SSA) and mainly comprised of nss-sulphate, a secondary aerosol. Dynamic mixing and subsequent dilution with ultra-fine mode particles from the free troposphere (FT) was observed in the MBL over the SO during ACE-1 (Bates et al., 1998b). The mixed-in ultra-fine particles dominated the particle numbers in the Aitken and accumulation mode size ranges. Further, these ultra-fine mode particles were attributed to new particle formation (NPF) events (Clarke et al., 1998; Humphries et al., 2016). Properties of Aitken mode ($D_\mathrm{p} = 10$–$100\,\mathrm{nm}$, same definition throughout this thesis) and accumulation mode particles (generally $D_\mathrm{p} = 0.1$–$1\,\mathrm{\mu m}$) in the SO region were found to be clearly dependent on air-mass origin, with two distinct air-masses (polar and maritime) being encountered during the BSO campaign (O'Dowd et al., 1997), as well as the PEGASO cruise (Dall'Osto et al., 2017; Fossum et al., 2018). Both air-masses featured distinctly different aerosol properties in terms of abundance and chemical composition. Looking at the composition of the larger particle size ranges, for ACE-1 the particles population of the coarse mode ($D_\mathrm{p} = 0.3$–$5\,\mathrm{\mu m}$; $D_\mathrm{p} > 1\,\mathrm{\mu m}$ throughout this thesis) was found to be dominated by sea salt, with sporadic and minor contributions from nss-sulphate. Variations in the coarse mode's (generally $D_\mathrm{p} > 1\,\mathrm{\mu m}$) sea salt concentrations could only partially (roughly $40\,\%$) be explained by local wind speeds (Quinn et al., 1998). The concentrations of particles in the SO's MBL that act as CCN were investigated by a smaller number of studies. Cases of polar air during PEGASO featured $N_{\mathrm{CCN},0.8}$ of $217\pm31\,\mathrm{cm}^{-3}$ (mean$\pm$one standard deviation), while maritime cases showed almost doubled concentrations ($420\pm168\,\mathrm{cm}^{-3}$). More recently, Fossum et al. (2020) found sea salt nuclei indirectly controlling sulphate nuclei activation in updraft conditions, in a way that sulphate aerosol activation was suppressed at greater sea salt nuclei concentrations, hinting on a delicate interplay between two types of CCN found in marine conditions. It remains an open question how CCN abundance is distributed over the SO and what typical values are, especially during the pristine conditions of the Austral summer. Further, CCN properties and origin are of interest. It is know that NPF in the FT is an important source of MBL CCN and occurs frequently over the summertime SO (McCoy et al., 2021).

To date, it is not known which process/source (e.g. NPF or SSA) generally governs the CCN population of the SO and what role atmospheric transport processes play. Consequently, I formulated the following scientific questions and provide answers throughout this thesis:

- What are typical CCN number concentrations in the Southern Ocean region?

- What is the CCN's hygroscopicity and how does it vary between the Southern Ocean's sectors?

- What are the sources of the Southern Ocean region's CCN?

Studies on INP abundance and origin in the SO region started with immersion freezing experiments by Bigg (1973). Measured INP number concentrations ($N_{\mathrm{INP}}$) at $-15\,^\circ\mathrm{C}$ were between 3 and $250\,\mathrm{m}^{-3}$. For CAPRICORN-1, McCluskey et al. (2018a) found INP number concentrations by a factor of up to 100 lower than what Bigg (1973) observed, with values varying between 0.04 and $1000\,\mathrm{m}^{-3}$ in the temperature range between $-12$ and $-31\,^\circ\mathrm{C}$. Further, McCluskey et al. (2018a) investigated the contribution of biological INP using heat treatment methods by assuming biological INP to be heat-labile. INP on the SO were found to be mainly heat-resistant, with contributions from heat-labile INP in the temperature range between $-15$ and $-20\,^\circ\mathrm{C}$. In Bigg (1973) it was hypothesised, based on the fact that INP number concentrations did not increase significantly in the vicinity of Australia, that there was no influence of dust from the Australian continent. Correlation of INP and ambient radon concentrations was used to assess whether sampled INP have terrestrial or marine sources for both CAPRICORN-1 & 2. The INP source potential of bubble bursting was characterised for CAPRICORN-1 in McCluskey et al. (2018a), using seawater samples. Overall, INP were found to be from marine sources for CAPRICORN-1. Additionally, Uetake et al. (2020) show that bacteria sampled during CAPRICORN-2 are mostly of marine origin, suggesting a restricted meridional transport of continental aerosol towards the SO. In consequence, a dominance of sea spray on the INP population was concluded. However, data on INP abundance, spatial distribution, properties, and sources over the SO region remain sparse. Consequently, I investigate the following questions in this thesis:

- What are the INP number concentrations in the Southern Ocean region and how do they vary between the Southern Ocean's sectors?

- What are the sources of the Southern Ocean region's INP?

In Regayre et al. (2020), it is pointed out that already a small number of aerosol measurements from the SO can effectively reduce model uncertainty more than hundreds of measurements in the Northern hemisphere, as current models are based on very few observations in that region. This demonstrates a need for further experimental investigations of CCN and INP in the SO region.

In this thesis, the results of the CCN and INP measurements during ACE are presented and discussed. Chapter 2 is dedicated to the theoretical background of cloud-altering aerosol particles, i.e. CCN and INP. Chapter 3 is about the ACE cruise in general, its instrumentation for aerosol particle characterisation, and the methods applied on the data gathered by it. In chapter 4 the results of the analyses performed on the data gathered during ACE are presented. Chapter 5 contains the summary of all the presented findings and will give answers to the scientific questions formulated above.

Please note that hereafter, text passages and figures are taken from the following (peer-reviewed and accepted) publication which was published in the framework of my PhD thesis:

Tatzelt, C., Henning, S., Welti, A., Baccarini, A., Hartmann, M., Gysel-Beer, M., van Pinxteren, M., Modini, R. L., Schmale, J., and Stratmann, F.: Circum-Antarctic abundance and properties of CCN and INP, *Atmos. Chem. Phys. Discuss.* [preprint], doi:10.5194/acp-2021-700, in review (accepted 14 June 2022), 2021.

# Chapter 2

# Fundamentals

The following chapter focuses on the theoretical background of aerosol particles that influence cloud droplet formation and glaciation. Firstly, the role of CCN on droplet formation is mathematically described. Secondly, ice nucleation is discussed.

## 2.1 Aerosol particle activation

The interaction of a particle with the surrounding water vapour is described by the Köhler theory (Köhler, 1936). The resulting formation of droplets depends on the chemical composition and size of the particle itself and the water vapour content of it's surrounding air. A simplification of Köhler theory, including a representation of the particle's chemical composition by a single parameter, is presented in Petters and Kreidenweis (2007) and referred to as $\kappa$-Köhler theory in the following.

### 2.1.1 Köhler theory

The water vapour content of air can be quantified by the saturation ratio ($S$), which is the ratio of water vapour pressure, $e$, and saturation vapour pressure, $e_{\text{sat}}$ ($S = e/e_{\text{sat}}$). More commonly, the water vapour content of the atmosphere is described by the relative humidity ($RH = S \cdot 100\,\%$). In the atmosphere $e$ can exceed $e_{\text{sat}}$, which results in a $RH$ value above $100\,\%$. These conditions are called super-saturated and the level of supersaturation ($SS$) can be expressed as:

$$SS = (S - 1) \cdot 100\,\% = RH - 100\,\%. \tag{2.1}$$

The equilibrium water vapour pressure over the curved surface of a droplet is described by Köhler theory (Köhler, 1936). For a single compound in a solution the relation between $S$ and the droplet diameter, $D$, is given by:

$$S = \exp\left(-\frac{B}{(D^3 - D_{\text{u}}^3)} + \frac{A}{D}\right), \text{ where } A = \frac{4 \cdot M_{\text{w}} \cdot \sigma_{\text{w}}}{R \cdot T \cdot \rho_{\text{w}}} \text{ and } B = \frac{6 \cdot n_{\text{sol}} \cdot M_{\text{w}}}{\pi \cdot \rho_{\text{w}}}. \tag{2.2}$$

This is called the Köhler equation and it includes the dry diameter ($D_{\text{u}}$), the molecular mass of water ($M_{\text{w}}$), the surface tension of water ($\sigma_{\text{w}}$), the universal gas constant ($R$), the temperature ($T$), the density of water ($\rho_{\text{w}}$), and the number of moles of solute ($n_{\text{sol}}$). The Köhler equation (Eq. 2.2) summarises two effects, which correspond to its two terms. In order to illustrate these effects, the Köhler curves for ammonium sulphate particles of different sizes are given in Fig. 2.1 (solid lines). The first term in Eq. 2.2 describes the Kelvin effect, where $e$ is larger over a curved surface compared to a flat surface. The Kelvin effect results in $e$ increasing with decreasing $D$ and is illustrated in Fig. 2.1 by the curve for pure water (dashed line). The reduction of $e_{\text{sat}}$ by water-soluble substances is described by the Raoult effect, represented by the second term in Eq. 2.2. In Fig. 2.1 the Raoult
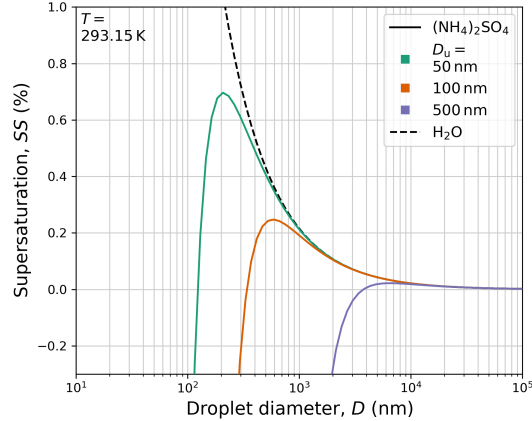
**Figure 2.1:** Results of the Köhler equation (Eq. 2.2) for ammonium sulphate particles ((NH$_4$)$_2$SO$_4$; solid lines) at a temperature, $T$, of 293.15 K. The effect of the Raoult term (first term in Eq. 2.2) is demonstrated by dry diameters ($D_u$) of 50 nm (green), 100 nm (orange), and 500 nm (purple). The curve for pure water (H$_2$O; dashed line) is given to illustrate the effect of the Kelvin term (second term in Eq. 2.2). Adapted from Andreae and Rosenfeld (2008).

effect is illustrated by Köhler curves for ammonium sulphate particles with different sizes (solid lines, colour-coded) showing overall lower $SS$ values for larger $D_u$. The maximum of the Köhler curve is the critical supersaturation, $SS_{crit}$, and its corresponding droplet diameter is the critical activation diameter ($D_{act}$). Before reaching a size equal to $D_{act}$, the solution droplet is in equilibrium with its surroundings. By exceeding $D_{act}$, the solution droplet is activated, experiencing theoretically infinitesimal growth due to the steady decrease in needed $SS$. However, under atmospheric conditions the amount of available water vapour is finite. This prevents infinitesimal growth of cloud droplets and results in a maximum reachable droplet diameter.

### 2.1.2   $\kappa$-Köhler theory

For the $\kappa$-Köhler theory (Petters and Kreidenweis, 2007) the Raoult term in the Köhler equation is parameterised by a single parameter, the hygroscopicity parameter $\kappa$. It is defined as:

$$\kappa = \frac{4 \cdot A^3}{27 \cdot D_{crit}^3 \cdot \ln^2 SS},$$

(2.3)

which includes the diameter where a particle is barely large enough to be activated at a given $SS$, the critical dry diameter ($D_{crit}$). In general, $\kappa$ quantifies the affinity of a material for water. For atmospheric particles, the range of $\kappa$ values spans roughly from 0 (insoluble particles, e.g. soot) to 1.4 (very hygroscopic, e.g. sodium chloride), as shown in Petters and Kreidenweis (2007). Under the assumption of an internally mixed particle population, $\kappa$ can be calculated by deriving $D_{crit}$. For that, the measured CCN number concentrations ($N_{CCN}$) and particle number size distribution (PNSD) are used in a way that the PNSD is integrated until the resulting particle number concentration, $N$, is equal to $N_{CCN}$. The particle diameter at this point is $D_{crit}$.
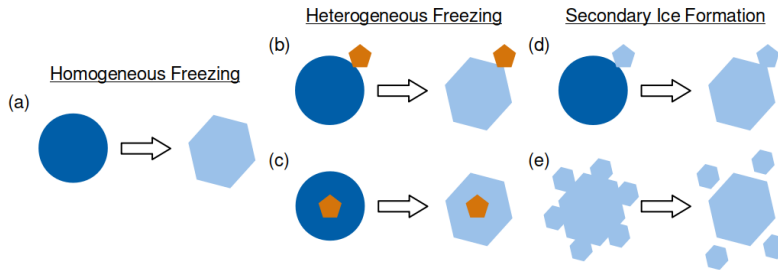
**Figure 2.2:** Overview on possible freezing mechanisms of a super-cooled cloud droplet (dark blue) that result in the formation of an ice crystal (light blue). Freezing of pure water droplets, homogeneous freezing, is illustrated in (a). With the help of an aerosol particle acting as INP (brown), ice crystals can form via (b) INP-initiated contact freezing or (c) immersion freezing. In addition, two kinds secondary ice formation, ice-initiated contact freezing and collisional fracture, are illustrated in (d) and (e), respectively. Adapted from Kanji et al. (2017).

## 2.2 Ice nucleation

The formation of a new stable phase at the expense of an original meta-stable phase of a thermodynamic system is called nucleation. Ice nucleation is the formation of ice particles from the vapour or liquid phase. In the atmosphere, ice nucleation is the result of one of the following three processes. Firstly, the freezing of pure water or solution droplets, called homogeneous freezing (Fig. 2.2a). Secondly, a catalyst (i.e. an INP) can initiate droplet freezing (heterogeneous freezing; Fig. 2.2b,c). Finally, secondary ice formation can occur by existing ice crystals initiating the freezing of water vapour or droplets (Fig. 2.2d), or crystals breaking apart and the resulting crystals acting as INP (Fig. 2.2e).

### 2.2.1 Homogeneous Freezing

The molecules in a single droplet of super-cooled water can form clusters. The number and size of these clusters is temperature-depended, in a way that both quantities are larger at lower temperatures. Once one cluster exceeds a critical size, ice nucleation occurs spontaneously. Under atmospheric conditions, homogeneous freezing occurs at temperatures below about $-38\,°\mathrm{C}$ (Rosenfeld and Woodley, 2000).

Homogeneous freezing can be described in theory by the change of a system's free energy resulting from the formation of a single cluster, the so-called Gibbs free energy of homogeneous nucleation ($\Delta G_{\mathrm{hom}}$). It is temperature-dependent and defined as:

$$\Delta G_{\mathrm{hom}}(T) = \Delta G_{\mathrm{S}}(T) + \Delta G_{\mathrm{V}}(T) = 4 \cdot \pi \cdot \sigma_{\mathrm{i/l}} \cdot r^2 - \frac{4 \cdot \pi \cdot r^3}{3 \cdot v(T)} \cdot k_{\mathrm{B}} \cdot T \cdot \ln(S), \qquad (2.4)$$

with the inter-facial energy between liquid and solid phase ($\sigma_{\mathrm{i/l}}$), the liquid volume occupied by one molecule ($v$), and the Boltzmann constant ($k_{\mathrm{B}}$). An example for the Gibbs free energy as a function of the cluster radius, $r$, at a fixed $T$ is given in Fig. 2.3. The curve for $\Delta G_{\mathrm{hom}}$ in Fig. 2.3 (purple line) results from the superposition of two effects that are the terms of Eq. 2.4. The first term, $\Delta G_{\mathrm{S}}$, describes the energy that is needed to form a curved interface or cluster surface. This is called the surface term since it depends on the surface area of the cluster ($4 \cdot \pi \cdot r^2$). In Fig. 2.3 $\Delta G_{\mathrm{S}}$ is shown
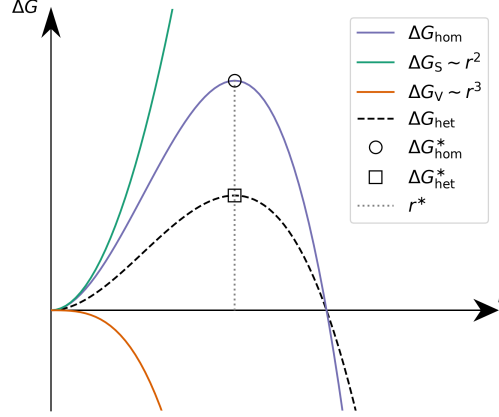
**Figure 2.3:** Gibbs free energy as a function of cluster radius ($r$) for homogeneous ($\Delta G_{\text{hom}}$; purple) and heterogeneous ($\Delta G_{\text{het}}$; dashed line) nucleation. Surface term ($\Delta G_{\text{S}}$; green) and volume term ($\Delta G_{\text{V}}$; orange) of $\Delta G_{\text{hom}}$ (Eq. 2.4) are given in the figure for reference. The maxima of $\Delta G_{\text{hom}}$ ($\Delta G_{\text{hom}}^*$; circle) and $\Delta G_{\text{het}}$ ($\Delta G_{\text{het}}^*$; square), and the corresponding critical cluster radius ($r^*$; dotted line) are indicated. Adapted from Grawe (2019).

as a green line. In contrast, the second term of Eq. 2.4, $\Delta G_{\text{V}}$, depends on the volume of the cluster ($\frac{4}{3} \cdot \pi \cdot r^3$) and is therefore called the volume term (orange line in Fig. 2.3). It describes the energy that is released due to the phase transition. The maximum of $\Delta G_{\text{hom}}$ (circle in Fig. 2.3) marks the transition from unstable to stable clusters and its corresponding radius, $r^*$, is the critical cluster radius. The location of $r^*$ is described by the Kelvin equation:

$$r^* = \frac{2 \cdot \sigma_{\text{i/l}} \cdot v(T)}{k_{\text{B}} \cdot T \cdot \ln(S(T))}. \tag{2.5}$$

At $r^*$, Eq. 2.4 can be expressed as:

$$\Delta G_{\text{hom}}(r^*(T)) = \Delta G_{\text{hom}}^*(T) = \frac{16 \cdot \pi}{3} \frac{v(T)^2 \cdot \sigma_{\text{i/l}}^3}{(k_{\text{B}} \cdot T \cdot \ln(S))^2}. \tag{2.6}$$

This equation underlines that $\Delta G_{\text{hom}}^*$ and $r^*$ are smaller at lower temperatures, at which the chance of homogeneous nucleation to happen spontaneously is increased.

The number of molecules joining a critical cluster per time interval and droplet volume is expressed by the homogeneous nucleation rate coefficient, $j_{\text{hom}}$, defined as:

$$j_{\text{hom}}(T) = w(T) \cdot n^*(T) = \frac{k_{\text{B}} \cdot T}{h} \cdot \exp\left(-\frac{\Delta F(T)}{k_{\text{B}} \cdot T}\right) \cdot n_{\text{l}} \cdot \exp\left(-\frac{\Delta G_{\text{hom}}^*(T)}{k_{\text{B}} \cdot T}\right), \tag{2.7}$$

with the diffusive flux of water molecules across the liquid-solid interface ($w$), the number of critical clusters ($n^*$), the Planck constant ($h$), the activation energy for diffusion of molecules across the liquid-solid interface ($\Delta F$), and the number density of molecules in the liquid phase ($n_{\text{l}}$). The bonds that hold the molecules together in the liquid phase need to be broken in order for a phase change from liquid to solid to occur. Reorientation of the water molecules to the ice lattice and creation of the bonds with the solid phase is necessary and requires energy. In this case, the required energy is described by $\Delta F$. In Eq. 2.7, a number of parameters are included which cannot be directly measured, including $j_{\text{hom}}$. Therefore, parameterisation is needed (e.g. Zobrist et al., 2007). Another option is the derivation of $j_{\text{hom}}$ via measurements of the frozen fraction $f_{\text{ice}}$, the ratio of frozen droplets and the total number of droplets after a time $t$ at a constant $T$. Since nucleation is a stochastic process, the freezing of all droplets of a population at a single temperature is highly

unlikely. However, the freezing of a droplet with a volume $V_d$ can be triggered by a single nucleation event (Pruppacher and Klett, 1997). The increasing likeliness of a critical cluster in a larger droplet compared to a smaller droplet underlines the importance of $V_d$. For a population with a number of equally sized droplets ($n_d$), that contains a number of frozen ($n_{fr}$) and unfrozen droplets ($n_{ufr}$), the change in the number of unfrozen droplets, $dn_{ufr}$, can be written as:

$$dn_{ufr} = -n_{ufr} \cdot V_d \cdot j_{hom}(T) \cdot dt. \tag{2.8}$$

Integrating Eq. 2.8 from $n_d(t=0)$ to $n_{ufr}(t)$ under the assumption of a constant $T$ leads to the frozen fraction, $f_{ice}$, given as:

$$f_{ice} = \frac{n_{fr}}{n} = 1 - \exp(-V_d \cdot j_{hom}(T) \cdot t). \tag{2.9}$$

### 2.2.2 Heterogeneous Freezing

If a solid surface is introduced to a super-cooled liquid droplet, the critical Gibbs free energy is lowered in comparison to the energy needed for homogeneous nucleation. Here, less water molecules need to join a cluster to reach a critical state, due to the presence of the solid surface. The introduction of the surface itself can occur in a number of ways. If freezing is triggered by an INP getting in contact with a super-cooled droplet, it is called contact freezing (Fig. 2.2b). If the INP is included in the super-cooled droplet, the process is called immersion freezing (Fig. 2.2c).

Under the assumption that clusters on the surface of the INP form spherical caps with irregular gaps (Fletcher, 1959), the critical Gibbs free energy of heterogeneous nucleation ($\Delta G^*_{het}$) can be described as a decrease in $\Delta G^*_{hom}$ (see Eq. 2.6) by a reduction factor $f$:

$$\Delta G^*_{het}(T) = \Delta G^*_{hom}(T) \cdot f. \tag{2.10}$$

The magnitude of $f$ depends on the angle between the surface of the INP and the spherical cap of the cluster, the so-called contact angle ($\theta$). It is given as:

$$f(\theta) = \frac{1}{2} \cdot (2 + \cos(\theta)) \cdot (1 - \cos(\theta))^2. \tag{2.11}$$

Inter-facial energies between the INP's surface, the solid phase's surface (ice phase), and the liquid phase's surface have an influence on $f$. The static equilibrium at the interface of the three phases is described by Young's equation (Young, 1805):

$$\cos(\theta) = \frac{\sigma_{n/l} - \sigma_{n/i}}{\sigma_{i/l}}, \tag{2.12}$$

with the inter-facial energy between nucleus and liquid phase ($\sigma_{n/l}$), nucleus and solid phase ($\sigma_{n/i}$), and liquid and solid phase ($\sigma_{i/l}$). Here, the contact angle is the characteristic value that describes the INP. For a contact angle of 0°, $f(\theta) = 0$ and that leads to the nucleation of the super-cooled droplet. For $\theta = 180°$, $f(\theta) = 1$ and homogeneous nucleation will take place. Consequently, efficient INP are characterised by a small $\theta$. Substituting $\Delta G^*_{hom}$ and $n_l$ in Eq. 2.7 with $\Delta G^*_{het}$ and the number density of water molecules at the interface of critical cluster and super-cooled liquid water ($n_{i/l}$), respectively, leads to the heterogeneous nucleation rate coefficient, $j_{het}$, given by:

$$j_{het}(T) = \frac{k_B \cdot T}{h} \cdot \exp\left(-\frac{\Delta F(T)}{k_B \cdot T}\right) \cdot n_{i/l} \cdot \exp\left(-\frac{\Delta G^*_{het}(T)}{k_B \cdot T}\right). \tag{2.13}$$

Derivation of $j_{het}$ is only achievable under a number of assumptions, by measuring $f_{ice}$. Heterogeneous ice nucleation can be described by two approaches, a stochastic approach and a singular approach.

In the stochastic approach, a change in the number of unfrozen droplets is given by:

$$dn_{ufr} = -n_{ufr} \cdot A_n \cdot j_{het}(T) \cdot dt, \tag{2.14}$$

including the surface area of the INP ($A_{\mathrm{n}}$). Integrating Eq. 2.14 from $N(t = 0)$ to $n_{\mathrm{ufr}}(t)$ for a constant $T$ leads to:

$$f_{\mathrm{ice}} = 1 - \exp(-A_{\mathrm{n}} \cdot j_{\mathrm{het}}(T) \cdot t). \tag{2.15}$$

At a constant $T$, $f_{\mathrm{ice}}$ is increasing over time and this has been shown in experiments under laboratory conditions (e.g. Murray et al., 2011).

The preferred formation of clusters at certain points of the surface of an INP, called surface sites, is assumed in the singular approach on heterogeneous ice nucleation. Each surface site has a characteristic temperature, $T_{\mathrm{c}}$, at which freezing is triggered. The droplet itself freezes at a $T$ equal to the highest $T_{\mathrm{c}}$ of all surface sites. A population of droplets that is cooled to $T_{\mathrm{c}}$ experiences that a number of droplets is freezing, the ones that contain surface sites active at this temperature. However, without a change in temperature the number of frozen droplets remains the same since no nucleation takes place. Consequently, nucleation is independent of time. The number of surface sites which initiate freezing between $T_0 = 0\,^{\circ}\mathrm{C}$ and the minimum temperature ($T_{\mathrm{min}}$), per surface area, is given in Connolly et al. (2009) by:

$$n_{\mathrm{s}} = - \int_{T_0}^{T_{\mathrm{min}}} k(T)\, \mathrm{d}T, \tag{2.16}$$

with the number of surface sites per surface area and temperature interval or so-called ice-active site density ($n_{\mathrm{s}}$), number of active sites per surface area ($k$), and the temperature interval ($\mathrm{d}T$). Here, the chnage in the number of unfrozen droplets, $\mathrm{d}n_{\mathrm{ufr}}$, is given by:

$$\mathrm{d}n_{\mathrm{ufr}} = -n_{\mathrm{ufr}} \cdot A_{\mathrm{n}} \cdot k(T) \cdot \mathrm{d}T. \tag{2.17}$$

Integrating Eq. 2.17 from $N(T_0)$ to $n_{\mathrm{ufr}}(T_{\mathrm{min}})$ and inserting Eq. 2.16 leads to a description of $f_{\mathrm{ice}}$, in the form of:

$$f_{\mathrm{ice}} = 1 - \exp(-A_{\mathrm{n}} \cdot n_{\mathrm{s}}(T_{\mathrm{min}})). \tag{2.18}$$

## Summary

In summary, the formation of cloud droplets as a result of an aerosol particle, i.e. an CCN, interacting with the surrounding water vapour is described by Köhler theory and depends on the size and the chemical position of the particle. By parameterising the chemical composition of the particle, the $\kappa$-Köhler theory gives an idea on the composition of the CCN population. The glaciation of super-cooled cloud droplets can occur without (homogeneous freezing) and with the help of aerosol particles, called INP. In the presence of INP, freezing can occur at higher temperatures.

# Chapter 3

# Campaign, instrumentation, and data handling

The following chapter contains a description of the ACE cruise and the instrumentation used in the context of this thesis, as well as the subsequent data analysis. Firstly, I give an overview on ACE itself. Secondly, I introduce the in situ instrumentation that was used to characterise the sampled aerosol particles in terms of size and ability to act as CCN. Thirdly, the offline filter sampling and the analyses of the filters with regards to ionic composition and ice-activity of the sampled material is described. Lastly, I present the additional resources that I used in addition to my analyses in order to give context to the CCN and INP results.

## 3.1 Antarctic Circum-navigation Expedition

ACE was organised by the Swiss Polar Institute and took place on-board the RV *Akademik Tryosh-nikov* (Fig. 3.1a). The cruise map in Fig. 1.3 shows that the cruise was divided into three Legs: Cape Town (South Africa) to Hobart (Australia), Hobart to Punta Arenas (Chile), and Punta Arenas to Cape Town. The cruise included stays at the ports of Hobart (18–22 January 2017) and Punta Arenas (22–26 February 2017). These port visits mark pauses to the actual cruise and are characterised by increasing closeness to inhabited land-masses and associated anthropogenic aerosol sources. The RV passed by or was on station in the vicinity of several islands in and close to the SO region. During Leg 1, the RV was close to Marion, Kerguelen, and Heard island. During Leg 2, the RV was in the vicinity of Scott, Peter 1$^{\text{st}}$, and Diego Ramírez island. Leg 3 saw the RV close to South Georgia, South Sandwich, and Bouvetøya island. Since terrestrial sources of aerosol particles are connected to open surfaces, information on the snow-cover of each island is important for further investigations of the aerosol particle origin. Besides additional information on ACE and its logistics, the cruise report in Walton and Thomas (2018) features photographs of each island at the visit of the cruise. These photographs indicate that six islands were snow-covered during the respective time of the visit. The remainder of islands (Marion, Kerguelen, and Diego Ramírez) was without visible snow-cover and terrestrial sources of aerosol particles are more likely in these cases. In addition to snow-covered islands, ACE went to Antarctica's Mertz Glacier (29–31 January 2017) and passed the Siple ice shelf during Leg 2 (11–12 February 2017). At Mertz Glacier, the southern-most latitude of 78°S was reached.

During ACE, a number of scientific measurements were carried out from a number of disciplines, e.g. biology, climatology, and oceanography. A comprehensive description of the scientific goals and instrumentation set-up during ACE is given in Walton and Thomas (2018). This thesis focuses on the in situ aerosol particle measurements and sampling on filters for subsequent INP-related and chemical analysis carried out during ACE, as part of the ACE-SPACE project. An overview on ACE-SPACE is given in Schmale et al. (2019).
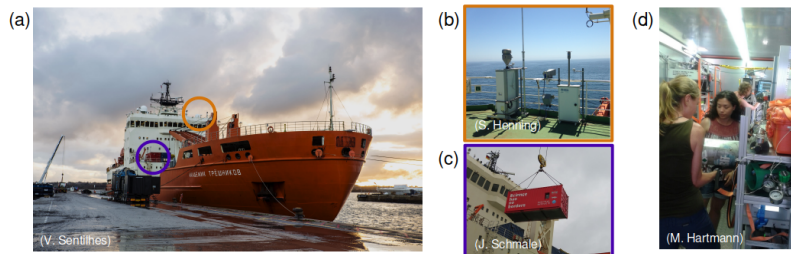
**Figure 3.1:** A photograph of the *Akademik Tryoshnikov* docked as part of ACE in (a), with the location of the two filter samplers (orange circle) and the laboratory container (purple circle) indicated. The two filter samplers installed on the RV's upper deck are shown in (b). The laboratory container, prior to its installation on the fore-deck of the RV, is shown in (c). A view inside the laboratory container, where the in situ instrumentation was installed, is shown in (d).
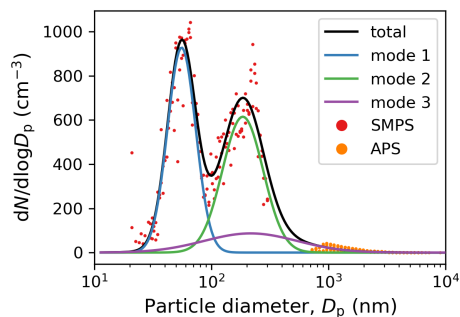


**Figure 3.2:** An example for the results of the mode-fitting approach applied to the output of the Spinning Mobility Particle Analyser (SMPS) and Aerodynamic Particle Sizer (APS) instruments. PNSD from the SMPS (red) and APS instruments (orange) are given as dots. The three fitted log-normal distributions (Aitken mode, blue; accumulation mode, green; sea spray mode, purple) and the sum of the three modes (total PNSD, black) are given as lines.

## 3.2   In situ aerosol measurements

The instrumentation for all in situ aerosol measurements presented in this thesis was situated in a temperature-controlled laboratory container (Fig. 3.1c) on the fore-deck of the RV (purple circle in Fig. 3.1a). The container was equipped with two standard aerosol inlets (Global Atmosphere Watch, Weingartner et al., 1999) at roughly 15 m above sea level (a. s. l.). The inlets allowed only for particles with dry particle diameter smaller than 40 µm ($PM_{40}$) to be sampled. The sampled air was dried to $RH < 40\%$, to prevent uncontrolled hygroscopic growth. An iso-kinetic splitter was used, together with as short as possible tubing, to feed the aerosol to the different instruments inside of the laboratory container.

### 3.2.1   Aerosol number size distribution

PNSD of aerosol particles in the mobility diameter range of 11 nm to 400 nm and aerodynamic range of 500 nm to 19 µm were measured during ACE using a Spinning Mobility Particle Analyser (SMPS, custom-built by PSI) and an Aerodynamic Particle Sizer (APS; model 3321, TSI inc., Shoreview, MN, USA), respectively.

The SMPS instrument consists of an impactor, a neutraliser, a Differential Mobility Analyser

(DMA), and a Condensation Particle Counter (CPC; model 3022, TSI inc.) in series (Wiedensohler et al., 2012). With the impactor, aerosol particles larger than a set diameter are removed. The neutraliser is a bipolar diffusion charger that aims to bring the sampled particles in an approximate bipolar charge equilibrium. The DMA consists of a charged electrode that is surrounded by a cylinder and the particles are inserted together with a laminar sheath flow of particle-free air. Charged particles that are not of a certain size are removed by applying a voltage between the electrode in the centre and the outer cylinder. This leads to particle of a certain size exiting the instrument. Modulation of the applied voltage enables a scanning of different particle sizes. Particles exiting the column are counted by a Condensation Particle Counter (CPC), in which particles are exposed to levels of supersaturation and the subsequent condensation enables optical detection.

The APS instrument consists of a acceleration nozzle and a laser anemometer (Wilson and Liu, 1980). The sampled particles form the sample flow, that is surrounded by a particle-free sheath flow. The inner nozzle focuses the aerosol flow, while the outer nozzle accelerates the entire flow. Due to inertia, larger particles are not accelerated as fast as smaller particles. Behind the nozzle, the time of flight of individual particles is measured with a laser beam. A direct proportion between time of flight and aerodynamic diameter exists.

Validation of sizing accuracy of both instruments was performed using polystyrene latex spheres. To minimise influence of the ship's exhaust, data filtering was performed for the SMPS' and APS' output, based on sudden changes in the total particle number concentration ($N_{\text{total}}$), carbon dioxide, black carbon, and wind direction, as described in Moallemi et al. (2021).

PNSD of SMPS and APS were merged, as illustrated in Fig. 3.2. As a first step, the SMPS output (red dots in Fig. 3.2) was converted from mobility to geometric diameter by assuming a spherical particle shape together with a charge distribution. Secondly, the APS' output (orange dots in Fig. 3.2) is converted from aerodynamic to geometric diameter under the assumption of spherical shape and a material density of $1.8\,\text{g}\,\text{m}^{-3}$. Both outputs combined enable interpolation of the gap in detectable particle size between the SMPS ($D_{\text{p}} \leq 400\,\text{nm}$) and APS ($D_{\text{p}} > 500\,\text{nm}$) instruments. Further, a mode fitting technique analogue to Modini et al. (2015) was applied, that is based on a method described in Khlystov et al. (2004) and fully described in the supplement to Landwehr et al. (2021). Under the assumption that each individual PNSD results from superposition of up to three aerosol modes, log-normal distributions in pre-defined size ranges are fitted. The three modes are Aitken (modal diameter in the range of $1\,\text{nm}$–$20\,\text{nm}$; referred to as "mode 1" in the following; blue line in Fig. 3.2), accumulation ($10\,\text{nm}$–$100\,\text{nm}$; "mode 2"; green line in Fig. 3.2), and a sea spray mode (centred within $140\,\text{nm}$–$220\,\text{nm}$; "mode 3"; purple line in Fig. 3.2). For each time step, combining all fitted modes results in a smoothed total PNSD (black line in Fig. 3.2) that is used where a measured PNSD is too noisy at low concentrations, e.g. for the subsequent calculation of the CCN hygroscopicity.

## 3.2.2 Cloud condensation nuclei

A CCN Counter (CCNC; *CCN-100* instrument, DMT, Boulder, CO, USA; see Fig. 3.3a) was used to measure CCN number concentrations at various $SS$ during ACE. The CCNC's main component is a continuous-flow thermal gradient diffusion chamber, which is sketched in Fig. 3.3b. In the chamber, a stream-wise temperature gradient (red line in Fig. 3.3b) is induced to achieve defined $SS$ and corresponding particle activation to droplets (Roberts and Nenes, 2005). The aerosol flow rate inside the CCNC is $0.5\,\text{L}\,\text{min}^{-1}$. Activated particles are counted by an optical particle counter behind the chamber. Calibration of the CCNC was performed prior to the cruise, following the standard operating procedure given in Gysel and Stratmann (2014) and recommendations in Schmale et al. (2017). During the cruise, the CCNC was operated at $SS$ of $0.1\,\%$, $0.15\,\%$, $0.2\,\%$, $0.3\,\%$, $0.5\,\%$ and $1\,\%$, maintained for $10\,\text{min}$ each. To ensure stable thermal conditions within the instrument, data collected during the first $5\,\text{min}$ of each $SS$ set-point were discarded. Furthermore it was ensured that (1) the instrument's internal thermal stability control reported thermally stable conditions, and (2) the absolute difference between set and read temperature of the optics was smaller than $2\,\text{K}$. The remaining data were aggregated into $1\,\text{min}$ intervals and filtered for ship exhaust influences (same
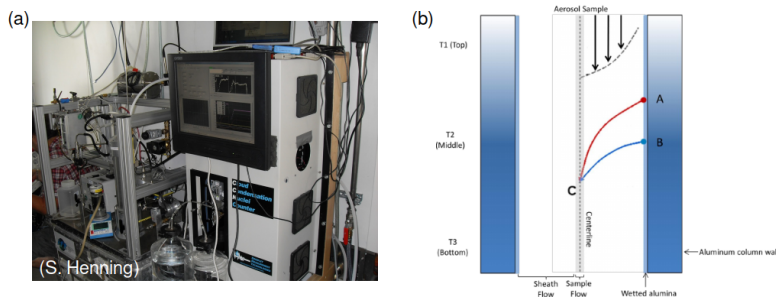
**Figure 3.3:** Phtotgraph of a CCN Counter (CCNC) in the laboratory in (a). A schematic of the CCNC's measurement column is presented in (b). Due to the differences in heat (red line) and water vapour diffusion (blue line), an $SS$ can be set at the centre line ($C$). Adapted from Roberts and Nenes (2005).

as SMPS and APS, see subsection 3.2.1). Based on the filtered values, averaged $N_{CCN}$ at particular $SS$ were calculated. This procedure results in one $N_{CCN}$ value per hour and level of supersaturation. No correction to standard conditions (1013.25 hPa and 273.15 K) was performed. During data analysis, CCN number concentrations at 0.1 % were found to lack sufficient data quality, therefore measurements at this supersaturation were discarded and not shown in the following chapter.

**Determination of critical dry diameter**

For determining critical dry diameters a procedure used in, e.g. Herenz et al. (2019) and Gong et al. (2020b) was applied. Here, it is assumed that all particles represented by the size distribution that are larger than a particular diameter are activated at given $SS$, implying the assumption of an internally mixed particle population. In consequence, the concentration of activated particles is equal to the measured $N_{CCN}$ value. For each $N_{CCN}$ value, the simultaneously measured size distribution is searched. The beginning of the one hour period for which the PNSD represents the aerosol particle population has to be within 1 h before or after the CCN measurement. If no adequate size distribution is available, no $D_{crit}$ value is derived. The cumulative sum of the PNSD is calculated from largest to smallest dry particle diameter value. The cumulative sum represents an integral of the PNSD, with the upper bound being 10 μm, equal to the cut-off diameter of the inlet that the instruments needed for the PNSD were operated on (see subsection 3.2.1). The dry particle diameter value corresponding to the point where the PNSD's cumulative sum exceeds the measured CCN number concentration is a first indication for the position of critical dry diameter. The exact critical dry diameter value is obtained by linear interpolation between the smallest dry particle diameter where the cumulative sum is smaller than CCN number concentration and the largest dry particle diameter where the cumulative sum is larger than $N_{CCN}$.

To model error propagation in the calculation of critical dry diameter and quantities derived from it Monte Carlo simulation (MCS) was used, following what was done for Herenz et al. (2019). The uncertainty in particle number concentration (and thus PNSD) is assumed to be 5 %, corresponding to one standard deviation (Gysel and Stratmann, 2014). A realistic particle concentration is calculated using:

$$x_{MC} = x \cdot (1 + u \cdot p). \tag{3.1}$$

Here, for a measured signal $x$, the MCS signal $x_{MC}$ is calculated with a relative uncertainty of $u$ and a set of random numbers $p$. In our case, $p$ consists of 10000 normal-distributed random numbers

(mean value: 0; one standard deviation: 1).

**Determination of CCN hygroscopicity**

The hygroscopicity parameter $\kappa$, an indirect measure for chemical composition of the CCN at a given dry particle diameter, is derived from the adjusted $SS$, the corresponding critical dry diameter, and the temperature inside the CCNC's measurement column ($T_{\mathrm{col}}$) using Eq. 2.3 (see subsection 2.1.2). Corresponding to $N_{\mathrm{CCN}}$, one $\kappa$ value per hour and supersaturation is determined.

In a similar way to the critical dry diameter, the error in adjusted $SS$ in Eq. 2.3 is assessed by using MCS, with a relative uncertainty of 3.5 % for $SS \geq 0.2$ % and an absolute error for $SS < 0.2$ %, according to Gysel and Stratmann (2014).

In addition, the range between 10th and 90th percentile for the critical dry diameter was derived for each $SS$ separately and values outside this range and their associated $\kappa$ were excluded from further analysis. Hence, the results I present are representative for the most frequent occurring behaviour in $\kappa$.

## 3.3 Off-line aerosol characterisation

The two operated filter samplers (Fig. 3.1b) were positioned at the upper deck of the RV (orange circle in Fig. 3.1a) and each one run on a $PM_{10}$ inlet. After being sampled, filters were stored in a freezer (at $-20\,^\circ$C) on-board and shipped to Leibniz-Institute for Tropospheric Research (TROPOS) for off-line analysis after the cruise concluded.

### 3.3.1 High-volume sampling

Filter sampling of ambient air, for off-line INP and chemical analysis, was carried out using a high-volume sampler (HV; *DHA-80*, DIGITEL, Volketswil, Switzerland). An ultrasonic anemometer ran next to the HV sampler, providing wind direction data for an automatic shut-down mechanism of the sampler. The HV sampler uses a flow rate of roughly $500\,\mathrm{L\,min^{-1}}$, sampling air through quartz-fibre filters (*MK 360*, Munktell, Bärenstein, Germany) of 150 mm in diameter for up to 24 h per filter. Here, each filter's individual sampling time ($<1$ min to 1437 min) was dependent on the sampler's automatic shut-down mechanism.

In total, 94 HV filters were collected throughout the cruise, including four un-sampled reference filters for the HV sampling, called field blank filters (FBF). FBF were handled in the same way as sampled ones, enabling assessment of background issues due to both methodology and handling. HV filters were split between INP-related analysis, chemical composition analysis, and reserve sample. Only HV filters sampled with a volume greater than $100\,\mathrm{m^3}$ (of possible $720\,\mathrm{m^3}$) were considered, to minimise the impact of potential contaminants. In consequence, a total of 79 sampled HV filters were included in the INP-related and chemical composition analysis.

### 3.3.2 Low-volume sampling

Filter sampling of ambient air, for off-line INP analysis at the TROPOS laboratories, was carried out using a low-volume sampler (LV; *DPA-14*, DIGITEL). For 8 h per filter, LV sampling was performed at a flow rate of roughly $25\,\mathrm{L\,min^{-1}}$ on poly-carbonate membrane filters (*Whatman Nuclepore*, Cytiva, Little Chalfont, UK; see Fig. 3.4c) with 200 nm pore size and a diameter of 47 mm.

In addition, over extended periods LV filters were sampled for 2 h each, to improve resolving of diurnal variations in the INP abundance, compared to the 8 h sampling. Two of these extended periods were performed during Leg 1 and two during Leg 3. During each period, 12 LV filters were sampled over a time frame of 24 h. The first period started on 31 December 2016 at 16:00 UTC and ended on 1 January 2017 at 16:00 UTC, when the RV was on station close to Île de la Possession (SO's Indian Ocean sector). The second period was during the RV's passage to Hobart (Australia),
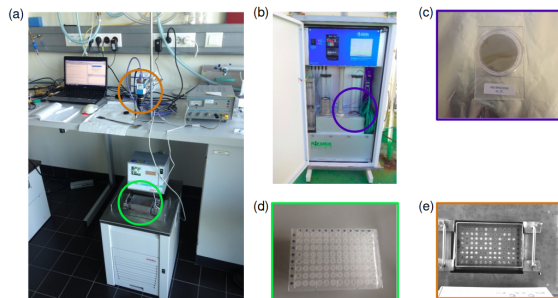
**Figure 3.4:** (a) Photograph of the ice nucleation droplet array (INDA) setup in the laboratory at TROPOS, with the camera (orange circle) and cryostat (green circle) indicated. A view inside the LV sampler is shown in (b). An example of (c) a sampled LV filter, (d) a polymerase chain reaction (PCR) tray, and (e) a picture taken by INDA's camera system is given.

between 8:00 UTC on 16 January 2017 and 8:00 UTC on 17 January 2017. The third period started on 28 February 2017 at 23:50 UTC and ended on 1 March 2017 at 23:50 UTC, when the RV was on passage from Punta Arenas (South America) towards South Georgia island (SO's Atlantic Ocean sector). The fourth period coincided with the RV being in the vicinity of Bouvetøy island between 23:50 UTC on 12 March 2017 and 23:50 UTC on 13 March 2017. With the flow rate of the LV sampler of $25\,\mathrm{L\,min^{-1}}$, the sampled volume of air was $3\,\mathrm{m^3}$ for the 2 h LV samples.

In total, 258 LV filters were handled throughout the cruise, including 48 filters sampled for 2 h and five FBF. LV filters were spent solely on the INP analysis.

### 3.3.3 Ice nucleation droplet array (INDA)

The freezing behaviour of the aerosol particles collected on each LV and HV filter was investigated using INDA at TROPOS. It is based on the freezing array method described in Conen et al. (2012), in which the sampled air is washed and diluted into droplets to determine the ice-activity. The INDA setup is shown in Fig. 3.4a and consists of a cryostat (*FP 40*, Julabo, Seelbach, Germany), a metal structure acting as a frame (green circle), a plate of light-emitting diodes (LEDs) lights, a digital camera (orange circle), and a measurement computer for data recording. The cryostat's bath is filled with ethanol. The opening of the bath is covered by a metal plate that features an opening in which a custom-made metal frame fits (Fig. 3.4e). Said frame is made in a way, that it can safely hold a PCR tray (BRAND, Wertheim, Germany; see Fig. 3.4d) horizontally at several centimetres below the opening of the bath, approximately at the top level of the ethanol. In the bath, a plastic plate with integrated LEDs is submerged, meant to illuminate the secured PCR tray from below. Roughly 20 cm centred above the opening of the cryostat's bath, a digital camera is mounted (orange circle in Fig. 3.4a). The camera is connected to the measurement computer via an Ethernet cable. In addition, the cryostat is connected to the measurement computer via a serial data cable. On the measurement computer, a *Python* script is run, catching the cryostat's internal thermometer read send via the data cable and logging them into an data table in the comma-separated values (CSV) format. Simultaneously, the digital camera is ordered to take an image of the PCR tray (example in Fig. 3.4) and it is saved as well. The measurement principle behind INDA is that frozen droplets exhibit a different behaviour of letting the light from the LED array through the PCR tray to the camera, compared to unfrozen droplets.

As the first step of the analysis process, stored filters were acclimatised to roughly $-3\,^{\circ}\mathrm{C}$ in a fridge. Due to the difference in filter material, INP analysis for LV and HV filters was slightly different. The contents of a LV filter (Fig. 3.4c) were washed off by submerging the filter in $7.5\,\mathrm{mL}$ ($V_{\mathrm{water}}$; $10\,\mathrm{mL}$ at later stages) of ultra-pure water (milliQ, $18.2\,\mathrm{M\Omega\,cm^{-2}}$). The 96 compartments of a PCR tray were filled with $50\,\mathrm{\mu L}$ each ($V_{\mathrm{d}}$) of the washing water (Fig. 3.4d). In contrast, only a

cut-out (2 cm in diameter) per HV filter was used for the INP analysis with subsequent punching out of 96 pieces of 1 mm in diameter ($D_{\text{punchout}}$). The 96 compartments of a PCR tray were filled with 50 µL of milliQ water and one punch-out. For both filter types, the resulting solution-filled PCR tray was sealed and subsequently partially submerged in the ethanol bath of INDA's cryostat. Cooled at a rate of $1\,\text{K}\,\text{min}^{-1}$, the number of frozen droplets ($n_{\text{fr}}$) and corresponding temperature profile was documented automatically every three seconds by INDA's camera system. Recommendations on sample handling and processing given in Polen et al. (2018) were followed. The frozen fraction ($f_{\text{ice}}$) was calculated by dividing number of frozen droplets by the total number of droplet per PCR plate ($n_{\text{total}} = 96$).

**Determination of atmospheric INP number concentrations**

Using INDA, a frozen fraction profile for each filter was obtained (see subsection 2.2.2). From that, the cumulative INP number concentration, $N_{\text{INP}}$, is calculated at any $T$ using:

$$N_{\text{INP}}(T) = -\frac{\ln(1 - f_{\text{ice}}(T))}{V_{\text{ref}}}, \tag{3.2}$$

with the reference volume ($V_{\text{ref}}$), following Vali (1971). For the LV filters $V_{\text{ref}}$ was calculated as:

$$V_{\text{ref,LV}} = \frac{V_{\text{flow}}}{V_{\text{water}}} \cdot V_{\text{drop}}, \tag{3.3}$$

where $V_{\text{flow}}$ is the volume of sampled air, $V_{\text{water}}$ is the volume of washing water and $V_{\text{d}}$ is the volume of water in each PCR well. In contrast, for the HV filters $V_{\text{ref}}$ was calculated using:

$$V_{\text{ref,HV}} = \frac{(\frac{1}{2} \cdot D_{\text{punchout}})^2}{(\frac{1}{2} \cdot D_{\text{filter,HV}})^2} \cdot V_{\text{flow}}, \tag{3.4}$$

where $D_{\text{punchout}}$ is the diameter of the filter sub-sample per PCR well and $D_{\text{filter,HV}}$ is the diameter of the HV filters. $V_{\text{flow}}$ was logged by both (LV and HV) samplers.

Uncertainties arising from the methodology were accessed similarly to previous studies (e.g. Wex et al., 2019; Gong et al., 2020a). Confidence intervals for $f_{\text{ice}}(T)$ of each filter were determined using a method described in Agresti and Coull (1998). Resulting lower and upper values of each $f_{\text{ice}}(T)$ in Eq. 3.2 are reported as error bars of $N_{\text{INP}}(T)$ values throughout this thesis.

To provide data points from each filter at a given temperature, estimated INP number concentrations are given for cases when frozen fractions of $f_{\text{ice}} = 0$ or $f_{\text{ice}} = 1$ were obtained, i.e. none or all wells of the PCR plate were frozen. For these two cases, Eq. 3.2 is not applicable to calculate valid concentration values. We then assume that none ($f_{\text{ice}} = 0/96$) or one ($f_{\text{ice}} = 1/96$) of the PCR wells are frozen as equally probable. A similar assumption is made when all ($f_{\text{ice}} = 96/96$) or all but one ($f_{\text{ice}} = 95/96$) PCR wells are frozen. Considering $f_{\text{ice}} = 1/96$ and $f_{\text{ice}} = 95/96$ in Eq. 3.2 yields estimates for the lower and upper limit of detectable INP number concentration, respectively.

Based on the $f_{\text{ice}}$ profiles of the FBF, averaged temperature-dependent INP number concentration for the FBF ($N_{\text{INP,FBF}}$) were determined, which were used as background INP number concentration for the sampled filters. Eq. 3.2 with an average volume of sampled air (mean $\pm$ SD) for all sampled LV (HV) filters of $8.95 \pm 0.74\,\text{m}^3$ ($471.3 \pm 151.4\,\text{m}^3$) was used to calculate $N_{\text{INP,FBF}}$.

No correction for contamination by the RV's stack exhaust was applied, as it was shown in Welti et al. (2020) that ship exhaust is not ice-active in the temperature range presented ($T > -30\,°\text{C}$).

**Normalisation of INP number concentrations**

The INP number concentrations derived for the LV filters were normalised to the aerosol surface area or alternatively volume, following Mitts et al. (2021), in order to obtain normalised ice (nucleation) activity. For this, the particle surface area and volume size distributions were first inferred from the PNSD, assuming spherical particles, and then integrated over the entire diameter range. This was

done for each size distribution measurement. These values were averaged over the 8 h sampling time of each LV filter and $N_{\mathrm{INP}}$ is divided by these values, resulting in the ice-active site density $(n_{\mathrm{s}})$ and ice-active volume density $(n_{\mathrm{v}})$, respectively.

### 3.3.4   Analysis of chemical composition

The chemical composition of the material sampled on the HV filters was analysed at the atmospheric chemistry department of TROPOS using a procedure similar to the one used in Müller et al. (2010) and van Pinxteren et al. (2017). A full description of each step of the analysis is given in the appendix (see Appendix A). Each filter was weighted, to determine the sampled $PM_{10}$ mass. A thermal-optical method was used to derive the contents of elemental carbon (EC) and organic content (OC), as described in section A.1. The water-soluble organic carbon (WSOC) was derived as well (see section A.2). The contents of a number of cations (sodium, ammonium, potassium, magnesium, and calcium) and anions (chloride, nitrate, sulphate, bromide, and oxalate) were determined by the means of ionic chromatography (see section A.3). The MSA content was determined using capillary electrophoresis (see section A.4). Results of all previous introduced procedures are given as atmospheric concentrations $(\mathrm{\mu g\,m^{-3}})$.

To access the fraction of compounds associated with sea salt (e.g. sulphate) the respective nss part was estimated using sodium as a tracer, following a method described in Piel et al. (2006). Here, non-sea salt sulphate mass concentration $(M_{\mathrm{nss\,SO_4^{2-}}})$ can be accessed using respective sulphate $(M_{\mathrm{SO_4^{2-}}})$ and sodium mass concentration $(M_{\mathrm{Na^+}})$ by means of:

$$M_{\mathrm{nss\,SO_4^{2-}}} = M_{\mathrm{SO_4^{2-}}} - \alpha_{\mathrm{SO_4^{2-}}} \cdot M_{\mathrm{Na^+}}. \tag{3.5}$$

A weighting factor for sulphate is given as $\alpha_{\mathrm{SO_4^{2-}}} = 0.252$ (Piel et al., 2006).

An influence of the RV's exhaust on the measured particle mass concentrations cannot be completely ruled out, since several HV filters visually darkened after sampling. One way of assessing this influence is the usage of EC as a tracer for the RV's emission, following van Pinxteren et al. (2017). Similarly, maximum EC and WSOC mass concentrations for cases of clean marine air sampled at North Atlantic's coastal station at Mace Head, reported in Cavalli et al. (2004), are used to estimate when clean marine air was sampled during ACE.

## 3.4   Further resources

### 3.4.1   In-water organic compound measurements

During ACE, sea water was sampled every 4 h using the RVs underway water supply system and during conductivity, temperature and depth (CTD) rosette deployments, at specific depths up to 200 m (Walton and Thomas, 2018). Glass fibre filters (22 mm in diameter, 700 nm pore size) were sampled with up to 2 l of sea water under low vacuum pressure and stored at $-80\,°\mathrm{C}$ prior to analysis on-board the RV. After extraction in 90 % acetone for 24 h, chlorophyll a (Chl a) pigment concentration $(\mathrm{mg\,m^{-3}})$ was measured utilising a fluorometer (*AU-10*, Turner Designs, San Jose, CA, USA). Calibration was performed against a standard Chl a solution (Sigma Aldrich).

Concentrations of volatile organic compounds (VOC) in sea water, like isoprene and DMS, were measured using a gas chromatography-mass spectrometry system (*5975-T LTM-GC/MSL*, Agilent Technologies, Santa Clara, CA, USA) by the Surveying Organic Reactive gases and Particles Across the Surface Southern Ocean (SORPASSO) project. A description of the full procedure can be found in Rodriguez-Ros et al. (2020).

### 3.4.2   Wind measurements

Continuous data on wind speed and direction during the cruise was obtained from two ultrasonic anemometers (part of *MAWS 420* system, Vaisala, Vantaa, Finland) located on either side of the
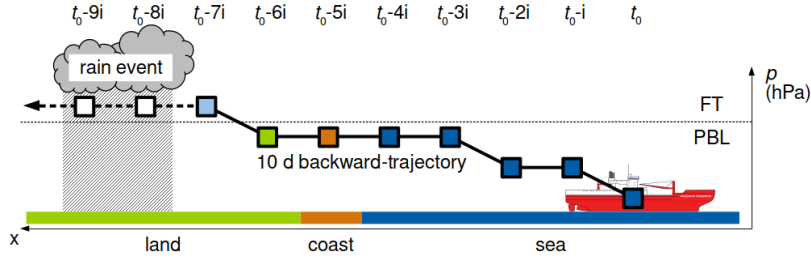
**Figure 3.5:** Simplified example of the air-mass origin analysis for the 10-day backward-trajectories. The trajectory contains information on the air parcel for the time steps $t$. Time steps within the planetary boundary layer (PBL) are classified by the underlying surface type into sea (dark blue), coast (orange), or land (light green). Time steps when the air parcel was outside the PBL are classified as free tropospheric (light blue). Time steps prior to or during a rain event are not considered for the classification (empty box).

ship on the observation deck (roughly 30 m a. s. l.) above the bridge of the RV (Walton and Thomas, 2018). Observed wind speeds were corrected for ship motion and heading using additional data from the RV's inclinometer (Landwehr et al., 2020). To estimate the wind speed at 10 m a. s. l. ($U_{10}$), measurement height and atmospheric stability were considered using a logarithmic wind speed profile, including drag co-efficient and atmospheric stability. Quantification of air-flow distortion bias generated by the RV's structures was performed using the European Centre for Medium Range Weather Forecasts (ECMWF) atmospheric model as a free stream reference. Resulting correction is applied to the observed wind speed, leading to a data set of $U_{10}$ for the cruise with a temporal resolution of 5 min.

### 3.4.3 Air-mass origin analysis

Backward-trajectories for ACE are available in Thurnherr et al. (2020). They used the LAGRANgian analysis TOol (LAGRANTO) described in Sprenger and Wernli (2015) with reanalysis data from ECMWF. These reanalyses are produced by the ECMWF Integrated Forcasting System (IFS), an atmospheric model and data assimilation system. These trajectories are used to analyse the air-mass origin in terms of geographical and surface information.

At an hourly resolution, trajectories are available for 56 pressure levels (between the surface and 500 hPa a. s. l.) above the RV's position. To achieve more robust statistics, for each hour all trajectories ending within the PBL above the RV's position are averaged into a cluster by calculating median values of latitude, longitude, pressure level, boundary layer pressure level, total precipitation, land fraction and sea ice fraction. An illustration of the following step-by-step description of the analysis is given in Fig. 3.5. The initial step is the application of a rain filter on each cluster. Here, it is assumed that aerosol particles are removed from the atmosphere by scavenging and wet deposition during precipitation events. Similar to Herenz et al. (2019), a total precipitation ($R_{total}$) threshold of 0.1 mm h$^{-1}$ between hourly time steps is used. Since the air parcel that is described by the trajectory has it's parameters calculated every three hours, the threshold in $R_{total}$ is 0.3 mm between time steps. If $R_{total}(t)$ exceeds this threshold, all time steps prior to $t$ are excluded from the analysis (white squares in Fig. 3.5). In the special case of a rain event occurring at the RV's position, the entire cluster is excluded from the analysis. As the second step of the analysis, for each cluster the pressure level of the air parcel at each time step, $p_{par}(t)$, is compared to the pressure level of the PBL ($p_{PBL}$). If $p_{par}(t)$ is smaller than $p_{PBL}(t)$ than this time step is classified as free tropospheric (light blue in Fig. 3.5) and it is assumed that the air parcel did not collect any aerosol signal from the surface. In the case of $p(t) > p_{PBL}(t)$, the surfaces type below the air parcel is categorised. Here, the IFS's land-sea mask is used for initial classification of the surface signal type. If the land-sea mask indicates that the entire surface in the grid box is land, the surface signal is classified as "land"
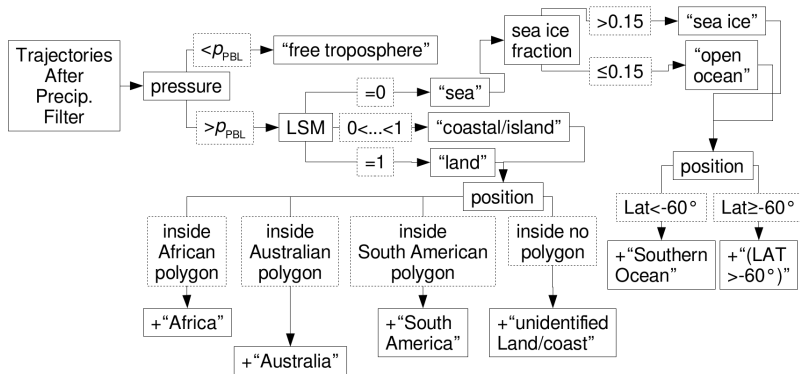
**Figure 3.6:** Classification scheme for each non-filtered time step of the backward-trajectories.

(green in Fig. 3.5). Correspondingly, if the entire grid box is over a body of water, the surface type is classified as "sea" (dark blue in Fig. 3.5). If the land-sea mask indicates neither "land" nor "sea", the surface type is classified as "coast" (orange in Fig. 3.5). If the surface below the air parcel is identified as being a body of water, the IFS's sea ice fraction is used to discriminate if it is open ocean or covered by sea ice. A commonly used sea ice fraction threshold of $<15\%$ is applied here to classify as "open ocean" (following Cavalieri et al., 1991). A sea ice fraction threshold of $>80\%$ is used to classify "sea ice". Any sea ice fraction between "sea ice" and "open ocean" is classified as "marginal ice zone" (MIZ). If the surface below the air parcel is identified as "land" or "coast", geographical polygons from air-mass source appointment tool "TRACE" (Radenz et al., 2021) are used to determine from which land-mass the surface signal stems. Three polygons from TRACE have been used, roughly outlining Africa, Australia, and South America. If the geo-location of the air parcel is outside of the three polygons, it is classified as "unidentified". The classification scheme is summarised as a decision tree in Fig. 3.6.

To upscale the results of this analysis to the coarser temporal resolution of the LV sampling (8 h per filter, see subsection 3.3.2), the PBL signals were averaged from all clusters within a LV filter's sampling period. The total number of trajectories that are averaged in clusters and considered per LV filter is between 1 and 28, with a mean of roughly 15.

### 3.4.4   Fluorescent particles

Fluorescent particles were measured during ACE using a wide-band integrated bio-aerosol sensor. A full description is given in Moallemi et al. (2021).

### 3.4.5   Correlation analysis

The collected data were used in a correlation analysis. The goal was to find possible connections between different quantities, indicated by a correlation or the lack of one. Input variables were the MSA and sodium concentrations resulting from the analysis of inorganic ions of the HV filters, INP concentrations at four temperatures ($-8\,°C$, $-12\,°C$, $-16\,°C$, $-20\,°C$ and $-24\,°C$) from the LV filters, $N_{total}$, $N_{>500}$, particle concentrations of individual PNSD modes ($N_{mode1}$, $N_{mode2}$, and $N_{mode3}$), $N_{CCN}$ at all measured $SS$ and respective hygroscopicity parameter values, $U_{10}$ and in-water Chl $a$ and DMS concentrations. Correlation analysis was performed by calculating Spearman's rank correlation coefficients and associated Spearman p-values between input variables. As data of diverse temporal resolution were used, the coarsest resolution (24 h, HV filter sampling) was chosen as framework and variables with finer resolution were averaged over 24 h periods, using median values. For each variable, 83 data points were used for the correlation analysis.

# Chapter 4

# Results and Discussion

In this chapter, I firstly present the results of the analysis regarding the entire aerosol population measured during ACE, which contains important information on the particles' origin when looking at size fractions of the population, e.g. CCN (second subsection). In the second section, the analysis of the LV filters regarding INP number concentration is presented. The third section is dedicated to the analysis of the HV filters regarding ionic composition of sampled particles, mainly focusing on sodium and MSA. The last section contains the results of the correlation analysis that was performed with quantities from all analyses mentioned above.

## 4.1  Aerosol particles and cloud condensation nuclei

### 4.1.1  Particle number size distributions

There are several ways of characterising an aerosol population. Seinfeld and Pandis (2006) show that condensation of low vapour pressure substances on already existing particles or the merging of particles (so-called "coagulation") leads to the formation of particles with sizes reaching into the Aitken (10–100 nm) and accumulation mode range (100–1000 nm). In consequence, I characterise the aerosol population encountered during the cruise by looking at the particle number concentration, $N$, and the distribution of the particle diameter, $D_\mathrm{p}$, in the following.

The arithmetic mean and respective 1 standard deviation of all hourly total smoothed PNSD measured during ACE are given in Fig. 4.1. Here, the $D_\mathrm{p}$-normalised $N$ ($\mathrm{d}N/\mathrm{dlog}D_\mathrm{p}$, y-axis) is shown as a function of $D_\mathrm{p}$ (x-axis). The mean PNSD resembles a bi-modal distribution. Bi-modality is suggestive of either entrainment of particles from the FT or in-cloud processing, according to Hoppel et al. (1986). The nucleation mode range, with $D_\mathrm{p}$ between 1 and 10 nm, is outside of what is represented by the mean PNSD. Consequently, NPF signals are not directly apparent. However, Baccarini et al. (2021) find that not more than two NPF events occurred during the entire cruise, both coinciding with the RV being in proximity to Mertz glacier. The first distinct mode in the mean PNSD has its peak at $D_\mathrm{p}$ of roughly 30 nm and lies within the Aitken mode range. The second distinct mode, with a maximum $D_\mathrm{p}$ of roughly 120 nm, is in the accumulation mode range. The minimum between the Aitken and accumulation mode is generally referred to as the Hoppel minimum, following Hoppel and Frick (1990). The Hoppel minimum of the mean PNSD in Fig. 4.1 lies visually between 70 and 80 nm, consistent with Schmale et al. (2019) finding a median value for the Hoppel minimum during ACE of around 80 nm.

The time series of the hourly total PNSD for the cruise is presented in Fig. 4.2a, showing the temporal evolution of $\mathrm{d}N/\mathrm{dlog}D_\mathrm{p}$ (colour scale) as a function of $D_\mathrm{p}$ (y-axis). The beginning and ending of each Leg is indicated by a dashed line. Gaps in the data stem from filtering for stack exhaust contamination and not all instruments for the PNSD-derivation being available at certain periods (see section 3.2). Multiple events with one of either Aitken or accumulation mode dominating
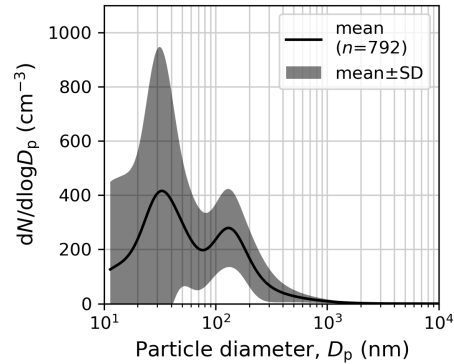
**Figure 4.1:** Mean of the total smoothed particle number size distribution for the whole cruise. The area between mean plus one standard deviation (SD) and mean minus SD is indicated (grey shaded area).

the PNSD are clearly visible in Fig. 4.2a. Events with a pronounced Aitken mode occurred regularly throughout the cruise, e.g. on 25 January, 23 February, or 9 March 2017. By conservatively assuming a particle growth rate of $1 \, \text{nm h}^{-1}$, one can estimate that an Aitken mode with a peak around 30 nm contains particles that formed up to 24 h prior to sampling. Consequently, I concluded that particles sampled throughout the cruise were likely not produced locally. Episodes of a pronounced Hoppel minimum are visible in Fig. 4.2a and underline that the encountered aerosol population experienced either entrainment of particles from the FT or in-cloud processing, as discussed in Hoppel et al. (1986).

## 4.1.2 CCN number concentrations

The CCN number concentration ($N_{\text{CCN}}$) at a $SS$ of 0.15 %, 0.2 %, 0.3 %, 0.5 % and 1 % are given in Fig. 4.2b (color-coded). $N_{\text{CCN}}$ at a particular $SS$ varied over 2 orders of magnitude throughout the cruise, e.g. at a $SS$ of 0.2 % ($N_{\text{CCN},0.2}$) from 4 to $390 \, \text{cm}^{-3}$. Under the assumption that a terrestrial influence on the aerosol population is less likely the further away the sampling location is from land, Moallemi et al. (2021) suggest a threshold for the distance to nearest land-mass, $d_{\text{land}}$, of 200 km to distinguish between the terrestrial influenced ($d_{\text{land}} \leq 200 \, \text{km}$) and the open ocean ($d_{\text{land}} > 200 \, \text{km}$) parts of the cruise. Periods when the RV was within 200 km of the nearest land are highlighted in Fig. 4.2b (grey shade) and show generally higher $N_{\text{CCN}}$ compared to the sections on the open ocean. This suggests that the aerosol particle abundance is influenced by terrestrial or anthropogenic sources and is in line with Schmale et al. (2019) showing pristine conditions during ACE being encountered only south of 55°S.

The total particle number concentration, $N_{\text{total}}$, is included in Fig. 4.2b for reference (black dots). Periodic differences between $N_{\text{total}}$ and $N_{\text{CCN},1.0}$ throughout the cruise were observed (Fig. 4.2b). Periods larger differences coincide with PNSD in Fig. 4.2a featuring a pronounced Aitken mode with elevated numbers in the size range below 40 nm. During these periods even $SS = 1 \%$ was not sufficient to activate the smaller Aitken mode particles. Consequently, quantities presented later in this thesis, that are derived from $N_{\text{CCN},1.0}$, are representative for the larger Aitken mode particles ($D_{\text{crit}}$ at this $SS$ ~30 nm, see Tab. B.1). In addition to the time series presented in Fig. 4.2b, spatial distribution of $N_{\text{CCN}}$ at all measured $SS$ are given as daily averages in Fig. B.1.

Averages of $N_{\text{CCN}}$ for the three Legs of ACE are shown in Fig. 4.3 and summarised in Tab. B.1. Due to the frequency distributions of CCN number concentration in Fig. 4.5a (introduced later) resembling log-normal distributions, averages are presented as geometric mean values and respective geometric standard deviation in Fig. 4.3 and discussed as such in the following. $N_{\text{CCN}}$ values increase with $SS$, i.e. for Leg 1 from 91 ($N_{\text{CCN},0.15}$) to $241 \, \text{cm}^{-1}$ ($N_{\text{CCN},1.0}$). For all $SS$, the largest geometric
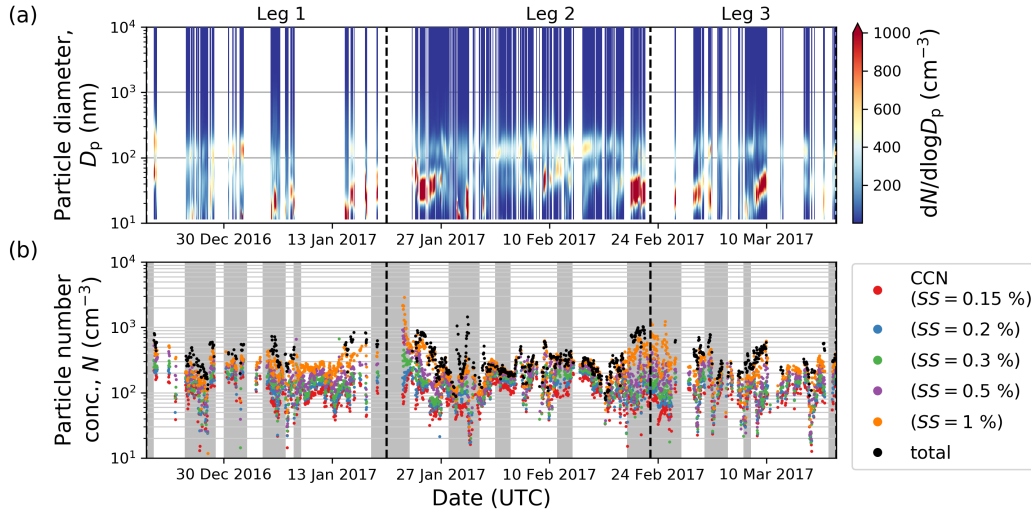
**Figure 4.2:** Time series of (a) total PNSD, and (b) total particle (black) and CCN number concentration (colour-coded by supersaturation) during Legs 1–3. Legs (dotted lines) and vicinity to land (grey area) are indicated. Data filtering for instrument availability and stack exhaust contamination has been performed.

mean values of $N_{\mathrm{CCN}}$ are observed during Leg 2. Moreover, the average Hoppel minimum diameter was found to be the largest for Leg 2, when compared to Legs 1 and 3, indicating a pronounced Aitken mode. Together with Schmale et al. (2019) showing that there is less (relative and absolute) contribution of SSA to CCN during Leg 2, this suggests a significant fraction of CCN originating from secondary aerosol production. However, differences in CCN number concentration between Legs are within the ranges given by the respective geometric standard deviations. The longitudinal differences on CCN abundance are either small against the overall variability of the data, or a variety of effects cancel each other out in a way that no clear longitudinal trend can be observed. In addition to the data for ACE, CCN number concentration from a selection of studies performed on Antarctica or over the SO are given for comparison in Fig. 4.3. For the continental Antarctic Princess Elisabeth station (PES), Herenz et al. (2019) report $N_{\mathrm{CCN},0.1}$, $N_{\mathrm{CCN},0.2}$, $N_{\mathrm{CCN}}N_{0.3}$, $N_{\mathrm{CCN},0.5}$, and $N_{\mathrm{CCN},0.7}$ values for the measurement period 2013–2016. PES is located at 71.95°S and 23.35°E on East Antarctica's Queen Maud Land and about 200 km in-land from the Antarctic coast. Overall, good agreement between mean values in Herenz et al. (2019) (2013–2016) and the geometric mean values for ACE (January–March 2017) can be found. The reported $N_{\mathrm{CCN},0.2}$, $N_{\mathrm{CCN},0.3}$, and $N_{\mathrm{CCN},0.5}$ for cases of maritime air-masses reaching PES show a difference of $-28\%$, $-9\%$ and $+1\%$ compared to the values for Legs 1–3, respectively. The largest differences occur at the lowest $SS$, 0.2 %, that is associated with the activation of larger particles. A hypothetical reason for the differences is the removal of lager particles due to atmospheric processes during transport to PES. At the Australian Cape Grim Baseline Station (CGBS; 40.68°S, 144.68°E), $N_{\mathrm{CCN},0.5}$ is measured continuously since the mid-1970s (Gras and Keywood, 2017). In Humphries et al. (2021), average $N_{\mathrm{CCN},0.5}$ for November 2017 to March 2018 at CGBS are given, coinciding with the time frame of ACE. For this period, a median of roughly 230 cm$^{-3}$ is reported (triangle pointing left in Fig. 4.3). This value is larger than the median value for Leg 1 of 181 cm$^{-3}$ (Tab. B.1) and towards the upper end of the respective range of values (IQR: 138–225 cm$^{-3}$). Difference could be due to air-masses from the Australian continent reaching CGBS. Conditions at CGBS are only representative for the SO when the wind direction is between 190° and 280°, the so-called "baseline" conditions (Gras and Keywood, 2017). At CGBS, the ambient radon concentration is used as a proxy for terrestrial influence (e.g. McCluskey et al., 2018a) and a threshold of 100 mBq m$^{-3}$ is used in Humphries et al. (2021). A median value for $N_{\mathrm{CCN},0.5}$ of 130 cm$^{-3}$ (triangle pointing right in Fig. 4.3) resulted from averaging only CGBS measurements
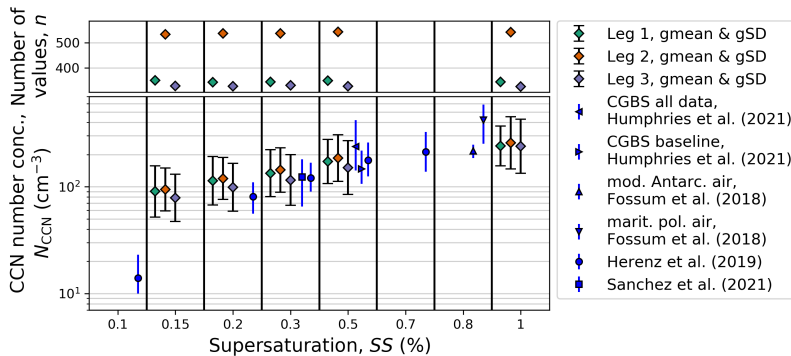
**Figure 4.3:** Geometric mean (gmean) and geometric standard deviation (gSD; whiskers) of CCN number concentration ($N_{CCN}$) for Leg 1 (green), Leg 2 (orange) and Leg 3 (purple), respectively. Included for comparison are median values and respective inter-quartile range (IQR) over all measurements at Cape Grim Baseline Station (CGBS) coinciding with PEGASO and CAPRICORN-2 from Humphries et al. (2021) (triangle pointing left) and measurements for "baseline" conditions (triangle pointing right) during that period. Baseline conditions are defined as wind directions between 190° and 280°, and ambient radon concentrations below $100\,\text{mBq}\,\text{m}^{-3}$. Averages for events of modified Antarctic air (upward pointing triangle) and maritime polar air (downward pointing triangle) from Fossum et al. (2018) are given.

during baseline conditions. This value is at the lower end of the results for Leg 1. I conclude that the terrestrial influence on the $N_{CCN,0.5}$ values for ACE is overall small and this is underlined by the results of the backward-trajectory analysis presented later in the text (subsection 4.1.4). Looking at other ship-based CCN measurements for reference values, results for the PEGASO cruise in the SO's Atlantic sector during January-February 2015 are available in Fossum et al. (2018). Since the $SS$ does not match the ones used during ACE, comparison is done semi-quantitatively in the following. Further, only Leg 3 is considered due to featuring the best geographical overlap. The result of visual interpolation between ACE's $N_{CCN,0.5}$ and $N_{CCN,1.0}$ for Leg 3 lies in the ranges $(217 \pm 31\,\text{cm}^{-3})$ reported for modified Antarctic air encountered during PEGASO (Fig. 4.3). For the BSO cruise, only CCN concentrations inferred from nss-sulphate are available in O'Dowd et al. (1997), not comparable with any CCN number concentration measured during ACE. As for aircraft-based CCN measurements, $N_{CCN,0.3}$ between 17 and $264\,\text{cm}^{-3}$, with an average of $123 \pm 58\,\text{cm}^{-3}$ (mean $\pm$ SD), are report in Sanchez et al. (2021) for flights through the MBL between 42.5°–62.1°S and 133.8°–163.1°E during the Southern Ocean Clouds, Radiation, Aerosol Transport Experimental Study (SOCRATES). The reported concentrations are slightly lower than what was measured in that area during ACE, with values between 48 and $452\,\text{cm}^{-3}$ and an average of $178 \pm 99\,\text{cm}^{-3}$ (mean $\pm$ SD). Besides the difference in measurement height (SOCRATES: 50 m a. s. l. until height of inversion; ACE: ~15 m a. s. l., see section 3.2), another factor is that measurements are from successive years, with the ACE cruise being in that area during 16 January to 26 January 2017 and the 15 flights during SOCRATES in the period of 15 January to 25 February 2018.

Complementary to the quasi-longitudinal characterisation of CCN number concentrations on the SO in Fig. 4.3, an overview on the latitudinal behaviour is given in Fig. 4.4. The number of averaged values per bin is given for completeness (blue bars). Overall, the lowest median concentrations are observed at each $SS$ between 55° and 60°S, with concentrations generally increasing towards the north and the south. Differences between median values are within their respective variability (given by the error bars) and thus no apparent dependence of CCN abundance on latitude is found. With this and the longitudinal indifference presented in Fig. 4.3, I conclude that CCN number concentration averages for the whole cruise (Legs 1–3) in Tab. B.1 are representative for any point of the cruise. Median values for the combined MARCUS and CAPRICORN-2 cruises from Humphries
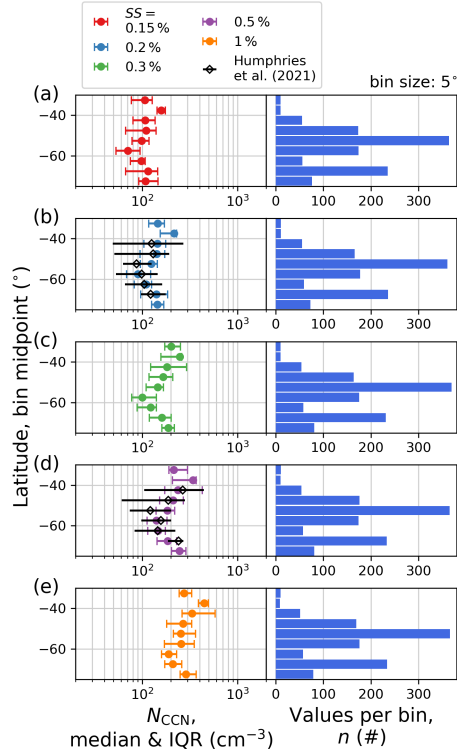
**Figure 4.4:** Median and respective IQR of CCN number concentration ($N_{CCN}$) at $SS$ of (a) 0.15 %, (b) 0.2 %, (c) 0.3 %, (d) 0.5 %, and (e) 1 % for Legs 1–3, binned by the latitude of the RV's position. The bins span the latitude from 40°S to 75°S, with a bin size of 5°. The number of values averaged for each bin is indicated in the fig (blue). For reference, median values of $N_{CCN,0.2}$ and $N_{CCN,0.5}$ for the combined MARCUS and CAPRICORN-2 cruises from Humphries et al. (2021) are given in (b) and (d).

et al. (2021) are given in Fig. 4.4a,d for reference (open diamonds). Agreement with the results for ACE is generally good, with only the minimum location being further north for MARCUS and CAPRICORN-2, between 50° and 55°S. This trend of concentrations increasing both north- and southward from the respective minimum value is shared between the results for ACE and the combined MARCUS and CAPRICORN-2 cruises.

PDF of normalised frequencies for $N_{CCN}(SS)$ are given in Fig. 4.5 and resemble mono-modal distributions for all $SS$. With increasing $SS$ the PDF's maxima shift towards higher CCN number concentrations, e.g. from roughly $90\,cm^{-3}$ at 0.15 % to roughly $210\,cm^{-3}$ at 1 %. When comparing the PDF for $N_{CCN,0.2}$ (blue line in Fig. 4.5) to yearly-averaged PDF for a number of measurement sites around the globe in Schmale et al. (2017), the overall low concentration values and the PDF maximum around $100\,cm^{-3}$ found for ACE best resembles the PDF reported for clean marine conditions (mono-modal with maximum at $\sim$200 cm$^{-3}$). Looking at $N_{CCN,0.3}$ (green line in Fig. 4.5), the mono-modal PDF's maximum is between 100 and $200\,cm^{-3}$. This is different from the $N_{CCN,0.3}$ PDF reported for the MBL-Legs of SOCRATES in Sanchez et al. (2021) that resembles a bi-modal distribution with local maxima at 100 and $150\,cm^{-3}$, respectively. Sanchez et al. (2021) attributed the lower concentration mode to precipitation events that efficiently remove larger particles. The higher concentration mode is associated with ageing of particles that results in an increase in particle size over time, e.g. due to in-cloud processing. A potential reason for the ACE data lacking two distinct modes could be the larger spatial (circum-Antarctic) and temporal coverage (3 months) compared to the SOCRATES data (15 flights over 1.5 months).
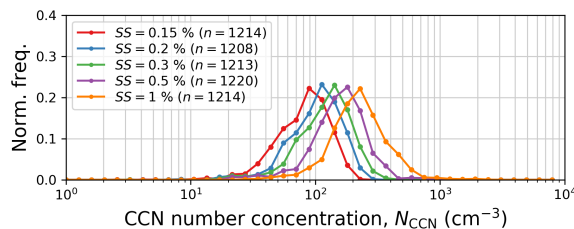
**Figure 4.5:** Normalised probability density function (PDF) of CCN number concentration ($N_{\mathrm{CCN}}$) for level of supersaturation ($SS$) 0.15 %, 0.2 %, 0.3 %, 0.5 % and 1 % (colour-coded) for Legs 1–3. $N_{\mathrm{CCN}}$ values at five minute resolution and number of samples ($n$) is indicated in the figure.

### 4.1.3   CCN hygroscopicity

An overview concerning the aerosol particle hygroscopicity parameter $\kappa$ values observed during Legs 1–3 is given in Fig. 4.6. Due to the frequency distributions in Fig. 4.7b (later introduced) not resembling log-normal distributions, median values and respective IQR are presented and discussed in the following. Error bars include both the natural variability and the measurement uncertainty in $\kappa$, as described in section 3.2.2. In Fig. 4.6a, $\kappa$ values are shown as a function of their associated critical dry diameter ($D_{\mathrm{crit}}$) values. Median values of either the full cruise (black) or parts of it (colour-coded) are shown for each $SS$. For reference, the relation between $\kappa$ and $D_{\mathrm{crit}}$ given by Eq. 2.3 is illustrated for $SS$ of 0.15 % (dotted line) and 1 % (dashed line) in the figure. In the following, the results shown in Fig. 4.6a are discussed in a way that in the first step only the $D_{\mathrm{crit}}$ values are considered, while in the second step only the $\kappa$ values are considered. In the third and final step, the relation between both quantities is further discussed. Firstly, when looking solely at $D_{\mathrm{crit}}$ (x-axis), a range between 25 and 125 nm is covered by all $SS$ when including error bars. Considering that the median Hoppel minimum location for the full cruise is at around 80 nm (Schmale et al., 2019), $D_{\mathrm{crit}}$ generally lie within either the Aitken mode range ($SS \geq 0.2$ %) or the lower accumulation mode range ($SS = 0.15$ %). Secondly, when looking solely at $\kappa$ values (y-axis), a range between 0.2 and 0.9 is covered by all $SS$ when including the variability-uncertainty range (indicated by IQR as error bars). Differences in $\kappa$ median values between Legs can be seen in Fig. 4.6a, with Leg 1 (green) showing generally the lowest values for all $SS$ while Leg 2 (orange) generally shows the highest values. Finally, when looking at the size-dependence of $\kappa$, no clear trend for $\kappa$ is apparent when error bars are considered. This is suggestive of the chemical composition of the CCN to be independent of particle size and therefore the presence of an internally well-mixed CCN population. However, when considering $\kappa$ median values alone, for $D_{\mathrm{crit}}$ up to 100 nm a slight increase in $\kappa$ with $D_{\mathrm{crit}}$ can be seen in Fig. 4.6a for Leg 2 (orange) and Legs 1–3 (black). This is in line with the general expectation of a lower $\kappa$ at smaller $D_{\mathrm{crit}}$, as organic gases condensing on pre-existing particles results in smaller values of $\kappa$, and larger, aged particles activating at lower $SS$, are associated with higher $\kappa$ (McFiggans et al., 2006). Legs 1 and 3 do not feature increasing $\kappa$ with increasing $D_{\mathrm{crit}}$, which again suggests an internally mixed CCN population. In addition, $\kappa$ as a function of $SS$ is given in Fig. 4.6b. Analogous to what is done for CCN number concentration in Fig. 4.3, values from the literature and previous studies are included for reference. For pure substances, Petters and Kreidenweis (2007) give a $\kappa_{\mathrm{mean}}$ between 0.1 and 0.2 for organic material, 0.61 for ammonium sulphate, and 1.28 for sodium chloride. In addition to that, in Schmale et al. (2019) a $\kappa$ of about 0.32 is hypothesised for MSA. All shown $\kappa$ values in Fig. 4.6b, including respective error bars, are above the range given for organic material. The majority of $\kappa$ values lies between the reference values for MSA (cyan dashed line) and ammonium sulphate (orange dashed line). This indicates that the sampled CCN population features a significant amount of organic material. However, the CCN population can also be composed of other insoluble (or moderately soluble) materials. Interestingly, $\kappa$ values for Leg 1 are closest to what is assumed for MSA compared to any other part of the cruise. Looking at

reference values, the $\kappa$ values for ACE are much lower than the ones reported in Herenz et al. (2019) for the Austral summer on continental Antarctica at PES (blue triangles in Fig. 4.6b). They found $\kappa_{0.1}$ to be in the range between 0.8 and 1.3, which is close to the value reported for pure sodium chloride in Petters and Kreidenweis (2007) (dark blue dashed line). These differences suggest that a significantly different aerosol was sampled on PES compared to what was encountered over the SO during ACE. While Herenz et al. (2019) interpreted their sampled particles to be of mostly inorganic nature and therefore assumed a marine primary origin, values for ACE hint towards an organic nature and a most likely secondary origin of the particles. Comparison to globally modelled $\kappa_{0.1}$ for the surface layer ($0.92 \pm 0.09$) and the planetary boundary layer ($0.8 \pm 0.17$) in the SO region, given in Pringle et al. (2010), suggests an overestimation of sea salt contribution and/or an underestimation of the presence of organic material in the model. A global model producing a $\kappa$ for the SO region as high as double of what was measured in situ may have strong implications on the perceived CCN properties and the modelled CCN interactions with clouds.

PDF for $D_{\mathrm{crit}}$ and $\kappa$ are given in Fig. 4.7. For $D_{\mathrm{crit}}$ mono-modal distributions are found for all $SS$ in Fig. 4.7a, with broader distributions for larger $SS$. Further, the maximum's position is decreasing with increasing $SS$, consistent with what is shown in Fig. 4.6a. For the PDF of $\kappa$ (Fig. 4.7b), a change in distribution shape with increasing $SS$ can be seen. All five shown distributions have their maximum between 0.4 and 0.6, while a mono-modal distribution is only found for $\kappa_{0.15}$ (red line). PDF for $SS$ of 0.3, 0.5, and 1 % (green, purple, and orange line, respectively) feature a tail towards smaller values of $\kappa$, which could be interpreted as an additional mode. The occurrence of small particles (activated at high $SS$) consisting mainly of organic material forms a strong case for the sampled Aitken mode CCN originating from secondary organic aerosol formation and growth processes. The accumulation mode, probed with the measurements at $SS = 0.15$ %, shows similar $\kappa$ values as the Aitken mode (Fig. 4.7b), while its CCN number concentration values are on average over 33 % smaller (Fig. 4.5a). Additionally, PDF for all $SS$ other than 0.15 % feature a tail towards higher $\kappa$ values. Such high $\kappa$ values at high $SS$ seem counter-intuitive and are indicative of highly hygroscopic Aitken mode particles being sampled. I performed a sensitivity study with respect to (1) modelling the measurement uncertainty via MCS and (2) considering error propagation in section C.1. As $\kappa$ values were robust against these variations, I conclude that this tail (yet counter-intuitive) is not an artefact that stems from the methodology. However, to avoid speculation on the reason, a conservative approach is taken in keeping the focus of the discussion on the median values presented in Fig. 4.6b.

### 4.1.4 Air-mass origin for aerosol particle and CCN measurements

I analysed the backward-trajectories for ACE to elucidate influences of free tropospheric and boundary layer air-masses on the prevailing aerosol population. In Fig. 4.8, hourly results of this analysis are presented. At each time step, all trajectories ending at the RV's position within the PBL were vertically averaged and the number of trajectories considered for this averaging is given as a point of reference in Fig. 4.8a (magenta dots). This number is highly variable throughout the cruise, ranging from 1 to 25, depending mainly on the PBL height and the surface pressure at the RV's position. The duration of individual, averaged trajectories is indicated in Fig. 4.8a (black) and strongly affected by the application of the precipitation filter (pink). It is highly variable throughout the cruise and a feature of increasing duration for successive trajectories is apparent (e.g. 24 February 2017), suggesting that trajectories are cut at the same rain event while the distance to the RV and thus the time it takes for the air-mass to reach the RV increases. Looking at the distribution between residency of the averaged trajectories in either PBL or FT (Fig. 4.8b), a strong free tropospheric influence (>50 %) coincides with trajectories showing a duration above 96 h in Fig. 4.8a. That trajectories have a higher chance of being influenced by the FT if they are not cut by the applied rain filter is a fact worth mentioning here.

The surface type contributions for times when the investigated air-masses were within the PBL are given in Fig. 4.8c and show that overall an oceanic influence dominated each Leg, especially Leg 1. However, throughout Leg 2 and in the beginning of Leg 3, shorter periods with a strong

terrestrial (land or coast) influence are found. Sporadic contributions to the air-mass from sea ice and marginal ice zone (MIZ) can be found during each Leg, with their combined fractions reaching up to 50 % (e.g. 17 February 2017). As for information on the geographical location, Fig. 4.8d shows that the oceanic influence present for the majority of Leg 1, the beginning of Leg 2, and the majority of Leg 3 stems mostly from north of 60°S. As for oceanic air-masses from within the SO region, only a few cases occurred, especially between 27 January and 20 February 2017 when the RV was close to Antarctica during Leg 2.

Contributions to the air-mass origin were averaged over the whole cruise and individual Legs, as presented in Fig. 4.9. The average distribution between total residence time in PBL or FT of all averaged trajectories (Fig. 4.9a) shows that on average the cruise was dominantly influenced by the PBL, with contributions from the FT of about 30 %. Looking at individual Legs, the average for Leg 2 shows a smaller influence of the PBL compared to the whole cruise, with a contribution of around 60 %. In comparison to Leg 2, a higher PBL influence is found for Leg 3 ($\sim$80 %). The averaged surface type contributions in Fig. 4.9b show that oceanic air-masses were the largest part of the PBL's influence during the cruise, with an average contribution of about 85 %. The remaining 15 % are dominated by air-masses of terrestrial origin (land and coast, $\sim$10 %), with sea ice or MIZ only contributing marginally (below 5 %). Comparing the whole cruise and its Legs, Leg 3 resembles the cruise average best in terms of the distribution between oceanic and terrestrial influences. For Leg 1 and Leg 2 the contribution of the oceanic influence differs from the whole cruise, with values of roughly 95 % and 75 %, respectively. For each Leg air-masses of terrestrial origin are mainly from coastal regions. Leg 2 exhibits the highest overall sea ice influence of about 5 %. Information on the geo-location of the PBL influences in Fig. 4.9c shows that the cruise is characterised by a majority of contributions ($\sim$60 %) from oceanic origin north of 60°S. In contrast, the SO contributes to roughly 30 % of the cruise average. The remaining 10 % originate almost equally from Antarctica and South America. Looking at Legs individually mirrors what is shown in Fig. 4.8: Leg 2 is dominated by oceanic origin from the SO ($\sim$60 %), with the remaining contributions equally split between non-SO oceanic and continental origin. In contrast, Leg 1 and Leg 3 are dominated by non-SO oceanic influences and the SO contributing only up to 10 %. For Leg 3, contributions from the SO and South America are roughly equal.

Median values for $N$ per binned value of free tropospheric ($f_{\text{FT}}$), terrestrial ($f_{\text{TR}}$), Antarctic ($f_{\text{AN}}$), oceanic ($f_{\text{OC}}$) and sea ice ($f_{\text{IC}}$) contribution are presented in Fig. 4.10. Here, $N_{\text{total}}$ and the particle number concentrations of the 3 modes (Aitken, accumulation, and sea spray; see subsection 3.2.1) of the total PNSD ($N_{\text{mode1}}$, $N_{\text{mode2}}$, and $N_{\text{mode3}}$) are included (colour-coded). The contribution value, $f_{\text{x}}$, is calculated by dividing the number of time steps of each trajectory cluster over the surface type, "x", by its total number of time steps. For $N$ of both mode 1 (green) and mode 2 (orange) no trend with any $f$ is apparent in Fig. 4.10, with differences in $N$ median values remaining within their respective IQR. From that I conclude that particle abundance in the Aitken and accumulation range is not driven by primary origin associated with any of the investigated surface types. In contrast, for mode 3 (purple) higher number concentrations are found with increasing oceanic (Fig. 4.10d) and consequently decreasing terrestrial (Fig. 4.10b) and Antarctic influence (Fig. 4.10c). This underlines that the exposure of air-masses to the open ocean is driving the abundance of the sea spray mode, hinting on a primary aerosol origin.

Median values and respective IQR of measured CCN number concentrations as function of FT, terrestrial, Antarctic, oceanic and sea ice contribution are presented in Fig. 4.11a–e. For better readability, only CCN number concentration at $SS$ of 0.15 % (red), 0.3 % (yellow) and 1 % (blue) are presented. In subsection 4.1.3, it is shown that measurements at $SS = 0.15$ % are representative for accumulation mode particles and at $SS = 1$ % larger Aitken mode particles acting as CCN are represented (see Fig. 4.6). $SS = 0.3$ % is included as it represents atmospheric conditions and measured in-cloud $SS$. No trend is apparent for neither free tropospheric (Fig. 4.11a) nor sea ice influence (Fig. 4.11e) and the investigated CCN number concentration, as differences between $N_{\text{CCN}}$ median values are within a factor 2. This variability is to small in comparison to the overall variability in CCN number concentration of roughly 2 orders of magnitude (see subsection 4.1.2) to identify

any meaningful signal in the air-mass origin. However, the decrease in CCN number concentration with increasing terrestrial contribution, $f_{TR}$, in Fig. 4.11b marks an interesting feature. For mostly oceanic air-masses ($f_{TR} \sim 0.1$), $N_{CCN,0.15}$ and $N_{CCN,0.3}$ decrease with increasing $f_{TR}$. In contrast, for air-masses of mostly terrestrial origin ($f_{TR} \sim 1$), $N_{CCN,0.3}$ and $N_{CCN,1.0}$ decrease while $N_{CCN,0.15}$ increases. For a mix of terrestrial and oceanic influence ($f_{TR} \sim 0.5$), a superposition of both before-mentioned effects occurs, with $N_{CCN,0.3}$ median values below $N_{CCN,1.0}$ and above $N_{CCN,0.15}$.

In summary, this simple attempt to get information on the source region does not work for the Aitken and accumulation mode particles represented by the total particle (Fig. 4.10) and CCN number concentration (Fig. 4.11). Trajectories might not be able to resolve of the associated mixing process as NPF more likely occurs above the mixing layer.

## Summary

In summary, a bi-modal aerosol population was encountered during the cruise. CCN number concentrations varied over 3 orders of magnitude per $SS$, which is in line with other studies on the SO. The lowest CCN number concentrations were encountered between 55°S and 60°S. The histogram of $N_{CCN}$ resembled what was found for clean marine conditions. No connection between $N_{CCN}$ and the duration of the air-mass in the FT, over Antarctica, or sea ice could be established. However, higher $N_{CCN}$ were found for air-masses having spent longer times over the non-Antarctic continents, hinting on a terrestrial source. The CCN hygroscopicity parameter was found to be size-independent, suggesting an internally mixed CCN population.

## 4.2  Ice nucleating particles

### 4.2.1  INP abundance

Time series of $N_{\text{INP}}(T)$ for $T = -24\,°\text{C}$ ($N_{\text{INP},-24}$; orange), $N_{\text{INP},-20}$ (purple), $N_{\text{INP},-16}$ (blue), $N_{\text{INP},-12}$ (green), and $N_{\text{INP},-8}$ (magenta) are given in Fig. 4.12a-e, respectively. INP concentrations outside the detectable range, estimated as described in section 3.3.3, are indicated in the figure (triangles) by each filter's lowest (lower detection limit) and highest resolvable concentration value (upper concentration limit). Measurement uncertainties (indicated by error bars) become smaller with decreasing temperature (see section 3.3.3). At $-12\,°\text{C}$ and $-16\,°\text{C}$, INP number concentration show the highest variability of around 3 orders of magnitude. At $-8\,°\text{C}$ and $-20\,°\text{C}$ the variability decreases to about 2 orders of magnitude, while INP number concentration at $-24\,°\text{C}$ only varies within 1 order of magnitude. A bias arises from the values being close to or above the upper detection limit, decreasing the range of values. Each of the shown time series of INP number concentration in Fig. 4.12 contains episodes of elevated INP concentrations, coinciding with the RV being close to land (within $200\,\text{km}$; grey area) and harbours (dashed line). During the open ocean sections of the cruise the majority of data points shows up to 2 orders of magnitude lower concentrations (e.g. $N_{\text{INP},-16} = 0.1\text{--}10\,\text{m}^{-3}$). This suggests that elevated atmospheric INP concentrations are connected to terrestrial (including coastal) INP sources. Without a tracer for terrestrial influences, e.g. measurements of ambient radon concentrations as in McCluskey et al. (2018a), direct assessment of the air-mass origin is not possible for ACE and the aforementioned connection will only be done indirectly, using backward-trajectory analysis, in subsection 4.2.2. For comparison, Fig. 4.12c contains the range between the 5th and 95th percentile of $N_{\text{INP}-15}$ from Bigg (1973) (orange area). They sampled filters in the SO around Australia, collecting 0.3 and $3\,\text{m}^3$ of ambient air through a pair of membrane filters. In terms of sampling strategy, the LV sampling of $12\,\text{m}^3$ through a porous filter over 8 h compares well with the sampling of Bigg (1973). The derivation of INP number concentrations however was fundamentally different, with ACE's samples being analysed with a freezing array method (subsection 3.3.3) and Bigg (1973) relying on a thermal diffusion chamber. In the supporting information (SI) of McCluskey et al. (2018a), the effect of background INP number concentrations during the study of Bigg (1973) is assessed and a correction proposed (22 % lower values). This correction was applied to the values shown in Fig. 4.12c. The majority of $N_{\text{INP},-16}$ measurements during ACE are in the open ocean sectors and clearly below the range of $N_{\text{INP},-15}$ observed by Bigg (1973). However, $N_{\text{INP},-16}$ larger than $10\,\text{m}^{-3}$ at the end of Leg 1, when the RV was close to Australia, lie within the range of values given in Bigg (1973). In McCluskey et al. (2018a) INP measurements from CAPRICORN-1 are presented. The range of observedINP concentrations is included in Fig. 4.12 for comparison (light blue). At each temperature, INP number concentration observed during ACE are at the upper end or higher than concentrations observed during CAPRICORN-1, except at $-16\,°\text{C}$ when low concentrations were measured on the open ocean in air-masses without terrestrial influence. Differences in sampled geographical area (CAPRICORN-1: 43–53°S and 141–151°E; ACE: 34°–78°S and circum-Antarctic) and season (CAPRICORN-1: March–April; ACE: December–March) could be reasons for the differences in observed INP abundance. Findings for ACE are consistence with preliminary results for MARCUS, CAPRICORN-1, and CAPRICORN-2 in McFarquhar et al. (2020), where INP number concentrations in the MBL over the SO are shown to exhibit a large variability, very low overall values and a weak overall latitudinal dependence. Further, the highest concentration were found near land and values differed largely from historical measurements (e.g. Bigg, 1973). Feedback of the Earth's changing climate on INP in the SO region as a contributor to the observed difference between current and historical observations cannot be ruled out (e.g. Bigg, 1990). However, potential mechanisms behind such a hypothetical feedback have not been identified either, to the best of our knowledge. For completeness, the spatial variability of $N_{\text{INP},-16}$ during ACE and $N_{\text{INP},-15}$ from Bigg (1973) are shown in Fig. B.2c.

   PDF of INP number concentration at selected temperatures are shown in Fig. 4.13. Values of INP number concentration outside of the detectable range (triangles in Fig. 4.12) are not considered for the PDF. As indication for the detectable range, averages for the upper and lower concentra-

tion limit are indicated in Fig. 4.13c–e (dashed line). Interpretation of the PDF for $N_{\mathrm{INP},-8}$ and $N_{\mathrm{INP},-24}$ is omitted due to the low number of samples compared to other temperatures and concentrations being close to the FBF results (Tab. B.3), respectively. Also for the other temperatures, the overall number of samples considered in the PDF is small. The following discussion has to be considered semi-quantitative in consequence. The $N_{\mathrm{INP},-12}$ and $N_{\mathrm{INP},-16}$ PDF (Fig. 4.13c,d) are tri-modal and the $N_{\mathrm{INP},-20}$ PDF (Fig. 4.13b) is bi-modal. The first mode for $N_{\mathrm{INP},-12}$ and $N_{\mathrm{INP},-16}$ contains concentrations below $0.2\,\mathrm{m}^{-3}$, which are on the lower boundary of the detectable range. Attributing these concentrations to a source or geographical origin is ambiguous when considering the FBF as a point of reference for the background freezing signal. FBF concentrations are 0.08 and $0.59\,\mathrm{m}^{-3}$ for $-12\,°\mathrm{C}$ and $-16\,°\mathrm{C}$, respectively (Tab. B.3). Consequently, I only discuss the two highest concentration modes in the following. The second (first) mode of the $N_{\mathrm{INP},-12}$ and $N_{\mathrm{INP},-16}$ ($N_{\mathrm{INP},-20}$), referred to as "low concentration mode" in the following, covers a range of concentration values (e.g. $N_{\mathrm{INP},-16} = 0.3\text{–}10\,\mathrm{m}^{-3}$) encountered mainly during the open ocean sections of the cruise (Fig. 4.12b–d). Results of the air-mass origin (see subsection 4.2.2) show that INP in this mode are mainly of marine origin, potentially including long-range transported terrestrial or coastal INP. In consequence, this mode is labelled "open ocean" (light blue area) in Fig. 4.13b-d. Moallemi et al. (2021) show that fluorescent primary biological aerosol particle (PBAP) measured during ACE's open ocean sections originate mainly from SSA. In marine regions of the Northern hemisphere, PBAP were found to act as INP (e.g. McCluskey et al., 2018b; Hartmann et al., 2021) and it is assumed to be the same for the Southern hemisphere. Consequently, PBAP from SSA are a potential source for the INP measured during the open ocean sections of ACE. This is further discussed in section C.5. The high concentration mode in the PDF of $N_{\mathrm{INP},-12}$, $N_{\mathrm{INP},-16}$, and $N_{\mathrm{INP},-20}$ consists of values (e.g. $N_{\mathrm{INP},-16} = 10\text{–}100\,\mathrm{m}^{-3}$) measured close to land (Fig. 4.12b–d). This mode has a greater terrestrial and coastal influence than the low concentration mode, based on the results of the air-mass origin analysis in subsection 4.2.2. In consequence, the high concentration mode is labelled "terrestrial/coastal" in Fig. 4.13b-d (yellow area). A further distinction, whether the source of these INP is on the continents or the respective coastal regions, is not possible. In Fig. 4.13c, a PDF of $N_{\mathrm{INP},-15}$ from Bigg (1973) is included for reference (orange line). Here, only a subset of the total of 126 data points from Bigg (1973) is shown, containing the 58 data points south of 43°S, mimicking the latitudinal range of the ACE cruise for a better comparison (see Fig. B.2). Again the disagreement between measurements during ACE and those described in Bigg (1973) can be seen, as discussed earlier for Fig. 4.16c. Agreement of their values is highest with the subset of our observations in the proximity to land. One possible explanation is the decrease in INP abundance over the SO due to changes in INP transport or weather systems as a result of Earth's changing climate (Bigg, 1990). In Bigg (1990), average INP number concentrations are lower than what is shown in Bigg (1973).

Welti et al. (2018) presented PDF of $N_{\mathrm{INP}}(T)$ based on filters sampled at a fixed location on the Cabo Verde island of Sao Vicente over a four year period (2009–2013). The PDF comprise changes in season, air-mass origin, and bulk aerosol composition. The respective PDF of $N_{\mathrm{INP},-16}$, $N_{\mathrm{INP},-12}$, and $N_{\mathrm{INP},-8}$ are included for comparison in Fig. 4.13c–e. Welti et al. (2018) found log-normal distributions for all temperatures, and attributed them to random dilution during transport, indicating a lack of strong local sources. In other words, the PDF are thought to represent background INP number concentrations at the Cabo Verde islands. Comparing PDF, it can be seen that for $N_{\mathrm{INP},-16}$ the bulk of our values is below what is reported in Welti et al. (2018), shifted by roughly 1 order of magnitude towards lower concentrations. For $N_{\mathrm{INP},-12}$ a respective shift is not as clearly seen, however a tendency towards more frequent occurrence of higher concentrations compared to our study is obvious. For $N_{\mathrm{INP},-8}$ this tendency is not visible anymore. The difference between the PDF given in Welti et al. (2018) and our study for $N_{\mathrm{INP},-12}$ and $N_{\mathrm{INP},-16}$ illustrates the latitudinal difference in marine INP number concentration with lower concentrations in the SO compared to the Atlantic.

Averaging of the INP number concentration at selected temperatures has been performed, in order to showcase typical values for the SO region. A summary of average INP number concentrations

for Legs 1–3 at selected temperatures is given in Tab. B.2. Two different approaches were used for averaging the INP number concentrations. In the first approach only values which are inside the detectable range are considered and the results are given as $N_{\mathrm{INP}}$. For the second approach, values outside the detectable range were included by using a value on the edge of the detectable range instead (see section 3.3.3) and the results are given as $N_{\mathrm{INP}}^{\star}$. Results of the two approaches differ in mean, median, and geometric mean values by up to $\pm 50\,\%$. The largest differences were found at $T$ of $-8\,°\mathrm{C}$ and $-24\,°\mathrm{C}$, where the number of data points outside the detectable range is largest. All averaged values are reported in the following with explicit reference to their potential biases. Average values of $N_{\mathrm{INP},-24}$, $N_{\mathrm{INP},-20}$, $N_{\mathrm{INP},-16}$, $N_{\mathrm{INP},-12}$ and $N_{\mathrm{INP},-8}$, sorted by Legs, are given in Fig. 4.14. Values were determined including the estimates for INP concentrations outside the detectable range (triangles in Fig. 4.12). As a point of reference for the measurement background, concentrations of the averaged FBF are included (dash-dotted lines). Differences in median values between different Legs are largest at $-20\,°\mathrm{C}$, however still within the respective IQR. Mean values (crosses in Fig. 4.14) are higher than the median and outside of the IQR for all temperatures other than $-24\,°\mathrm{C}$.

In addition to the temporal (Fig. 4.12) and quasi-longitudinal (Fig. 4.14) distribution of INP number concentrations presented earlier, the latitudinal dependence of $N_{\mathrm{INP}}$ is given in Fig. 4.15. INP number concentrations were averaged based on the latitude of the midpoint between locations where sampling started and ended, using $5°$ bins. Due to the inclusion of values outside the detectable range, the averaging produces no meaningful results for $-8\,°\mathrm{C}$, $-12\,°\mathrm{C}$ and $-24\,°\mathrm{C}$. For $N_{\mathrm{INP},-20}$ and $N_{\mathrm{INP},-16}$, overall lower concentrations towards the South Pole occurred. Data on INP abundance gathered during ACE are featured in Welti et al. (2020) and form an integral part for a global view on marine INP concentrations. In Welti et al. (2020), a trend of decreasing INP number concentration from the equator towards both poles is presented, which is consistent with the decrease in $N_{\mathrm{INP},-16}$ and $N_{\mathrm{INP},-20}$ in Fig. 4.15b,c.

The temperature spectra of INP number concentration for all LV samples are presented in Fig. 4.16a and show the highest freezing onset to be at a temperature of around $-4\,°\mathrm{C}$. Between filters, INP number concentration spreads up to 3 orders of magnitude for individual $T$. The steepness of the curves in the temperature spectra can be used as indication for the closeness of the sample to a potential INP source (e.g. Hartmann et al., 2019, 2021). By taking the steepness of the FBF curve (pink line) as a point of reference for the continuous increase in INP number concentration with $T$ of the background INP concentrations (1 order of magnitude per $5\,\mathrm{K}$), a few samples in Fig. 4.16a show a steeper curve than the FBF. These curves are characterised by exceeding $10\,\mathrm{m}^{-3}$ at $-16\,°\mathrm{C}$. A high concentration of INP above $-15\,°\mathrm{C}$ is typically associated with a signal of a biological INP source (e.g. Creamean et al., 2019). The range of values for CAPRICORN-1 from McCluskey et al. (2018a) is included in Fig. 4.16a for comparison (light blue). As noted above, only the lowest curves of ACE lie within the range observed by McCluskey et al. (2018a), who found general lower concentrations on the SO. Potential reasons are given in the discussion of Fig. 4.12.

In order to test the hypothesis that typical marine INP (e.g. SSA) were encountered for the majority of the cruise, INP number concentration values were normalised. This was achieved by dividing INP number concentration by the particle surface area concentration or the particle volume concentration derived from the total PNSD under the assumption of spherical particles (see section 3.3.3). Normalisation enables comparison of INP properties across different studies, which can include different INP number concentration derivation approaches or sampled particle size ranges, independent of INP number concentration. The resulting spectra of ice-active site density, $n_{\mathrm{s}}$, and ice-active volume density, $n_{\mathrm{v}}$, are given in Fig. 4.16b,c. Values of $n_{\mathrm{s}}$ spread over 4 orders of magnitude ($0.1$–$1000\,\mathrm{cm}^{-2}$) in the observed temperature range. For comparison, values from two laboratory experiments are included in Fig. 4.16b, that focused on sampling of artificially generated SSA and assessing its ice-activity (DeMott et al., 2016; Mitts et al., 2021). The results from DeMott et al. (2016) span a wider range of $n_{\mathrm{s}}$ and $T$ than the ACE data, while values from Mitts et al. (2021) overlap with the open ocean-sampled filters from ACE. Field measurements from CAPRICORN-1 (McCluskey et al., 2018a) showing a large variability in $n_{\mathrm{s}}$, are included for comparison. Contrary

to INP number concentration (Fig. 4.16a), $n_{\mathrm{s}}$ values from ACE lie within the lower end of what is reported from CAPRICORN-1. This indicates observation of a similar or more ice-active particle population during CAPRICORN-1 compared to ACE and mirrors what was found for INP number concentration (Fig. 4.16a). The range of $n_{\mathrm{v}}$ reported in Mitts et al. (2021) are included in Fig. 4.16c for comparison. The range overlaps with the lower range of the values from ACE. In conclusion, the strong overlap between ice-active site density profiles from ACE (derived from INP number concentration) and studies of artificial SSA (e.g. DeMott et al., 2016; Mitts et al., 2021) supports the idea that low INP number concentration measured on the open ocean might be driven by SSA.

For completeness, temperature spectra of INP number concentration for all HV samples of ACE are presented in Fig. C.3 and differences compared to the LV sampling results are discussed in section C.3.

## 4.2.2 Air-mass origin for INP measurements

Using the backward-trajectories available for ACE, I analysed the air-mass origin for the INP data of the LV samples in a similar way to what I did for the (hourly) CCN data (see subsection 4.1.4). As described in subsection 3.4.3, the coarser temporal resolution of the LV sampling (8 h) is accounted for by calculating each contribution (e.g. the duration within the FT for a given averaged trajectory, $f_{\mathrm{FT}}$) over all (hourly) trajectory clusters within the sampling period of one LV filter. Here, the averaging of up to eight trajectory clusters, which have maximum possible duration of 10 d each, results in a combined maximum duration of 1920 h. The results of this analysis for the LV sampling intervals are presented in Fig. 4.17 and show, on first glance, trends that are similar with the results at hourly resolution (Fig. 4.8). Differences arise mainly from the additional averaging needed to achieve coarser temporal resolution. Similarities between the 1 h and 8 h analyses include a highly variable number of considered time steps (Fig. 4.17a), the occurrence of extended periods of a strong influence of the FT (Fig. 4.17b), a dominance of oceanic origin in the PBL influences (Fig. 4.17c), and the majority of oceanic air-masses stemming from north of 60°S (Fig. 4.17d).

Results of this analysis were averaged over the full duration of the cruise and its respective Legs. The averaged contributions are shown in Fig. 4.18 and visually resemble what is shown for the whole cruise and its Legs at hourly resolution in Fig. 4.9 (see subsection 4.1.4). The threshold in $d_{\mathrm{land}}$ of 200 km proposed in Moallemi et al. (2021) and presented in subsection 4.1.1 (e.g. Fig. 4.2b) is tested here in terms of the air-mass origin. The data set was divided using the 8 h median in $d_{\mathrm{land}}$ and the results are 116 cases of pristine marine conditions (PM, $d_{\mathrm{land}} > 200$ km) and 99 cases of terrestrial-influenced conditions (TI, $d_{\mathrm{land}} \leq 200$ km). Average surface distributions for PM and TI are included in Fig. 4.18 and show that the PBL influence is nearly equal for both conditions (Fig. 4.18a). However, TI are less oceanic ($\sim$80 %) compared to PM ($\sim$95 %). However, the ratio between terrestrial and coastal influence is equal in both cases. As for the geographical origin of the air-masses (Fig. 4.18c), TI and PM show a similar contribution for non-SO oceanic influence of 60 % and differ in oceanic influence from the SO. The terrestrial influence for TI stems mainly from Antarctica and to a lesser degree from South America, while for PM the small terrestrial influence originates only from Antarctica. To investigate the classification of encountered INP conditions based on sampling-location, as highlighted in the PDF in Fig. 4.13c, the data set was divided using a threshold in $N_{\mathrm{INP},-16}$ of 10 m$^{-3}$. For conditions with elevated $N_{\mathrm{INP},-16}$, a far higher combined terrestrial and coastal influence (40 %) is apparent in comparison to low $N_{\mathrm{INP},-16}$ conditions (10 %). This underlines the conclusions I made in subsection 4.2.1 that the elevated INP number concentration encountered close to land are connected to terrestrial-influenced air-masses.

Measured INP number concentrations at different $T$ as a function of free tropospheric, terrestrial, Antarctic, oceanic and sea ice influence are presented in Fig. 4.19. Due to the median values lying within respective IQR for different $f$, it is apparent that INP abundance is independent of the duration that the air-mass was in the FT (Fig. 4.19a), over Antarctica (Fig. 4.19c), and over ice-covered surfaces (Fig. 4.19e). In contrast, median values of INP number concentration as a function of $f_{\mathrm{TR}}$ are presented in Fig. 4.19b. For all shown $T$, an increase in INP number concentration with increasing $f_{\mathrm{TR}}$ is apparent. For $N_{\mathrm{INP},-16}$, values increase from 1 m$^{-3}$ ($f_{\mathrm{TR}} = 0$) to 10 m$^{-3}$

($f_{\mathrm{TR}} > 0.3$). For $f_{\mathrm{TR}} > 0.3$, number of samples values are low and INP number concentration median values are highly variable. Median values of INP number concentration as a function of $f_{\mathrm{OC}}$ are presented in Fig. 4.19d. $N_{\mathrm{INP}}$ at any $T$ are highly variable for different $f_{\mathrm{OC}}$, which could be the result of either a weak or a highly variable oceanic influence on the INP abundance. In summary, this supports the importance of long-range transport for the INP population over the SO.

## Summary

In summary, elevated $N_{\mathrm{INP}}$ were found in the vicinity of land and a lower, broader range of values was encountered on the open ocean. Generally, $N_{\mathrm{INP}}$ decreased towards Antarctica. Close to inhabited land-masses, the increased INP abundance is connected to terrestrial and/or coastal sources. For the open ocean sections, INP number concentrations is driven by local oceanic sources (i.e. SSA) and/or long-range transport.

## 4.3 Chemical composition of sampled aerosol particles

Information on the chemical composition of aerosol particles is widely used to infer the origin of the sampled population (Seinfeld and Pandis, 2006). The abundance of specific compounds is used as indication for the source's strength. To aid the characterisation of CCN and INP sources over the SO, sampled HV filters were analysed regarding the aerosol load ($PM_{10}$ mass) and the atmospheric particle mass concentrations, $M$, of OC, EC, WSOC, ammonium ($NH_4^+$), potassium ($K^+$), sodium ($Na^+$), magnesium ($Mg^{2+}$), calcium ($Ca^{2+}$), MSA, chloride ($Cl^-$), bromide ($Br^-$), nitrate ($NO_3^-$), sulphate ($SO_4^{2-}$), nss sulphate (nss-$SO_4^{2-}$), and oxalate ($C_2O_4^{2-}$) as described in subsection 3.3.4. The results of these analyses are presented in Tab. B.4 as median values of $M$ and respective IQR for the whole cruise and individual Legs. To prevent sampling of stack exhaust air, an automated shut-down of the HV sampler was achieved via monitoring of the wind direction, as described in subsection 3.3.1. Quantification of this approach's effectiveness is attempted by primarily using EC as a proxy for combustion products in the stack's exhaust air (see subsection 3.3.4). Using threshold values in EC ($0.07\,\mu g\,m^{-3}$) and WSOC ($0.5\,\mu g\,m^{-3}$), four days (23 December 2016, 24 December 2016, 8 February 2017, and 26 February 2017) have been identified that each show clean conditions with a weak influence of the stack exhaust. The median value over these four days for each identified compound is included in Tab. B.4 under "golden days". Differences between the golden days and the whole cruise median values are small for the majority of identified compounds, except OC, EC, and WSOC. However, 2 orders of magnitude between the whole cruise ($0.460\,\mu g\,m^{-3}$) and the golden days median ($0.007\,\mu g\,m^{-3}$) for $M_{\mathrm{nss\,SO_4^{2-}}}$ indicate that the stack exhaust's signal is included in the results of this analysis. Sodium and MSA mass concentrations are known to be unaffected by stack exhaust air (see subsection 3.3.4). In consequence, only total aerosol load and mass concentrations for sodium and MSA are discussed in the following. For the remainder of identified compounds, particle mass concentrations are given for completeness in Tab. B.4.

On average, $32.4\,\mu g\,m^{-3}$ (median; IQR: $26.1$–$49.6\,\mu g\,m^{-3}$) of $PM_{10}$ were observed during ACE (Tab. B.4). Leg 1 exhibits a higher median value ($42.4\,\mu g\,m^{-3}$) compared to Leg 2 and Leg 3 ($31.1\,\mu g\,m^{-3}$ and $33.3\,\mu g\,m^{-3}$).

Averaging $M_{Na^+}$ for the whole cruise gives a median value of $2.8\,\mu g\,m^{-3}$, with an IQR from 1.8 to $3.9\,\mu g\,m^{-3}$ (Tab. B.4). Higher median values for Legs 1 and 3 compared to Leg 2 are found, similar to what is observed for $PM_{10}$. This is consistent with Blanchard and Woodcock (1957) showing SSA production to be driven by wave breaking and Schmale et al. (2019) showing on average higher wind speeds and significant wave heights for the Legs with extended open ocean sections (Leg 1 and Leg 3). For the 34th Chinese National Antarctic and Arctic Research Expedition (CHINARE) cruise, aerosol characterisation was performed on the SO (40°–76°S, 170°E–110°W) in February–March 2018. Yan et al. (2020c) report a $M_{Na^+}$ average of $0.8\pm0.8\,\mu g\,m^{-3}$ (mean$\pm$SD) for CHINARE. During Leg 2 of ACE, the part of the cruise that overlaps with the region covered by CHINARE the most, the $M_{Na^+}$ median was $1.8\,\mu g\,m^{-3}$, i.e. more than two times higher than that observed during CHINARE.

MSA mass concentrations were generally 2 and 1 order of magnitude lower than the ones for $PM_{10}$ and sodium, respectively. Consequently, values are reported in ($ng\,m^{-3}$) in the following. A $M_{MSA}$ median of $102\,ng\,m^{-3}$ for the entire ACE cruise was found (Tab. B.4), with highly variable values ranging from 1 to $455\,ng\,m^{-3}$. Differences in median values between Legs are small. The mass concentration maximum of $455\,ng\,m^{-3}$ was observed during Leg 2, on the Ross Sea and close to the sea ice edge at around 70°S. Comparing our measurements of $M_{MSA}$ with historical records, Davison et al. (1996) report for south of the Falkland islands in November 1992 a mean concentration of $27\,ng\,m^{-3}$, with values ranging up to $99\,ng\,m^{-3}$. During ACE in late February of 2017, values around $120\,ng\,m^{-3}$ were found in this part of the SO between 70 and 36°W. Besides long-term trends over the last two decades, the difference of up to 1 order of magnitude might be due to the difference in season, with higher $M_{MSA}$ for ACE due to increased marine biological activity in early fall compared to late fall for Davison et al. (1996). Another factor is the large degree of variability in MSA abundance across the SO, depending on season and location as illustrated in Castebrunet et al. (2009), with values during ACE on the higher end of the scale. For a number of CHINARE

Antarctic cruises, $M_{\mathrm{MSA}}$ are reported. Yan et al. (2020b) report for the polynya regions of the Ross Sea (50–70°S, 160–185°E) an average value of $44 \pm 22\,\mathrm{ng\,m^{-3}}$ (mean $\pm$ SD) for December 2017 and $39 \pm 28\,\mathrm{ng\,m^{-3}}$ for January 2018. The $M_{\mathrm{MSA}}$ maximum of $211\,\mathrm{ng\,m^{-3}}$ was reported for the Ross Sea, at around 64 to 67°S, connected to the position of the dynamic sea ice edge at ∼64°S. Here, with the start of the sea ice melt in early December, the release of iron from ice into the water can spur marine microbial activity (Turner et al., 2004), that may result in an increased DMS emission and consequently secondary MSA production. Consistently, the maximum MSA mass concentration during ACE was encountered near the sea ice edge on the Ross Sea. For the Amundsen Sea (40–76°S, 170°E–110°W) in February–March 2018 ($34^{\mathrm{th}}$ CHINARE cruise), average $M_{\mathrm{MSA}}$ of $31 \pm 17\,\mathrm{ng\,m^{-3}}$ are reported in Yan et al. (2020c). The ACE cruise went on the Amundsen Sea in early February 2017 and MSA mass concentrations in this region show a median value of $210\,\mathrm{ng\,m^{-3}}$. Overall, a difference in average MSA mass concentrations of up to 1 order of magnitude between ACE and the CHINARE cruises becomes apparent. One factor might be the usage of different instrumentation and analysis techniques. Another factor, playing into the year-to-year variability, might be the presence of sea ice. Schmale et al. (2019) note a significantly lower sea ice extent on the Amundsen Sea during ACE, when compared to climatological records. The lack of a sea ice cover enables marine activity and the emission of aerosol precursors into the air. Adding to the encountered variability in MSA are besides aforementioned sources also the atmospheric sinks, e.g. precipitation that is associated with frontal zones and efficiently removes MSA from the atmosphere, increasing the observed variability. For South Georgia, a sub-micron ($\mathrm{PM_1}$) MSA mass concentration of up to $200\,\mathrm{ng\,m^{-3}}$ was reported in Schmale et al. (2013). During ACE, the RV was on station close to this island in the beginning of March 2017, with MSA mass concentrations around $75\,\mathrm{ng\,m^{-3}}$ during these days, underlining the high variability in MSA abundance on the SO.

## Summary

In summary, sodium and MSA were the only compounds for which the abundance throughout the cruise were characterised along with the $\mathrm{PM_{10}}$ mass. This selection is the result of a tracer indicating that a stack exhaust signal contribution was present for the remainder of measured compounds. Sodium particle mass concentrations were found to vary in a way that the highest values coincided with the highest $\mathrm{PM_{10}}$ mass and strongest wave activity. MSA abundance was found to be highly variable on the SO, with peak particle mass concentrations near the sea ice edge. $M_{\mathrm{MSA}}$ for ACE differ up to 2 orders of magnitude from what other studies reported for the SO region, underlining a strong variability.

## 4.4 Correlation analysis

The results of a correlation analysis performed with a selection of variables gathered during ACE is given as a Spearman correlation matrix in Fig. 4.20.

With regards to the results of the in situ aerosol particle measurements, $N_{\text{total}}$ was found to be correlated with $N_{\text{mode1}}$ (Spearman's rank correlation coefficient $R_{\text{S}}$ of 0.9, Spearman p-value of $< .001$) and $N_{\text{CCN},1.0}$ ($R_{\text{S}} = 0.8$, $p < .001$). This mirrors the behaviour these quantities show in Fig. 4.2a, and is indicative for the importance of Aitken mode particles for the total particle and CCN number concentrations at high $SS$.

Correlations between sodium and mode 3 ($R_{\text{S}} = 0.7$, $p < .001$) as well as PM$_{10}$ ($R_{\text{S}} = 0.7$, $p < .001$) concentrations were found. As sodium is used as a conservative tracer for primary aerosol particles of marine origin (Legrand and Pasteur, 1998), especially sea salt, the correlations suggest that SSA significantly contributes to both, PM$_{10}$ and the coarse mode. However, we do not find a significant correlation between wind speed at $10\,\text{m a. s. l.}$ ($U_{10}$) and sodium mass concentration. Bates et al. (1998b) attributed this kind of observation to the fact that the instantaneous wind speed at the RV is not representative for the conditions an air parcel experienced prior to its measurement. It is worth mentioning, that other studies on the SO found correlation between wind speed and sodium mass concentrations (e.g. Schmale et al., 2013; Yan et al., 2020a; Landwehr et al., 2021). Another factor might be, that the wind speed was averaged over $24\,\text{h}$, in order to match the temporal resolution of the filter sampling. Possible short term effects might be lost due to the averaging process. I investigated this by means of an additional correlation analysis at hourly resolution and found only small differences for the in situ measurement results (see section C.4).

The particle concentration of mode 2 shows a positive correlation ($R_{\text{S}} \approx 0.7$) with $N_{\text{CCN}}$ at $SS \leq 0.5\,\%$, pointing at the importance of accumulation mode particles for the CCN population at atmospheric relevant $SS$. No correlation was found between CCN number concentration and mode 3 number concentrations, suggesting little influence of SSA on the CCN population probed with our $SS$.

No correlation between CCN number concentration and MSA concentration was found. This seemingly contradicts findings of previous studies (e.g. Ayers and Gras, 1991) and our observations of the highest CCN number concentration (subsection 4.1.2) and the highest MSA mass concentration (section 4.3) occurring near the coast of Antarctica. The highest $M_{\text{MSA}}$ have been investigated as case studies in Appendix D. However, it might be a smearing effect due to averaging and finding no correlation with our method does not imply that there could not be a connection under specific conditions and/or shorter time scales.

Furthermore, no correlation between CCN number concentration and in-water Chl $a$ or DMS concentration could be found, which is in line with Ayers et al. (1997). Considering the long process chain from in-water DMS to particles of CCN size this is not surprising and the argument that conditions at measurement point must not be representative for the conditions encountered by the air-parcel during transport in Bates et al. (1998b) is very likely applicable.

Looking at $\kappa$ values, high correlation between different levels of supersaturation (except $SS = 1\,\%$) could be found, mirroring the lack of size-dependent composition presented in subsection 4.1.3. Further, no correlation between sodium mass concentration and $\kappa$ values was found, showing that the chemical information approximated by $\kappa$ is not connected to the mass-dominated results of the analysis of sodium and MSA. This again supports the observation of SSA particles not significantly contributing to the CCN population, as SSA dominates the sampled particle mass but not the particle number.

No correlations with any other variable was found for the MSA concentration. This includes the absence of the correlation between MSA and in-water DMS concentration. Although MSA is known to form exclusively from oxidation of DMS in the atmosphere (Sorooshian et al., 2007), a direct correlation is not expected. In-water DMS concentrations are not representative of DMS concentrations in the atmosphere (Ayers et al., 1997) and DMS has an atmospheric lifetime of several days over the SO (Chen et al., 2018).

INP number concentrations measured at a temperature difference ($\Delta T$) of $4\,\text{K}$ showed positive

correlation ($R_{\mathrm{S}} > 0.6$). This is expected, since these concentrations are cumulative along the temperature axis (see Fig. 4.20) and could indicate a common source that contributes INP over the $T$ range. For $\Delta T \geq 8\,\mathrm{K}$, only $N_{\mathrm{INP},-12}$ and $N_{\mathrm{INP},-20}$ show a correlation ($R_{\mathrm{S}} = 0.7$, $p < .001$). This correlation between INP number concentrations at $-12\,^{\circ}\mathrm{C}$ and $-20\,^{\circ}\mathrm{C}$ points at the importance of long-range transport and mixing influencing the INP population in the same way at both temperatures (Welti et al., 2018). The in-water Chl $a$ concentrations were also included in the correlation analysis, as it can be used as a proxy for biological activity (e.g. McCluskey et al., 2018a). However, no direct correlation between INP number concentration and Chl $a$ was found. This suggests that the measured INP are not originating from local biogenic sources but does not exclude a delayed connection. In DeMott et al. (2010) a parameterisation for INP number concentration is given that is based on $N_{>500}$. No correlation is found between measured $N_{\mathrm{INP}}$ and $N_{>500}$, showing that a parameterisation based solely on $N_{>500}$ is not applicable for the SO. No significant correlations were found between INP number concentration and $\mathrm{PM}_{10}$, $N_{\mathrm{total}}$ or any other physical and chemical properties measured. This clearly shows that trying to derive INP-related properties from bulk number-based or bulk mass-based aerosol properties without considering air-mass history might lead to results not representative for atmospheric INP number concentrations. Instead, $N_{\mathrm{INP}}$ must be compared with results from methods selective to individual, rare particle types that could act as INP and the data must be segregated in terms of air-mass properties (see subsection 4.2.2) or some other, more specific INP tracers such as mineral dust or proteins, to further elucidate INP sources.

## Summary

In summary, the correlation analysis showed that the particle mass was mainly driven by sodium and coarse mode particles, while the abundance of CCN was dominated by Aitken (high $SS$) and accumulation mode particles (lower $SS$). Regarding potential primary origin of CCN, an only small impact of SSA on the population was underlined. As for a secondary origin of CCN, no direct connection between CCN number concentration and MSA mass concentration was found. However, an indirect or time-delayed influence was not investigated. The INP abundance showed mainly intra-temperature correlations, indicative of a mixed (biogenic and mineral), long-range transported INP population.
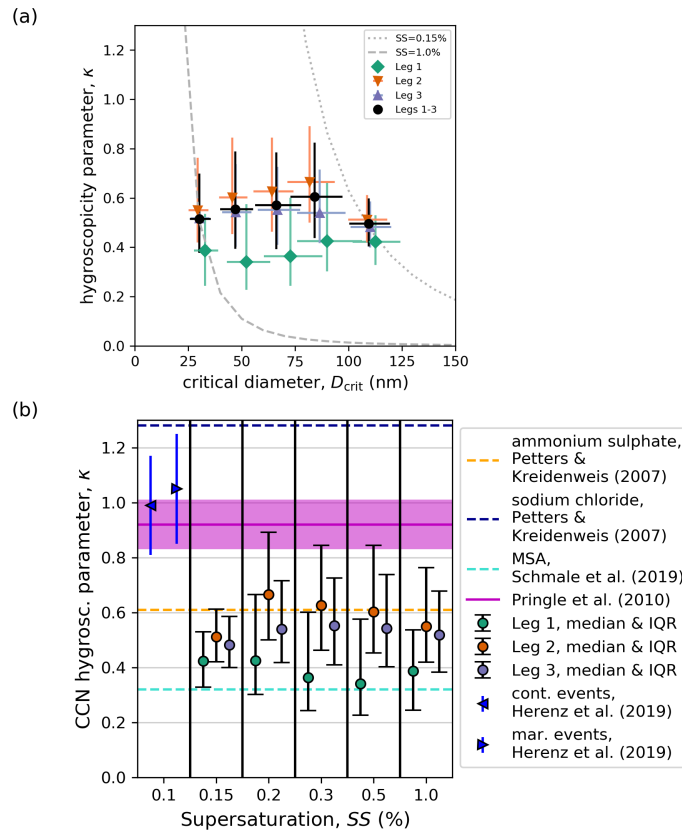
**Figure 4.6:** (a) Median values and respective IQR of aerosol particle hygroscopicity parameter ($\kappa$) for Leg 1 (green), Leg 2 (orange) and Leg 3 (purple), respectively. Additionally, $\kappa$ is given as a function of critical dry diameter ($D_{\text{crit}}$) in (b). All $\kappa$ values resulting from $D_{\text{crit}}$ values outside of $10^{\text{th}}$ to $90^{\text{th}}$ percentile range for $D_{\text{crit}}$ (per $SS$) are excluded here. As reference, $\kappa$ mean values for sodium chloride (dashed black line) and ammonium sulfate (dashed orange line) from Petters and Kreidenweis (2007), and a hypothetical $\kappa$ value for MSA from Schmale et al. (2019) (dashed teal line) are given in (a). Averages for Antarctica from Herenz et al. (2019) for cases of continental (triangle pointing left) and marine events (triangle pointing right) are given. Modelled $\kappa$ values for the Southern Ocean's surface layer (magenta line and area) from Pringle et al. (2010) for reference.
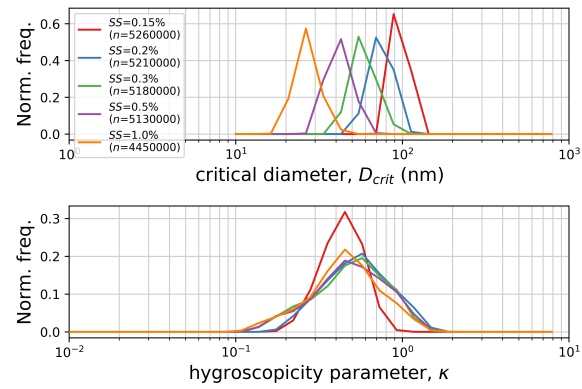
**Figure 4.7:** Normalized PDF of (a) critical dry diameter $D_{\mathrm{crit}}$ and (b) hygroscopicity parameter $\kappa$ for level of supersaturation $0.15\,\%$, $0.2\,\%$, $0.3\,\%$, $0.5\,\%$ and $1\,\%$ (colour-coded) for Legs 1–3. $D_{\mathrm{crit}}$ and $\kappa$ from MCS runs ($n_{\mathrm{MCS}} = 10^4$) of hourly mode-fitted PNSD. $D_{\mathrm{crit}}$ values (and resulting $\kappa$) outside of $10^{\mathrm{th}}$ to $90^{\mathrm{th}}$ percentile range (per $SS$) excluded. The number of samples is indicated ($n$).
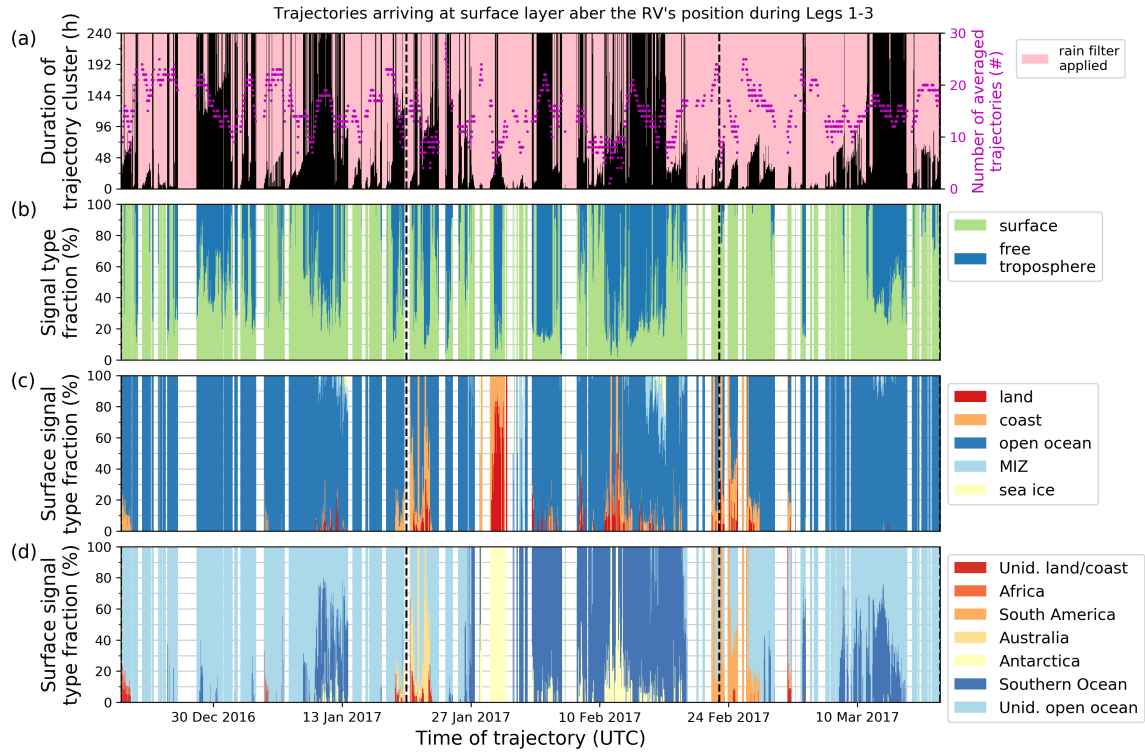
**Figure 4.8:** Results of the analysis of the backward-trajectories for ACE regarding potential aerosol particle source signals. The time of potential signal pick-up for each trajectory (black) and the part of the trajectory that is dismissed as a result of the applied rain filter (red) is shown in (a). In addition, the number of averaged trajectories per time step is given for consistency (magenta). The normalised contribution of surface (green) and free tropospheric signal (blue) for each trajectory using the model's planetary boundary layer height in (b). Surface signal specification using the model's land-sea mask and sea ice fraction ($f_{SI}$) to into land (red), coast (orange), open ocean ($f_{SI} \leq 15\%$; dark blue), marginal ice zone ($15\% < f_{SI} \leq 80\%$; light blue), and sea ice ($f_{SI} > 80\%$; yellow) signal in (c). Information on the geographical position in (d) using the polygons for Africa, South America, Australia and Antarctica in Radenz et al. (2021). The 10-day backward-trajectories for ACE are available in Thurnherr et al. (2020).
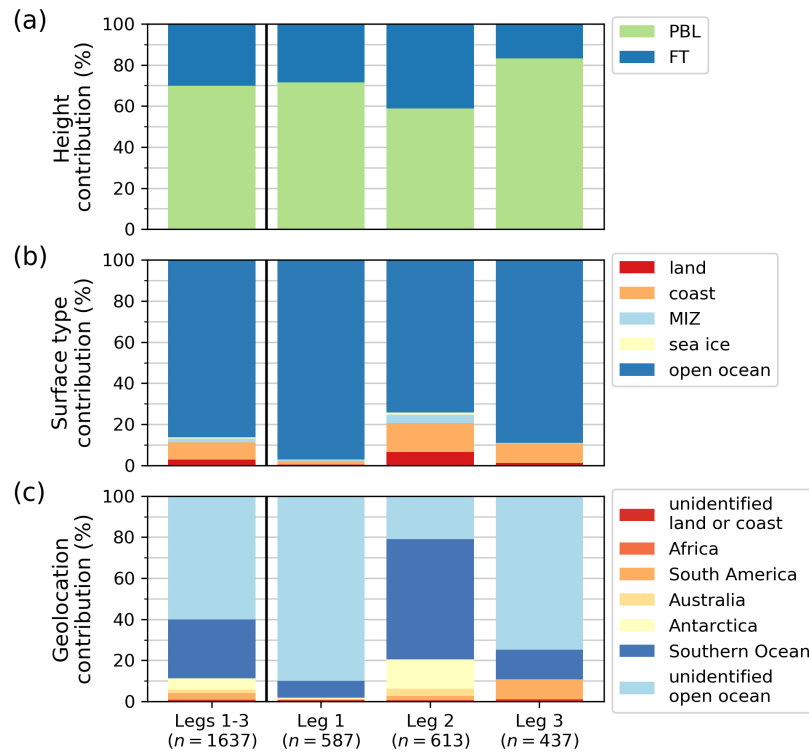
**Figure 4.9:** Mean values for the results of the air-mass origin in the backward-trajectories regarding signal origin in terms of (a) height, (b) type, and (c) geographical location for the whole cruise and its Legs. In (a), contributions of PBL (green) and FT signal (blue). In (b), surface contribution fractions of land (red), coast or island (orange), open ocean (dark blue), marginal ice zone (MIZ, light blue), and sea ice (yellow). In (c), location of the surface signal as unidentified (red), Africa (dark orange), South America (medium orange), Australia (light orange), Antarctica (yellow), Southern Ocean (dark blue), or unidentified open ocean (light blue). The number of samples ($n$) is given for reference.
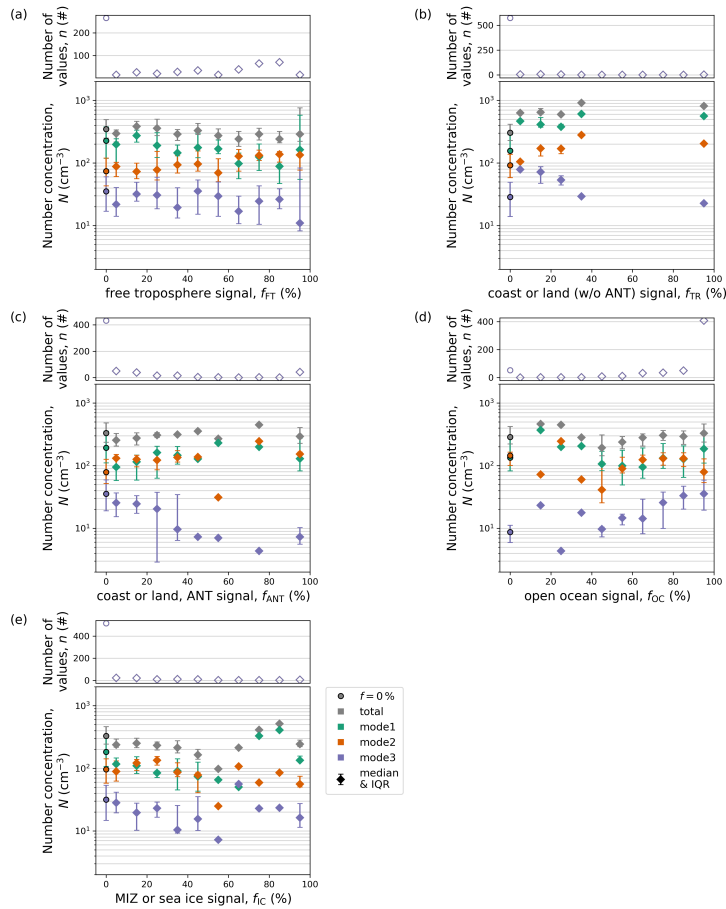
**Figure 4.10:** Median and respective IQR of total particle number concentration ($N_{\text{total}}$, black) and particle number concentration in the fitted Aitken (green), accumulation (orange) and SSA mode (purple) as function of (a) free tropospheric, (b) terrestrial, (c) Antarctica, (d) open ocean, and (f) sea ice signal in the analysis of the trajectories. In addition, the respective averaged $N$ for $f = 0$ and number of samples ($n$) is given for reference..
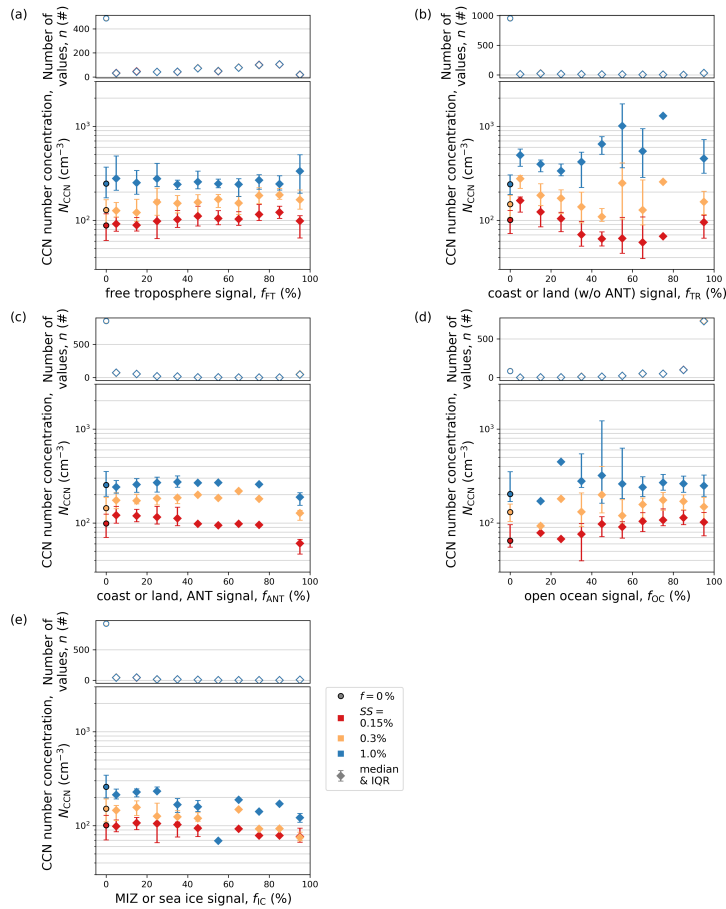
**Figure 4.11:** Median and respective ßglsiqr of CCN number concentration ($N_{\mathrm{CCN}}$) at a supersaturation of 0.15 % (red), 0.3 % (yellow), and 1 % (blue) as function of (a) free tropospheric signal $f_{\mathrm{FT}}$, (b) terrestrial signal $f_{\mathrm{TR}}$, (c) Antarctica signal $f_{\mathrm{AN}}$, (d) open ocean signal $f_{\mathrm{OC}}$ and (f) sea ice signal $f_{\mathrm{IC}}$. In addition, the respective averaged CCN number concentration for $f = 0$ and number of considered values for the averaging ($n$) for reference.
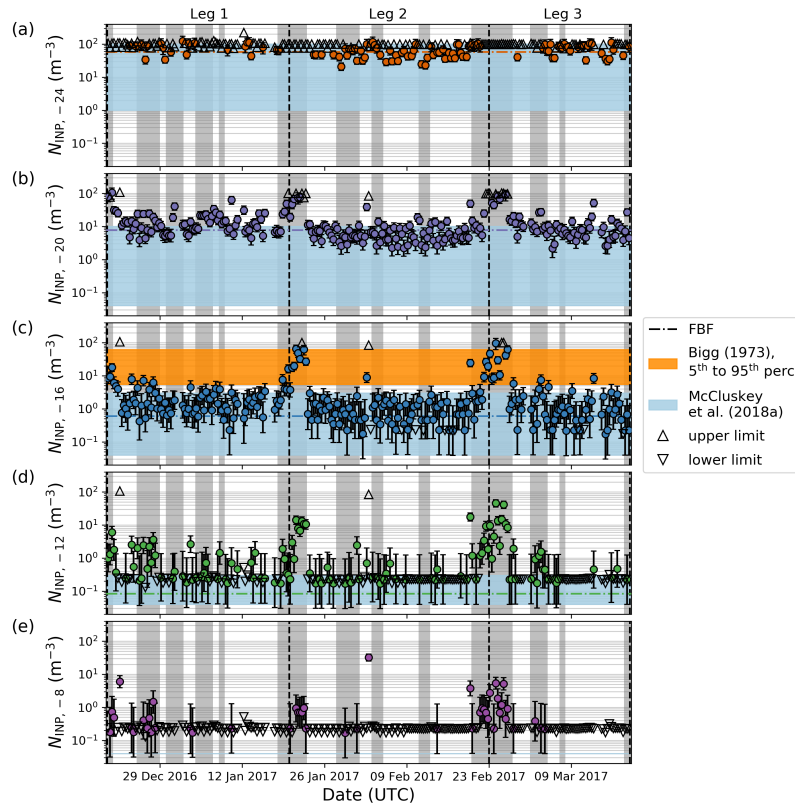
**Figure 4.12:** Time series of INP concentration (INP number concentration) at (a) $-24\,°\mathrm{C}$, (b) $-20\,°\mathrm{C}$, (c) $-16\,°\mathrm{C}$, (d) $-12\,°\mathrm{C}$, and (e) $-8\,°\mathrm{C}$ from filters sampled for $8\,\mathrm{h}$ each. Zero (infinite) values of INP number concentration at given temperature presented as values of lower (upper) edge of the detectable range, indicated by downward (upward) pointing triangles. Legs of ACE (dashed lines) and periods when the RV was close to land (grey area) are highlighted. For reference, the range of values from McCluskey et al. (2018a) and the $5^{\mathrm{th}}$ to $95^{\mathrm{th}}$ percentile of $N_{\mathrm{INP},-15}$ from Bigg (1973) is given.
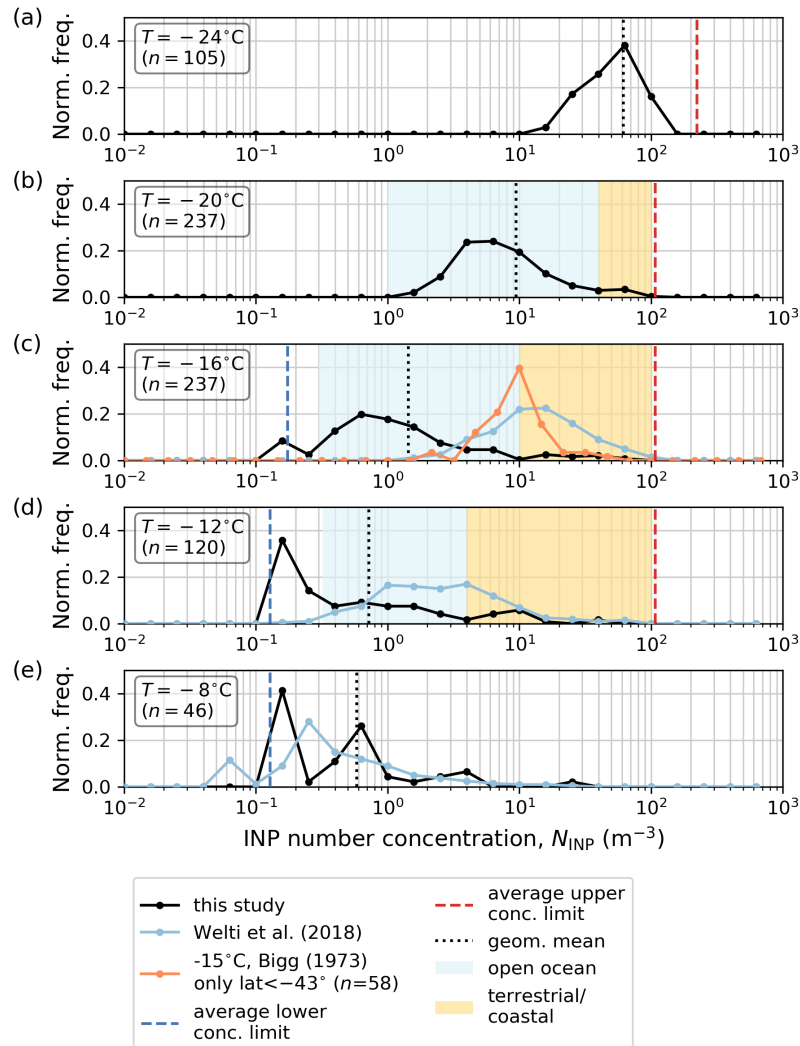
**Figure 4.13:** Normalised probability density functions (solid) and geometric mean values (dotted) for INP concentrations (INP number concentration) at (a) $-24\,°C$, (b) $-20\,°C$, (c) $-16\,°C$, (d) $-12\,°C$ and (e) $-8\,°C$ are given for filters sampled for 8 h (black). For reference, $N_{\mathrm{INP},-16}$, $N_{\mathrm{INP},-12}$, and $N_{\mathrm{INP},-8}$ for Cabo Verde (North Atlantic; Welti et al., 2018) are given in (c), (d), and (e), respectively (blue). Additionally, $N_{\mathrm{INP},-15}$ from Bigg (1973) for data points south of 43°S (orange) is given for comparison. A classification of modes by sampling location is given (yellow: coastal; light blue: open ocean) and averages of the upper (dark red) and lower concentration limit (dark blue) is indicated by dashed lines. The number of samples ($n$) is indicated in the figure.
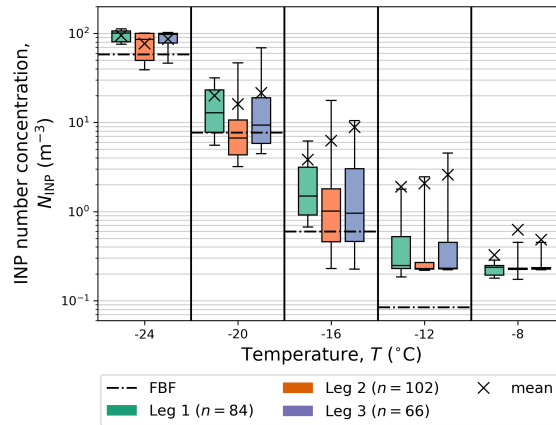
**Figure 4.14:** Box-and-whiskers plot indicating the median (horizontal lines), IQR (boxes), and $10^{th}$ to $90^{th}$ percentiles (whiskers) of INP number concentrations ($N_{INP}$) derived from filters sampled for 8 h during Leg 1 (green), Leg 2 (orange), and Leg 3 (purple). Mean values are given (crosses) for reference. Averaging was performed by treating zero (infinite) values of $N_{INP}$ at given temperature as values of the lower (upper) limit of the detectable range. The number of samples ($n$) is indicated in the figure.
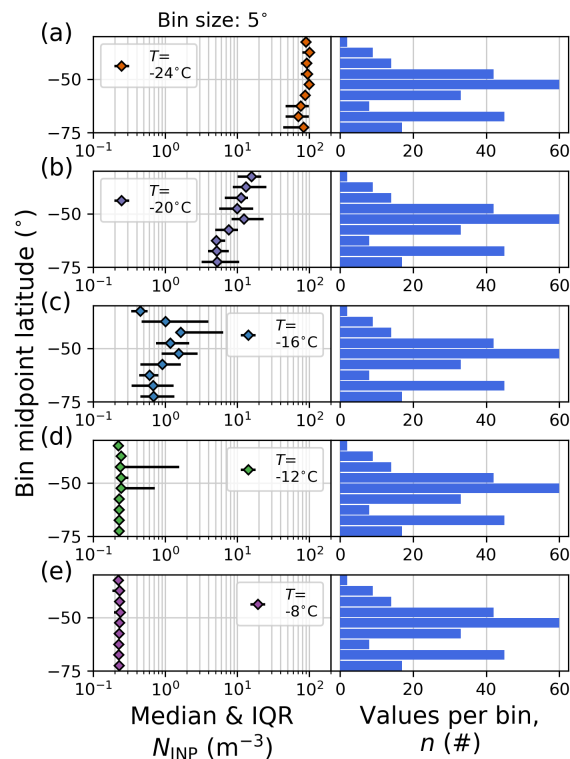


**Figure 4.15:** Median and respective IQR of INP number concentration at $T$ of (a) $-24\,°C$, (b) $-20\,°C$, (c) $-16\,°C$, (d) $-12\,°C$, and (e) $-8\,°C$ for Legs 1–3, binned by the latitude of the RV's position. The bins span the latitude from 40°S to 75°S, with a bin size of 5°. The number of values represented by each bin ($n$) is indicated in the figure.
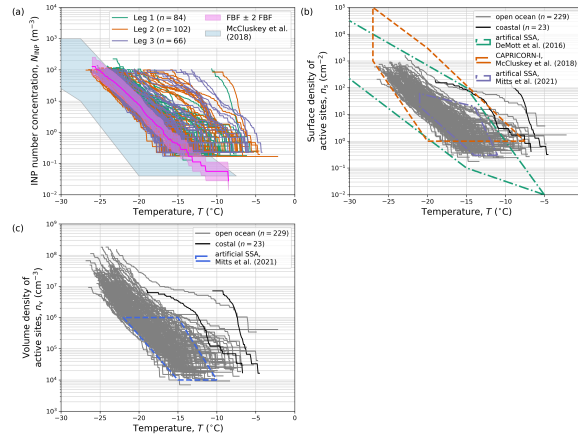
**Figure 4.16:** Temperature-dependence of (a) INP number concentration INP number concentration, (b) ice-active site density $n_\mathrm{s}$, and (c) ice-active volume density $n_\mathrm{v}$ for the LV filters sampled during ACE. Values of $n_\mathrm{s}$ ($n_\mathrm{v}$) were calculated by normalising INP number concentration with the total particle surface area (total particle volume) derived from an averaged particle number size distribution per filter under the assumption of a population of only spherical particles. In (a) the data set is divided into Leg 1 (green), Leg 2 (orange), and Leg 3 (purple). In (b) and (c) the data set is divided into open ocean (gray) and coastal (black) based on the threshold in $N_{\mathrm{INP},-16}$ of $10\,\mathrm{m}^{-3}$ (see Fig. 4.13c). In (a) the measurement background from averaged spectra of FBF $\pm$ a factor of two (pink line and area) and the data range from McCluskey et al. (2018a) is given for reference (light blue area). In (b) data ranges from DeMott et al. (2016) (green), McCluskey et al. (2018a) (orange) and Mitts et al. (2021) (purple) are given for reference. The range of values (dashed) from Mitts et al. (2021) is given in (c) for reference. The number of samples ($n$) are indicated in the figure.
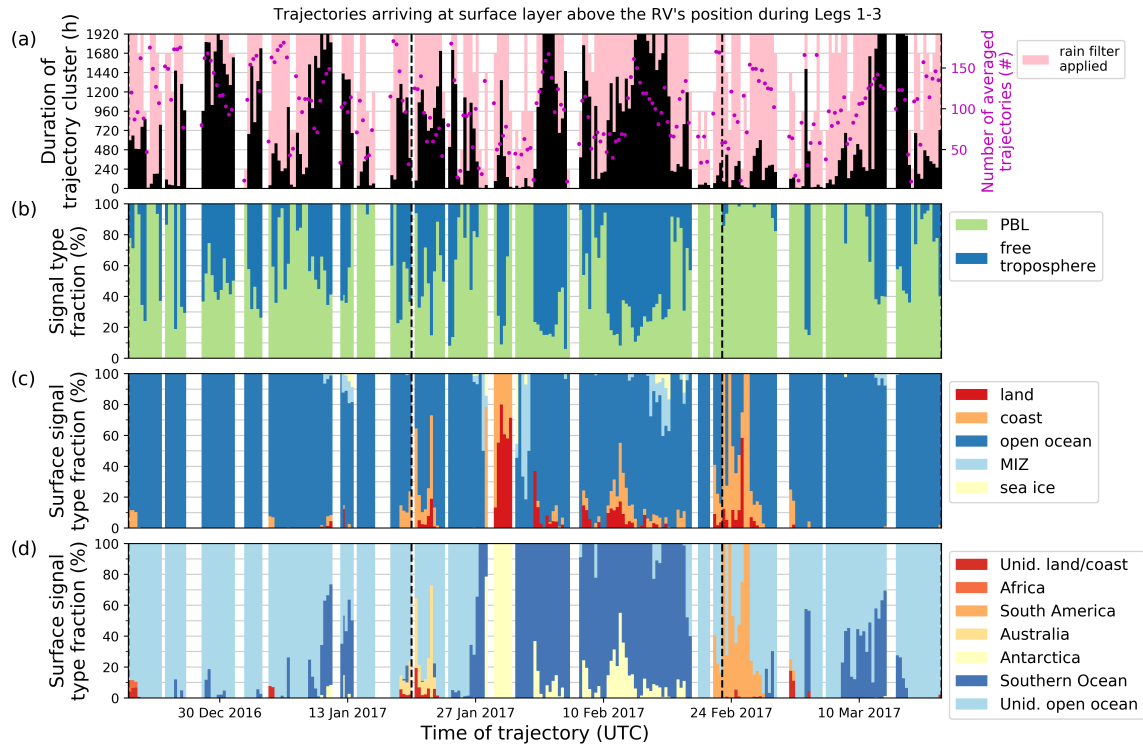
**Figure 4.17:** Results of the analysis of the 10-day backward-trajectories calculated for ACE regarding potential aerosol particle signals. The time of potential signal pick-up for each time steps averaged trajectory (black) and the part of the trajectory not considered due to the applied rain filter (pink) in (a). In addition, the total number of averaged trajectories per time step is given (magenta). The normalised contribution of PBL (green) and FT (blue) for each trajectory using the model's planetary boundary layer height in (b). Surface signal specification using the model's land-sea mask and sea ice fraction ($f_{SI}$) to into land (red), coast (orange), open ocean ($f_{SI} \leq 15\%$; dark blue), marginal ice zone ($15\% < f_{SI} < 80\%$; light blue), and sea ice ($f_{SI} > 80\%$; yellow) signal in (c). Information on the geographical position in (d) using the polygons for Africa, South America, Australia and Antarctica in Radenz et al. (2021). The 10-day backward-trajectories for ACE are available in Thurnherr et al. (2020).
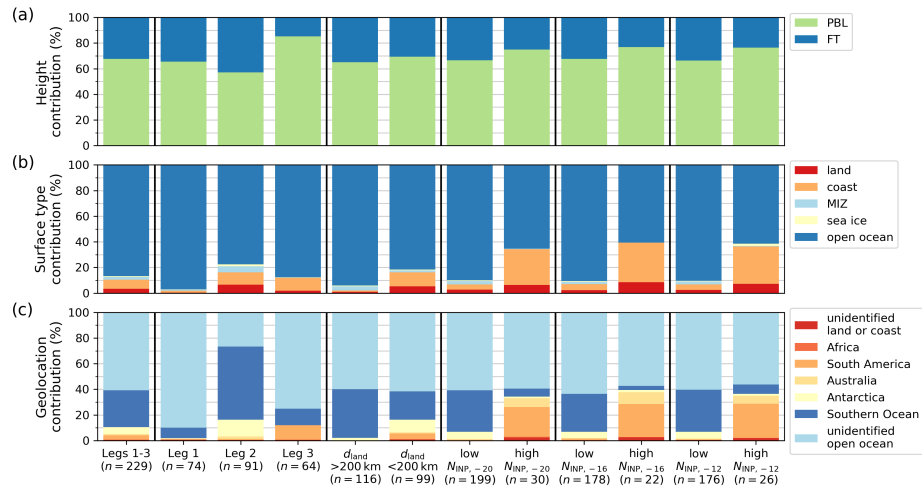
**Figure 4.18:** Percentage of (a) height level, (b) over-passed surface type, and (c) over-passed geographic location by 10-day backward-trajectories (see subsection 3.4.3). Colour codes for surface types are: non-Antarctic land masses (red), non-Antarctic coastal regions or islands (orange), Antarctic continent or coastal regions (AN; yellow), ice-covered regions (light blue), and open ocean (dark blue). From left to right, the different surface contributions to the air-masses are shown for the entire circumnavigation (Legs 1-3), separated by Leg (see Fig. 1.3), cases of $d_{\text{land}}$ above or below $200\,\text{km}$, and cases of $N_{\text{INP},-20}$ below ("low") or above $40\,\text{m}^{-3}$ ("high"), $N_{\text{INP},-16}$ below/above $10\,\text{m}^{-3}$, and $N_{\text{INP},-12}$ below/above $4\,\text{m}^{-3}$ analogous to ranges indicated in the respective PDF (see Fig. 4.13b–d). The number of samples ($n$) are indicated in the figure.
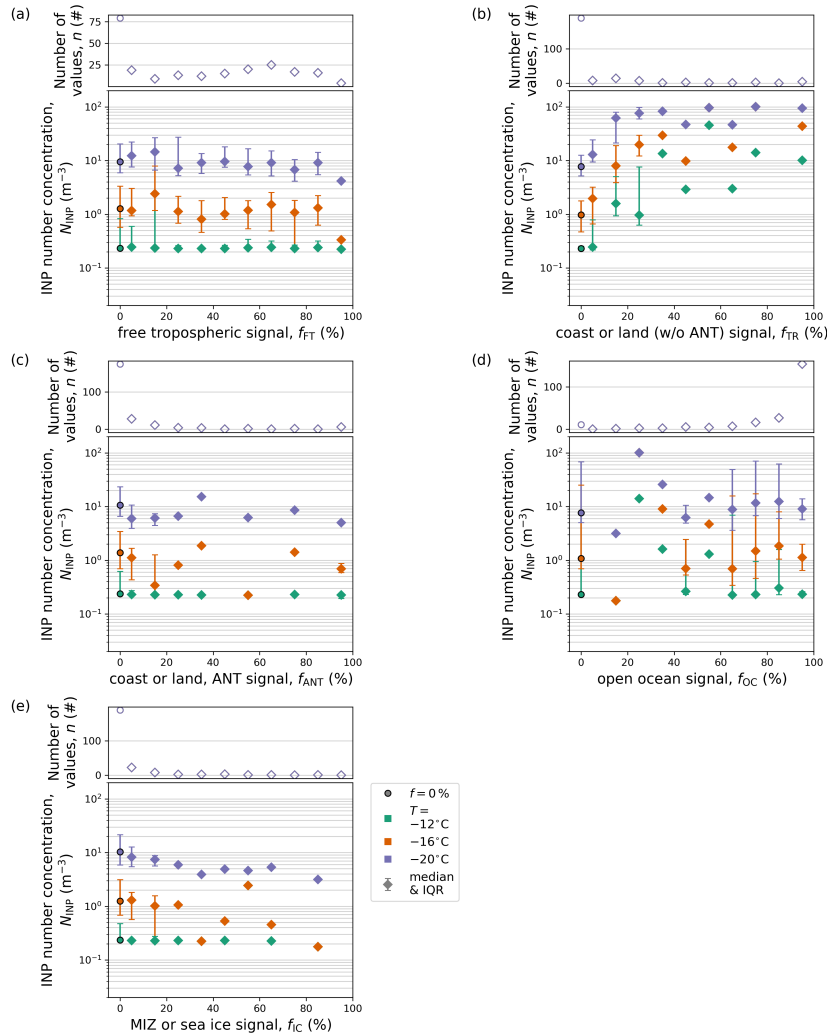
**Figure 4.19:** Median and respective IQR of INP number concentration ($N_{\text{INP}}$) at a $T$ of $-12\,°\text{C}$ (green), $-16\,°\text{C}$ (orange), and $-20\,°\text{C}$ (purple) as function of (a) free tropospheric signal $f_{\text{FT}}$, (b) terrestrial signal $f_{\text{TR}}$, (c) Antarctica signal $f_{\text{AN}}$, (d) open ocean signal $f_{\text{OC}}$ and (f) sea ice signal $f_{\text{IC}}$. In addition, the median value and respective IQR for INP number concentration at $f = 0$ (circle) and number of considered values for the averaging ($n$) for reference.

correlation analysis at 24h resolution
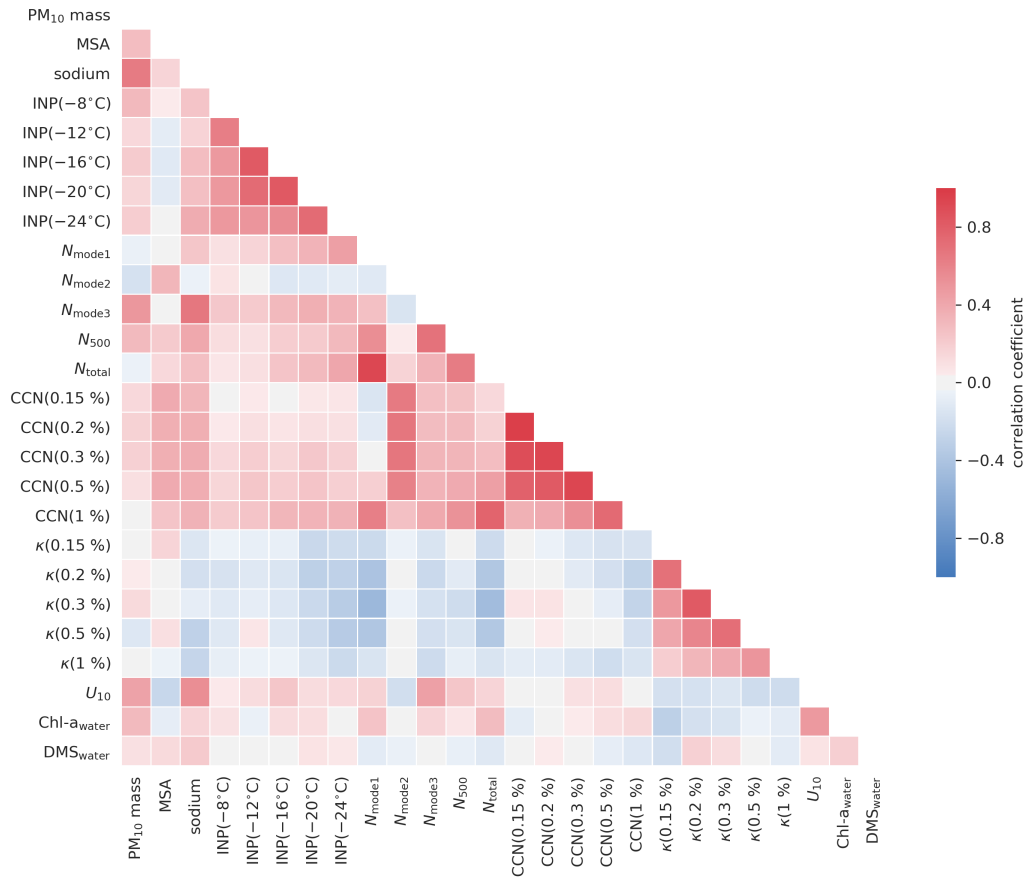


**Figure 4.20:** Spearman rank correlation matrix of quantities directly measured or derived from measurements during ACE. From the 24 h long HV sampling, $PM_{10}$ mass and mass concentrations of particulate sodium and MSA are included. INP number concentrations at temperatures of $-8\,°C$, $-12\,°C$, $-16\,°C$, $-20\,°C$ and $-24\,°C$ ($INP(T)$) are included from the LV filters, sampling for eight hours. Here, the estimates for INP number concentrations above and below the detection limit are included. From hourly smoothed PNSDs, the total particle number concentration ($N_{total}$), respective three modes ($N_{mode1}$, $N_{mode2}$, and $N_{mode3}$), and the number concentration of aerosol particles larger than $500\,nm$ ($N_{>500}$) are included. CCN number concentration at $0.15\,\%$, $0.2\,\%$, $0.3\,\%$, $0.5\,\%$ and $1\,\%$ supersaturation ($CCN(SS)$) and derived aerosol particle hygroscopicity parameter ($\kappa(SS)$) are included. Additionally, daily-averaged wind speed at $10\,m$ a. s. l. ($U_{10}$), and in-water concentrations of chlorophyll a (Chl $a_{water}$) and dimethyl sulphide ($DMS_{water}$) are used. Positive correlation between two quantities indicates a similar trend over time, while an opposing behaviour is indicated by a negative correlation coefficient.

# Chapter 5

# Summary and Conclusions

The Southern Ocean (SO) is a region of interest for the ongoing research of Earth's changing climate, as it was found to feature pristine aerosol conditions during the Austral summer months. Measurements of aerosol properties, which are supposed to be similar to those prevailing under pre-industrial conditions, are therefore extremely valuable, e.g. for atmospheric modelling. However, actual aerosol particle measurements over the SO have been sparse, both temporally and spatially. During the Austral summer of 2016/17, in situ measurements and off-line sampling of aerosol particles over the SO were conducted as part of the Antarctic Circum-navigation Expedition (ACE). In the framework of this doctoral thesis, I analysed the results of the aerosol particle measurements during ACE with a focus on abundance and properties of cloud-relevant aerosol particles, i.e. cloud condensation nuclei (CCN) and ice-nucleating particles (INP). In addition, colleagues provided information on the chemical composition of the sampled aerosol and I analysed the backward-trajectories available for ACE, to gain additional information on the origin of the sampled CCN and INP. With a number of quantities from these analyses I performed a correlation analysis to gain further hints on links between the different investigated parameters. Using all the presented findings, I answer the research questions, formulated in the introduction, in the following.

- What are typical CCN number concentrations in the Southern Ocean region?

In general, CCN number concentrations ($N_{\mathrm{CCN}}$) throughout the cruise spanned 2 orders of magnitude at a single level of supersaturation ($SS$), e.g. 3–590 cm$^{-3}$ at $SS = 0.3\,\%$ ($N_{\mathrm{CCN},0.3}$). Leg-wise averaging of $N_{\mathrm{CCN}}$ showed differences within the natural variability, hinting on an overall small longitudinal variability. In contrast, the investigation of the latitudinal dependence showed decreasing concentrations towards Antarctica, consistent with Humphries et al. (2021). Overall, CCN results compare well (<30 % percentage difference) with measurements of previous and quasi-simultaneous studies in the SO region. However, $N_{\mathrm{CCN},0.2}$ during ACE were almost a factor 2 higher than what a model run by Regayre et al. (2020) predicted and constraining the actual measurements helped to improve their model's performance.

- What is the CCN's hygroscopicity and how does it vary between the Southern Ocean's sectors?

The CCN hygroscopicity was investigated via calculation of the critical dry diameter ($D_{\mathrm{crit}}$) and subsequent derivation of the hygroscopicity parameter ($\kappa$). Encountered values of $\kappa$ were in the range between 0.2 and 0.9, corresponding to mixtures with variable amounts of organic and inorganic material. Compared to other studies, values during ACE are around a factor 2 lower than what was measured in the vicinity (e.g. on Antarctica) or modelled for the SO region. Average values of $\kappa$ were found to be independent of $SS$ and thus particle size, indicating (in first approximation) an internally mixed CCN population in the Aitken and accumulation mode. Probability density functions (PDF) of $\kappa$ were found to be mono-modal at $SS$ of 0.15 %, while for higher $SS$ tails towards smaller and larger $\kappa$ values were found, hinting at the presence of small Aitken mode particles mainly composed of material with low hygroscopicity.

- What are the sources of the Southern Ocean region's CCN?

The absence of a correlation between the sodium particle mass concentration (as sea salt tracer) and $N_{\mathrm{CCN}}$ points towards sea spray aerosol (SSA) not being an important source for CCN in the marine boundary layer (MBL) of the SO, agreeing well with the findings of Schmale et al. (2019). A secondary origin of the sampled CCN is thus likely and further underlined by the simultaneous occurrence of the highest $N_{\mathrm{CCN}}$ and a pronounced Aitken mode, which itself cannot stem from primary origin. When the research vessel (RV) was in the vicinity of land, generally higher $N_{\mathrm{CCN}}$ were encountered, pointing towards terrestrial and/or coastal influences on the CCN population. This is generally supported by the analysis of the air-mass origin but not in the case of Antarctica, as lower $N_{\mathrm{CCN}}$ were encountered close to the Antarctic coast. The importance of the free troposphere (FT) and/or long-range transport for the CCN origin is further underlined by the bi-modal nature of the particle population and the scarcity of new particle formation (NPF) events encountered in the SO's MBL. The FT played a role in the residence time of the air-mass ($\sim$30 %) on average), however to a far lesser extend than the planetary boundary layer (PBL) ($\sim$70 %). Here, the residence time in the PBL was dominated by an oceanic influence ($\sim$85 %). In consequence, a distinction between the effects of long-range transport and residency in the free tropospheric was not possible. However, with both PDF for $N_{\mathrm{CCN}}$ and $\kappa$ resembling mono-modal distributions, the sampling of aerosol particles originating from two distinctly different sources during ACE is out of the question.

- What are the INP number concentrations in the Southern Ocean region and how do they vary between the Southern Ocean's sectors?

Analysis of filter-collected atmospheric aerosol particles regarding ice activity yielded temperature-dependent INP number concentrations ($N_{\mathrm{INP}}$) in the range between $-4$ and $-27\,^\circ$C. Throughout the cruise, $N_{\mathrm{INP}}$ varied up to 3 orders of magnitude at a given temperature ($T$). Comparison with other studies showed that values for ACE are lower than what was observed previously over the SO, e.g. by Bigg (1973), while being on the upper end of what is reported in McCluskey et al. (2018a) for a specific sector of the SO. Consistent with other ship-based investigations in Welti et al. (2020), a pole-ward decrease in $N_{\mathrm{INP}}$ abundance was found. In contrast, leg-wise averages showed no longitudinal trend in the INP abundance.

- What are the sources of the Southern Ocean region's INP?

The temporal evolution of $N_{\mathrm{INP}}$ showed elevated values coinciding with the RV being in the proximity of land. This points towards terrestrial and/or coastal sources influencing the INP population and was confirmed by the analysis of the backward-trajectories, which showed air-masses having resided much long over land-masses or coastal areas for cases of elevated $N_{\mathrm{INP}}$. INP spectra for the most part of the cruise feature similar behaviour of $N_{\mathrm{INP}}$ over a wide temperature range. This is underlined by the results of the correlation analysis showing high correlations between $N_{\mathrm{INP}}$ in the temperature range between $-12$ and $-24\,^\circ$C. I interpret this as a mix of signals from long range-transported INP populations of biogenic ($T > -20\,^\circ$C) and mineral ($T < -20\,^\circ$C) origin. Indications for local INP sources are not apparent, e.g. no correlation between $N_{\mathrm{INP}}$ and in-water chlorophyll a content (Chl $a$; as marine biological activity proxy) was found.

The presented data set is a unique, circum-Antarctic view on CCN and INP abundance, their properties and indications towards aerosol particle origin. It gives valuable insights on the conditions over the SO regarding cloud-relevant aerosol particles, compare well with previous studies (Welti et al., 2020) and adds to the to-date sparse number of studies of the SO region. Further, it found use in multi-disciplinary (Landwehr et al., 2021), climate modelling (Regayre et al., 2020), and remote sensing applications (Efraim et al., 2020).

# Chapter 6

# Outlook

This study is a substantial contribution to the to-date sparse number of cloud-relevant aerosol particle (i.e. CCN and INP) measurements over the SO region. I presented first clues on the summertime abundance and origin of CCN and INP in the SO's MBL.

In terms of seasonal coverage, ACE was limited to the Austral summer. Long-term measurements would enable characterisation of the annual cycle in CCN and INP abundance and origin. Potential sites could be any coastal or quasi-coastal location on the SO with sufficient infrastructure to support long-term operations. A recent example for the Leibniz-Institute for Tropospheric Research (TROPOS) establishing CCN measurements at *Neumayer III* station on Antarctica's Queen Maud Land. Another example are CCN measurements at Cerror Mirador (Punta Arenas, Chile) that were started by TROPOS with the help of the local university in 2019. Studies have shown that for station-based measurements, such as Australia's coastal Cape Grim station or Antarctica's *Princess Elisabeth* station, a verifiable terrestrial influence on the sampled aerosol population can occur. However, data filtering is possible and thus a viable option for other measurement sites. Given the non-stationary nature of a ship-based expedition, the aerosol particle source appointment for ACE could only be done with a specifically developed air-mass origin identification scheme. For a stationary measurement site, extended source appointment would be possible, e.g. dispersion modelling similar to what is done in Herenz et al. (2018, 2019). Regarding the vertical distribution of aerosol particles, measurements during ACE were limited to the MBL. With the importance of residence in the FT and long-range transport processes for the particle population over the SO underlined in this thesis, it can be concluded that vertical measurements are needed. Currently, both moving (e.g. aircraft-based) and quasi-stationary (e.g. tethered balloon) profiling platforms are available or in development, benefiting from the ongoing miniaturisation of CCN and INP instrumentation.

Regarding the CCN measurements in the SO's MBL, the exclusion of $SS = 0.1\,\%$ due to data quality issues hindered the characterisation of CCN in the accumulation mode.

For both low-volume (LV) and high-volume (HV) filter sampling during ACE, a substantial number of INP number concentrations were close to or at the edge of the detectable range. Future studies on INP over the SO need to better constrain their sampling strategy (e.g. filter material or sampling volume) with concentrations presented in this thesis as a point of reference. Especially in the regime of biological INP (above $-20\,°C$), $N_{\mathrm{INP}}$ were mostly outside the detectable range. Further, the contribution of biological INP could be quantified by applying a thermal treatment to the filters, similar to what is done in McCluskey et al. (2018a). This enables the assessment of heat labile material to the INP population. As for the second potential source of INP in the SO's MBL, the contribution of mineral INP (below $-20\,°C$) could be quantified via tracer measurements, e.g. ambient radon concentrations as what is done in McCluskey et al. (2018a).

# Appendix A

# Analyses of chemical composition

As a first step of the analysis, filters were acclimated for a duration of $72\,h$ at a temperature of $20\,°C$ and $50\,\%$ relative humidity. Secondly, the mass of the sampled material ($PM_{10}$) was determined by weighing each filter with a micro-balance (*AT261 Delta Range*, Mettler Toledo, Greifensee, Switzerland). Thirdly, extraction of sampled material of each filter with $25\,ml$ milliQ water and $15\,min$ in shaker, $15\,min$ in ultrasonic bath and another $15\,min$ in shaker. The extract was cleaned by pushing it through a $0.45\,µl$ pre-cleaned one-way syringe filter, to remove insoluble materials.

## A.1   Organic cabon and elemental carbon

The organic content (OC) and elemental carbon (EC) content of each filter were measured on a $1.5\,cm^2$ cut-out, using a dual-optical carbonaceous analyser (Sunset Laboratory Inc., Tigard, OR, USA). The EUSAAR's (European Supersites for Atmospheric Aerosol Research) temperature protocol "EUSAAR 2" was utilised and a charring correction was applied (Cavalli et al., 2010). The correction value for pyrolytic carbon was determined using a laser with a wavelength of $678\,nm$. Under a helium atmosphere, each sample was extracted from the filter medium via heat. This was follow by exposure to an oxidising atmosphere (mixture of oxygen and helium) and application of carefully controlled heat ramps. A flame ionisation detector was use to quantify the methane that formed during the catalytic methanation of carbon dioxide ($CO_2$).

## A.2   Water-soluble organic carbon

Each filter's content of water-soluble organic carbon (WSOC) was obtained by analysing the filtered aqueous particle extract with a total organic carbon (TOC) analyzer (*TOC-VCPH*, Shimadzu Corp., Kyoto, Japan). The inorganic carbonates within the sample were converted to $CO_2$ by adding a $1.5\,\%$ hydrochloric acid solution ($2\,M$) to the aqueous extract. The result is an acidified sample (pH of 2). By channelling synthetic, particle-free air through the acidified sample, forming $CO_2$ was captured. Furthermore, carbon within the sample was oxidised by adding $300\,µl$ of the solution to a catalyst (aluminum oxide/platinum on quartz wool) under thermal-controlled conditions at $720\,°C$. The formed $CO_2$ was analysed by non-dispersive infrared detection. For quantification, external calibration was performed with the help of potassium hydrogen phthalate.

## A.3   Inorganic ions

Concentrations of inorganic ions (sodium, chloride, sulfate, nitrate, ammonium, potassium, magnesium, and calcium) from the filtered aqueous extract via an ion chromatograph system (*ICS-3000*, Dionex Corp., Sunnyvale, CA, USA), equipped with a guard column ($3 \times 50\,mm$; *IonPac CG16*,

Dionex Corp.) and a separatory column ($3 \times 250$ mm; *IonPac CS16*, Dionex Corp.).  At a constant temperature of 60 °C.  Separation of the ions was achieved by a gradient of methanesulfonic acid (MSA). At the start, the MSA mass concentration was 6 mM, increased to 15 mM (20 min), 30 mM (30 min), and 50 mM (31 min) until the end of the analysis run (42 min).

## A.4   Methylsulfonic acid

The MSA content of each filter was determined using capillary electrophoresis with ultra violet detection (*Spectra Phoresis 1000*, Thermo Fisher Scientific inc., Waltham, MA, USA) on the filtered aqueous particle extract.

# Appendix B

# Additional Data Representations
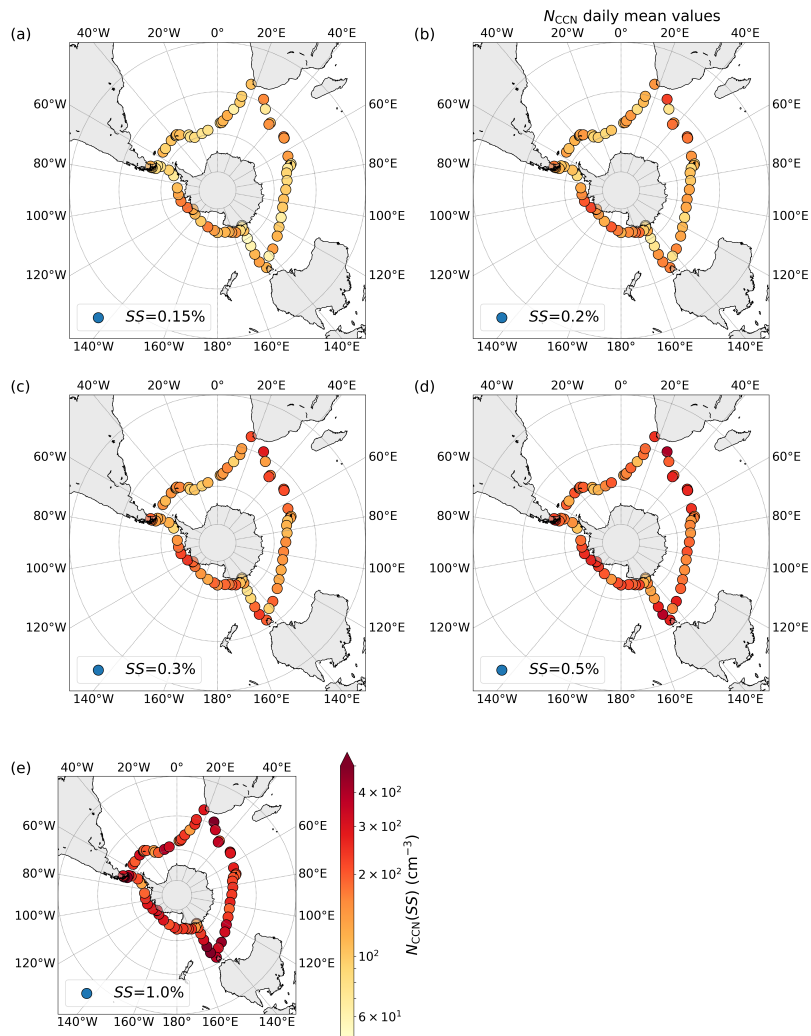
**Figure B.1:** Geographical distribution of daily averaged CCN number concentration at $SS$ of (a) 0.15 %, (b) 0.2 %, (c) 0.3 %, (d) 0.5 %, and (e) 1 % are given as the midpoint of the respective cruise track of that day (circles).

**Table B.1:** Overview of the CCN number concentrations ($N_{\mathrm{CCN}}$) and critical dry diameters ($D_{\mathrm{crit}}$) at a given level of supersaturation ($SS$) throughout and for parts of the cruise, given as geometric mean (gmean) value (and a factor of respective one geometric standard deviation (gSD)). Additionally, the averages of the total particle number concentration ($N_{\mathrm{total}}$) and the hygroscopicity parameter ($\kappa$) at given $SS$ presented as median values and respective inter-quartile range (IQR).

| | Legs 1–3 | Leg 1 | Leg 2 | Leg 3 |
|---|---|---|---|---|
| $N_{\mathrm{total}}$ (cm$^{-3}$) | 305.04 (225.77, 451.84) | 389.75 (272.06, 539.29) | 277.00 (211.34, 382.17) | 318.76 (235.02, 442.93) |
| $N_{\mathrm{CCN}}(SS)$ (cm$^{-3}$) | | | | |
| $SS = 0.15\,\%$ | 88.64 (53.28, 147.48) | 90.49 (52.04, 157.33) | 94.20 (59.19, 149.92) | 78.61 (47.29, 130.69) |
| $0.2\,\%$ | 111.79 (67.98, 183.82) | 113.56 (67.28, 191.67) | 119.48 (76.03, 187.76) | 98.63 (58.85, 165.29) |
| $0.3\,\%$ | 132.52 (79.41, 221.16) | 133.83 (80.84, 221.54) | 143.39 (88.97, 231.11) | 115.50 (66.95, 199.27) |
| $0.5\,\%$ | 171.69 (101.49, 290.47) | 172.18 (106.83, 277.51) | 185.44 (111.84, 307.47) | 150.71 (84.43, 269.05) |
| $1\,\%$ | 247.98 (145.28, 423.28) | 241.12 (157.20, 369.82) | 257.79 (146.73, 452.92) | 239.56 (133.96, 428.39) |
| $D_{\mathrm{crit}}(SS)$ (nm) | | | | |
| $SS = 0.15\,\%$ | 109.40 (100.29, 119.34) | 112.56 (101.94, 124.29) | 108.61 (99.91, 118.07) | 110.05 (100.98, 119.94) |
| $0.2\,\%$ | 84.07 (72.77, 97.12) | 89.86 (75.98, 106.28) | 81.78 (71.46, 93.59) | 86.52 (75.97, 98.54) |
| $0.3\,\%$ | 66.23 (56.37, 77.83) | 72.77 (60.36, 87.72) | 64.15 (55.43, 74.24) | 66.73 (57.51, 77.42) |
| $0.5\,\%$ | 47.04 (39.98, 55.34) | 52.23 (42.01, 63.42) | 45.58 (39.42, 52.69) | 47.18 (40.84, 54.52) |
| $1\,\%$ | 30.22 (25.73, 35.48) | 32.90 (27.73, 39.04) | 29.46 (25.20, 34.44) | 30.22 (26.18, 34.88) |
| $\kappa(SS)$ | | | | |
| $SS = 0.15\,\%$ | 0.50 (0.40, 0.60) | 0.42 (0.33, 0.53) | 0.51 (0.42, 0.61) | 0.48 (0.40, 0.59) |
| $0.2\,\%$ | 0.61 (0.44, 0.82) | 0.43 (0.30, 0.66) | 0.67 (0.50, 0.89) | 0.54 (0.42, 0.72) |
| $0.3\,\%$ | 0.57 (0.39, 0.78) | 0.36 (0.24, 0.60) | 0.63 (0.46, 0.84) | 0.55 (0.41, 0.73) |
| $0.5\,\%$ | 0.55 (0.39, 0.79) | 0.34 (0.23, 0.58) | 0.60 (0.45, 0.84) | 0.54 (0.40, 0.74) |
| $1\,\%$ | 0.52 (0.38, 0.70) | 0.39 (0.24, 0.54) | 0.55 (0.42, 0.76) | 0.52 (0.38, 0.68) |

**Table B.2:** Overview of the LV sampling INP number concentration ($N_{\mathrm{INP,LV}}$) encountered throughout and during parts of the cruise, given as mean, median and gmean (and a factor of respective one gSD) values. The number of samples is indicated ($n$). Additionally, averaging was performed with the inclusion of values on the detectable range and values are given under $N_{\mathrm{INP}}{}^{*}$.

| | mean | median | gmean (gSD) | $n$ |
|---|---|---|---|---|
| $N_{\mathrm{INP,LV}}(T)$ (m$^{-3}$) | | | | |
| $T = -24\,°\mathrm{C}$ | 66.95 | 64.78 | 61.45 (40.07, 94.25) | 105 |
| $-20\,°\mathrm{C}$ | 13.87 | 8.57 | 9.43 (4.21, 21.15) | 237 |
| $-16\,°\mathrm{C}$ | 4.41 | 1.18 | 1.44 (0.41, 5.10) | 237 |
| $-12\,°\mathrm{C}$ | 2.66 | 0.42 | 0.72 (0.17, 2.99) | 120 |
| $-8\,°\mathrm{C}$ | 1.67 | 0.46 | 0.58 (0.18, 1.84) | 46 |
| $N_{\mathrm{INP,LV}}^{\star}(T)$ (m$^{-3}$) | | | | |
| $T = -24\,°\mathrm{C}$ | 85.22 | 97.65 | 80.39 (55.48, 116.48) | 252 |
| $-20\,°\mathrm{C}$ | 18.75 | 8.84 | 10.82 (4.16, 28.15) | 252 |
| $-16\,°\mathrm{C}$ | 6.11 | 1.17 | 1.46 (0.35, 5.97) | 252 |
| $-12\,°\mathrm{C}$ | 2.15 | 0.23 | 0.41 (0.12, 1.43) | 252 |
| $-8\,°\mathrm{C}$ | 0.49 | 0.23 | 0.27 (0.14, 0.50) | 252 |

**Table B.3:** Mean INP number concentrations of LV sampling ($N_{\mathrm{INP,LV,FBF}}$) and HV sampling field blank filter (FBF) ($N_{\mathrm{INP,HV,FBF}}$) at selected temperature ($T$).

| $T$ | $N_{\mathrm{INP,LV,FBF}}$ (m$^{-3}$) | $N_{\mathrm{INP,HV,FBF}}$ (m$^{-3}$) |
|---|---|---|
| $-24\,°\mathrm{C}$ | 57.76 | 105.11 |
| $-20\,°\mathrm{C}$ | 7.72 | 21.08 |
| $-16\,°\mathrm{C}$ | 0.59 | 5.64 |
| $-12\,°\mathrm{C}$ | 0.08 | 1.32 |
| $-8\,°\mathrm{C}$ | - | 0.86 |
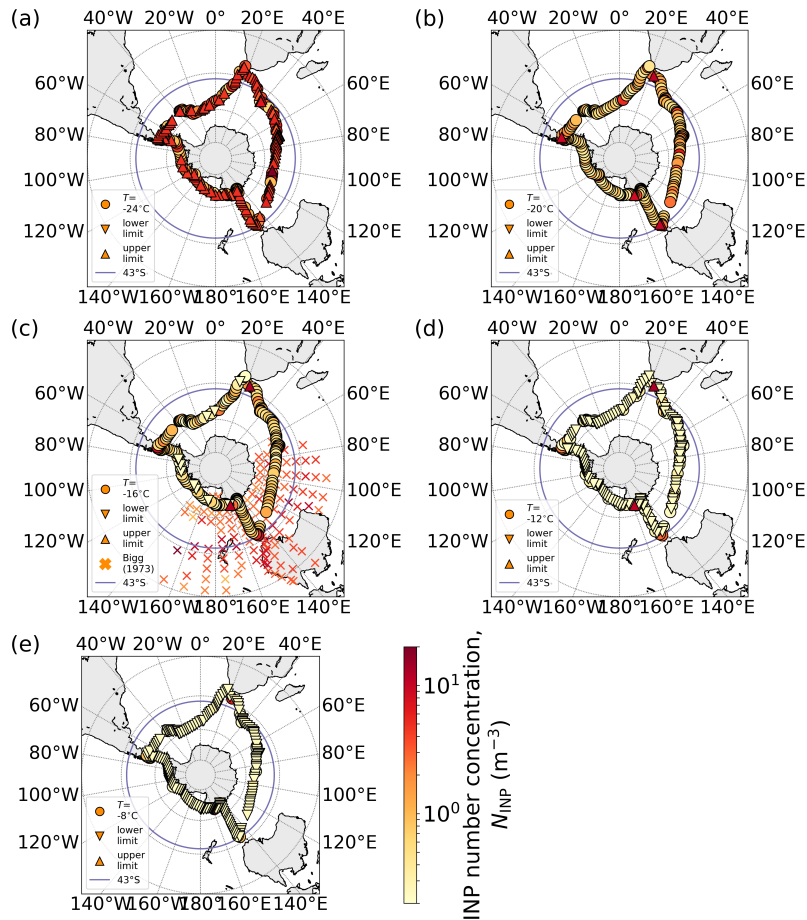
**Figure B.2:** Geographical distribution of measured INP number concentration at $T$ of (a) $-24\,°\text{C}$, (b) $-20\,°\text{C}$, (c) $-16\,°\text{C}$, (d) $-12\,°\text{C}$, and (e) $-8\,°\text{C}$ are given for filters sampled for $8\,\text{h}$ (circles). Estimates for INP number concentration values below (downward pointing triangle) and above the detectable range (upward pointing triangle) are indicated. For reference, $N_{\text{INP},-15}$ from Bigg (1973) for data points south of 43°S (purple) are given for comparison in (c).

**Table B.4:** Results for the analysis regarding the chemical composition of the HV filters sampled during ACE, presented as median values and respective IQR for particle mass concentration of OC, EC, WSOC, ammonium ($NH_4^+$), potassium ($K^+$), sodium ($Na^+$), magnesium ($Mg^{2+}$), calcium ($Ca^{2+}$), MSA, chloride ($Cl^-$), bromide ($Br^-$), nitrate ($NO_3^-$), sulphate ($SO_4^{2-}$), non-sea salt sulphate (nss-$SO_4^{2-}$), and oxalate ($C_2O_4^{2-}$). Averages for the whole cruise, parts of it and 4 days with low EC and WSOC concentrations (golden days, see section 4.3). Additionally, the ratio $r$ of chloride to sodium and MSA to non-sea salt sulphate. Note, if number of samples is below three, IQR is omitted.

| | | Legs 1-3 | Leg 1 | Leg 2 | Leg 3 | Golden Days |
|---|---|---|---|---|---|---|
| $M$ ($\mu g\,m^{-3}$) | $PM_{10}$ | 32.350 (26.050, 49.600) | 42.400 (27.300, 52.600) | 31.050 (23.475, 47.475) | 33.300 (26.200, 50.700) | 28.350 (21.490, 33.850) |
| | OC | 7.460 (2.848, 17.318) | 4.201 (1.892, 15.608) | 10.672 (5.980, 17.318) | 3.660 (2.418, 17.043) | 0.166 (0.121, 0.329) |
| | EC | 1.111 (0.362, 2.388) | 1.215 (0.089, 2.339) | 1.404 (0.608, 2.336) | 0.559 (0.340, 2.272) | 0.0 |
| | WSOC | 0.578 (0.326, 1.163) | 0.418 (0.242, 1.109) | 0.804 (0.42, 1.096) | 0.503 (0.344, 1.115) | 0.035 (0.0, 0.104) |
| | $NH_4^+$ | 0.129 (0.077, 0.229) | 0.120 (0.087, 0.218) | 0.175 (0.128, 0.272) | 0.093 (0.060, 0.147) | 0.021 (0.012, 0.030) |
| | $K^+$ | 0.075 (0.049, 0.118) | 0.112 (0.074, 0.140) | 0.053 (0.026, 0.093) | 0.066 (0.054, 0.108) | 0.069 (0.066, 0.114) |
| | $Na^+$ | 2.750 (1.810, 3.885) | 3.550 (2.563, 4.918) | 1.810 (0.973, 3.151) | 2.745 (2.240, 4.095) | 3.870 (3.465, 4.640) |
| | $Mg^{2+}$ | 0.302 (0.216, 0.424) | 0.360 (0.272, 0.492) | 0.219 (0.113, 0.323) | 0.327 (0.250, 0.381) | 0.354 (0.346, 0.443) |
| | $Ca^{2+}$ | 0.304 (0.210, 0.429) | 0.344 (0.226, 0.503) | 0.256 (0.189, 0.412) | 0.296 (0.201, 0.408) | 0.280 (0.245, 0.302) |
| | MSA | 0.102 (0.074, 0.143) | 0.114 (0.080, 0.182) | 0.112 (0.074, 0.207) | 0.086 (0.061, 0.101) | 0.047 (0.031, 0.062) |
| | $Cl^-$ | 4.590 (2.950, 6.325) | 6.020 (4.005, 8.248) | 2.980 (1.640, 5.305) | 4.595 (3.488, 6.815) | 5.570 (5.400, 7.465) |
| | $Br^-$ | 0.014 (0.010, 0.026) | 0.016 (0.011, 0.024) | 0.010 (0.007, 0.017) | 0.015 (0.012, 0.020) | 0.030 (0.023, 0.030) |
| | $NO_3^-$ | 0.040 (0.027, 0.083) | 0.038 (0.030, 0.067) | 0.041 (0.024, 0.067) | 0.060 (0.013, 0.183) | 0.028 |
| | $SO_4^{2-}$ | 1.260 (0.843, 1.655) | 1.540 (1.018, 2.050) | 1.260 (0.664, 1.655) | 0.951 (0.824, 1.338) | 0.957 (0.935, 1.164) |
| | nss-$SO_4^{2-}$ | 0.460 (0.233, 0.758) | 0.454 (0.323, 0.854) | 0.593 (0.423, 0.882) | 0.199 (0.141, 0.438) | 0.007 (0.003, 0.074) |
| | $C_2O_4^{2-}$ | 0.014 (0.009, 0.026) | 0.016 (0.010, 0.027) | 0.014 (0.010, 0.026) | 0.006 (0.003, 0.008) | 0.025 |
| $r$ ($kg\,kg^{-1}$) | $Cl^-$/$Na^+$ | 1.669 (1.590, 1.704) | 1.671 (1.602, 1.695) | 1.623 (1.558, 1.701) | 1.693 (1.618, 1.714) | 1.709 (1.574, 1.720) |
| | MSA/nss-$SO_4^{2-}$ | 0.269 (0.144, 0.416) | 0.271 (0.152, 0.345) | 0.194 (0.145, 0.300) | 0.489 (0.172, 0.793) | - |

# Appendix C

# Sensitivity Tests

## C.1   Omitting Monte Carlo simulations for $D_{\text{crit}}$ and $\kappa$

PDF of $\kappa$ are presented in Fig. C.1. Contrary to what is presented in subsection 4.1.3 (Fig. 4.7b), Fig. C.1a features $\kappa$ values that result from Eq. 2.3 and without MCS being performed as described in section 3.2.2. For Fig. C.1b, MCS results are considered, however values are not excluded outside the $10^{\text{th}}$ to $90^{\text{th}}$ percentile range for $D_{\text{crit}}$ as described in section 3.2.2.

The PDF for $\kappa$ in Fig. C.1a bear strong resemblance to the respective PDF for the MCS (Fig. 4.7b), underlining that the measurement uncertainty modelled with the help of MCS has a weak influence on the resulting $\kappa$ values. In contrast, the PDF for $\kappa$ in Fig. C.1b shows wider distributions and compared to Fig. 4.7b. Consequently, I conclude that the exclusion of extreme $D_{\text{crit}}$ values (and thus $\kappa$) improves the characterisation of typical $\kappa$ values presented in subsection 4.1.3.

## C.2   Higher resolution LV sampling

LV sampling was performed for extended periods during the cruise with each filter being sampled for 2 h (see subsection 3.3.2). INP spectra for these four periods during Leg 1 and Leg 3 are given in Fig. C.2. For each period, sampled 2 h filters lie within the curve given by the respective FBF and a factor of 2 (pink). Consequently, the sampling time of 2 h was not sufficient to resolve the overall low INP number concentration of the SO and no further conclusions on the diurnal variation in INP abundance can be drawn.

## C.3   Comparison to HV sampling INP Results

Additional INP spectra determined from HV samples (*DHA-80* sampler, see section 3.3) are given in Fig. C.3. Compared to the LV results in Fig. 4.20, the determined $N_{\text{INP}}(T)$ are higher and in a narrower range. LV and HV sampling differed in sample collection interval and filter material (LV: poly-carbonate pore filter, 0.2 µm pore size, 47 mm in diameter; HV: quartz fibre, 150 mm). Concerning collection intervals, continuous sampling over eight hour intervals were chosen for the LV filters to resolve diurnal INP number concentration variations. HV filters were collected during intervals of 24 h, interrupted by breaks due to the automatic shutdown to avoid contamination from ship exhaust. However, this was accounted for during data analysis (see section 3.3). Possible low biases of INP number concentration for higher sampled volumes have been discussed in Bigg et al. (1963) and Mossop and Thorndike (1966), but do not reflect the trend found for our two sampling techniques. The longer sampling interval of the HV filters could play a role here, with increased chances of sampling a singular, highly ice-active particle that creates a signal that can be interpreted as a generally higher abundance of INP. Analogous, the effect of bias towards singular events can
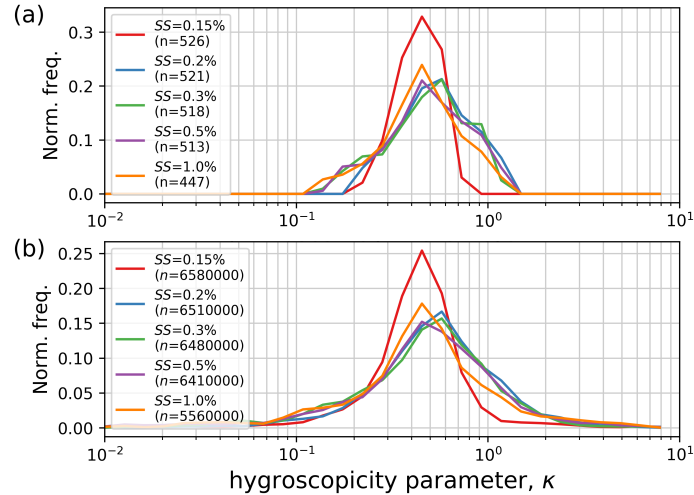
**Figure C.1:** Normalised probability density function of hygroscopicity parameter for $SS$ of 0.15 %, 0.2 %, 0.3 %, 0.5 % and 1 % (colour-coded) for Legs 1–3 without (a) performing Monte Carlo simulation (MCS) to assess the measurement uncertainty and (b) without the exclusion of $\kappa$ values that resulted from $D_{\mathrm{crit}}$ outside of $10^{\mathrm{th}}$ to $90^{\mathrm{th}}$ percentile range (per $SS$). The number of data points is indicated ($n$).

be found for the LV sampling's Leg-wise averages in Fig. 4.14, giving differences between mean and median values of up to 1 order of magnitude that underline the inclusion of strong outliers. In this case, the outliers are shown to stem from the elevated concentrations encountered when the RV was close to land (see Fig. 4.12c) and lead to higher mean values. Mean values are not representative for the majority of concentrations encountered on the open ocean. With our method, however, it is not possible to identify the sampled particle that initiated droplet freezing, as it is based on activation statistics. The difference in filter material could be another factor, but our results are in contrast to Wex et al. (2020) finding good agreement between quartz fibre and poly-carbonate filters for identical sampling intervals. Contamination from ship exhaust should not effect INP analysis results (see Appendix C in Welti et al., 2020) as exhaust particles are not ice-active in the investigated temperature range. For completeness, INP number concentration for HV sampling are given in Fig. C.3. Due to a higher data coverage (LV: $n_{\mathrm{filter}} = 253$; HV: $n_{\mathrm{filter}} = 79$) allowing for more robust statistics, I decided to focus on LV samples for the in-depth analysis presented in the framework of the thesis.

## C.4   Correlation analysis at finer temporal resolution

Averaging over 24 h was performed for the in situ measured quantities, in order to be included in the correlation analysis in section 4.4. A closer look at a finer temporal resolution is performed in the following, only using quantities that are available at a hourly resolution or respective hourly averages if necessary.

Results of this version of the correlation analysis are presented in Fig. C.4 and $\rho$ values are generally smaller when compared to the 24 h resolution correlation analysis in Fig. 4.20. The only exception being hygroscopicity parameter at $SS < 1\%$, where generally lower $\rho$ are found. This suggests that the averaging of hygroscopicity parameter to the 24 h resolution artificially creates correlations where there are none and consequently correlations of hygroscopicity parameter at 24 h resolution need to be treated carefully.
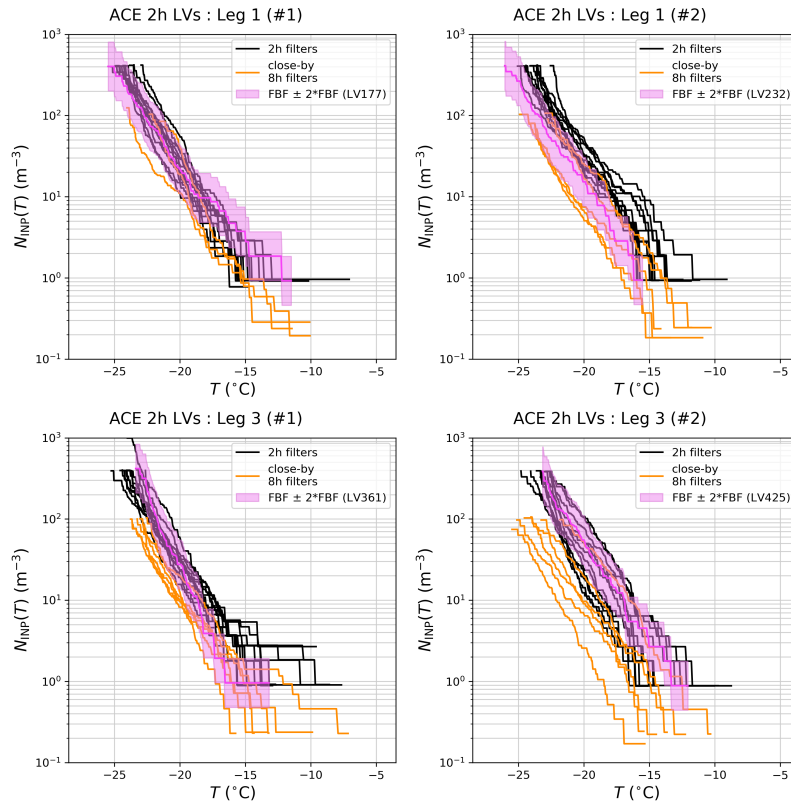
**Figure C.2:** $N_{\mathrm{INP}}$ as function of $T$ for LV filters sampled during Leg 1's (a) first and (b) second period of 2 h sampling. In addition, $N_{\mathrm{INP}}$ for Leg 3's (c) first and (d) second period of 2 h LV sampling. Spectra of LV filters sampled for 8 hour prior or after the 2 hour sampling periods are given for reference (yellow). The corresponding FBF for each period plus a factor 2 (pink) for reference.
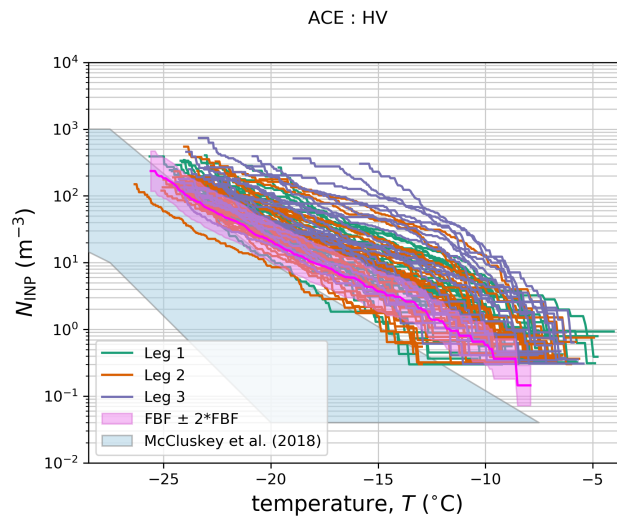


**Figure C.3:** INP number concentration as function of temperature for filters sampled for 24 h during ACE. Average spectra of FBF and corresponding factor two (pink line and area), and data range from McCluskey et al. (2018a) (light blue) for reference.

correlation analysis at 01h resolution
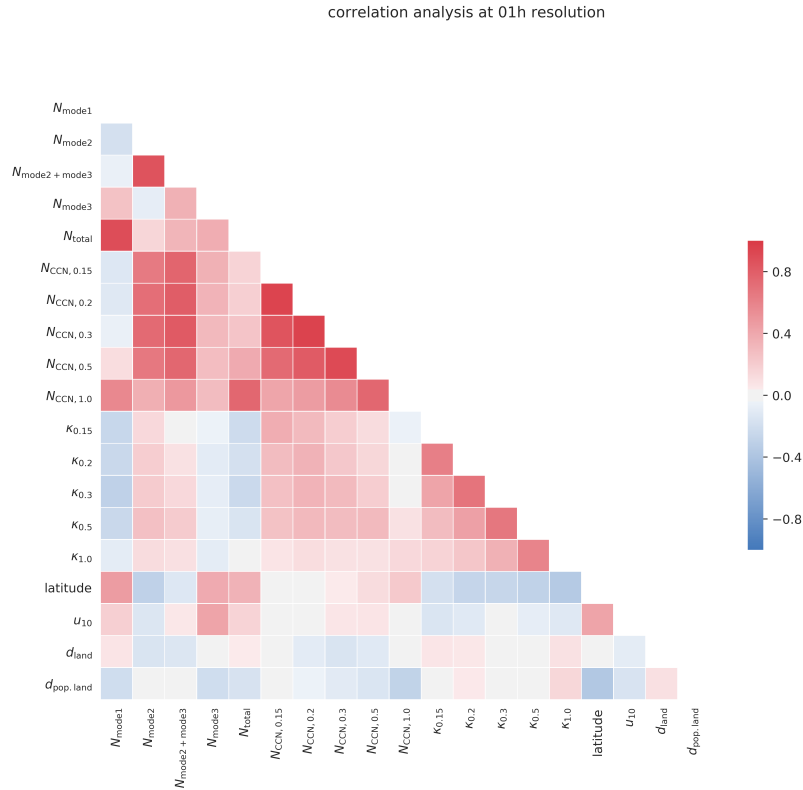


**Figure C.4:** Spearman rank correlation matrix of quantities directly measured or derived from measurements during ACE. From hourly smoothed particle number size distribution (PNSD), the total particle number concentration, respective three modes ($N_{\mathrm{mode1}}$, $N_{\mathrm{mode2}}$, and $N_{\mathrm{mode3}}$). CCN number concentration at $0.15\,\%$, $0.2\,\%$, $0.3\,\%$, $0.5\,\%$ and $1\,\%$ supersaturation ($\mathrm{CCN}(SS)$) and derived aerosol particle hygroscopicity parameter ($\kappa(SS)$) are included. Additionally, hourly-averaged latitude of the RV's position, wind speed at $10\,\mathrm{m}$ a. s. l. ($U_{10}$), distance to nearest land-mass, and distance to nearest populated land mass ($d_{\mathrm{pop.land}}$). Positive correlation between two quantities indicates a similar trend over time, while an opposing behaviour is indicated by a negative correlation coefficient.

## C.5 Parameterisation of INP abundance

In the correlation analysis in section 4.4, no connection between INP number concentration at selected $T$ and other aerosol particle parameters could be established. To further investigate how to describe the SO's INP abundance, the analysis is enhanced by considering INP number concentration at the full temperature range. Several parameterisations for atmospheric INP number concentrations are available and commonly based on the number of larger aerosol particles. In DeMott et al. (2010), a parameterisation of INP number concentration as a function of the number concentration of aerosol particles larger than 500 nm is presented. From the total PNSD for ACE (Fig. 4.2a), number concentration of aerosol particles larger than 500 nm and $N_{>700}$ were derived and a correlation analysis with the measured INP number concentration at different $T$ performed. In addition, the number of aerosol particles larger than 700 nm and 1000 nm from the Aerodynamic Particle Sizer (APS) measurements ($N_{>700,APS}$ and $N_{>1000,APS}$) were included in the correlation analysis. Fig. C.5 shows that no reasonable correlation for $N_{>500}$ and $N_{>700}$ with INP number concentration occurred. To investigate potential smoothing effects during the mode-fitting procedure that lead to the total PNSD, $N_{>700,APS}$ from the measurements of the APS instrument are included in Fig. C.5 (dotted lines). For $N_{>700,APS}$, the $T$ range with a sufficient number of data points is $-13\,°C$ to $-24\,°C$. Looking at terrestrial influenced conditions, $p$ values in Fig. C.5b indicate reasonable correlations for INP number concentration at $-16\,°C$, $-17\,°C$ and $-19\,°C$, with Spearman's rank correlation coefficient values around 0.4 (Fig. C.5a). Here, larger aerosol particles explain variability in INP concentrations in the regime of particles of biological origin. As for pristine marine conditions, $p$ values are reasonable for $T$ of $-20\,°C$, $-21\,°C$, $-22\,°C$ and $-24\,°C$. Spearman's rank correlation coefficient values are around 0.3, except for $-24\,°C$ (R = 0.5). In conclusion, variability in abundance of larger aerosol particles explains the variability of INP from mineral origin. Given what we know about INP active at different temperature regimes, $N_{>700,APS}$ composition could be different between terrestrial influenced and pristine marine conditions. In addition, $N_{>1000,APS}$ is included in Fig. C.5 (dash-dotted lines) to investigate the role of even larger particles. The number of samples considered for the correlation analysis is sufficient for the temperature range of $-13\,°C$ to $-24\,°C$. Under terrestrial influenced conditions, $p$ values indicate reasonable correlations for $-15\,°C$ to $-17\,°C$ and $-19\,°C$ to $-21\,°C$. Spearman R values ($R_S$) in Fig. C.5a show values around 0.4 for the biological INP regime and slightly lower values for the mixed INP temperature regime ($R_S = 0.3$). During the pristine marine conditions, $p$ values indicate reasonable correlations for $T$ of $-21\,°C$, $-22\,°C$ and $-24\,°C$, which is in the mineral INP regime. A peak $R_S$ of over 0.5 is apparent for $-24\,°C$, with the higher temperatures showing $R_S$ values around 0.3. In contrast to $N_{>700,APS}$, slightly higher correlation coefficients are found for $N_{>1000}$ while $N_{>700}$ has a clearer separation of the biological and mineral INP signal.

For ACE, a correlation analysis between measured and predicted INP number concentrations was performed and results are presented in Fig. C.6. As for the parameterisation proposed in DeMott et al. (2010), the number of samples is sufficient for $-13\,°C$ to $-23\,°C$. However, with $p > 0.01$ in the reasonable $T$ range it can be concluded that no reasonable correlation between measured and INP number concentration derived from $N_{>500}$ at any temperature. An update to the $N_{INP}(N_{>500})$ parameterisation in DeMott et al. (2010) is presented in Tobo et al. (2013). Within the $T$ range of sufficient number of samples ($-13\,°C$–$-23\,°C$), $p$ values are above 0.1 and thus indicate no reasonable correlation. From this and the performance of the parameterisation given in DeMott et al. (2010), it can be concluded that INP number concentration is not represented by $N_{>500}$, in agreement with what was found for Fig. C.5. In Tobo et al. (2013), a parameterisation of INP number concentration based on the number of fluorescent particles larger than 500 nm is presented. Correlation analysis of the predicted INP number concentration using this parameterisation and measured INP number concentration is presented in Fig. C.6 and shows the number of samples to be sufficient in the $T$ range between $-13\,°C$ and $-24\,°C$. For terrestrial influenced conditions, $p$ values indicate correlations for $-15$ to $-22\,°C$, and Spearman's rank correlation coefficient values are between 0.30 and 0.45. For pristine marine conditions, $p$ values indicate reasonable correlation in the biological INP regime ($-13$–$-16\,°C$) and the mineral INP regime ($-21$–$-24\,°C$). For the biological INP regime, Spearman's

rank correlation coefficient values are around $-0.3$, while in the mineral INP regime they are between 0.3 and 0.5.

PBAP were found to act as INP in studies of marine regions of the Northern hemisphere (e.g. McCluskey et al., 2018b; Hartmann et al., 2021). Under the assumption that this holds true for the Southern hemisphere as well, the connection between primary biological aerosol particle (PBAP) and INP sampled for the SO region is investigated in the following. The number concentration of fluorescent ($N_{\mathrm{FL}}$) and hyper-fluorescent PBAP ($N_{\mathrm{HFL}}$) measured during ACE are presented in Moallemi et al. (2021) and stem from measurements of a wide-band integrated bio-aerosol sensor (see subsection 3.4.4). The open ocean sections of the cruise, considered to feature pristine marine conditions, were identified by looking the distance between the RV and the nearest land mass, $d_{\mathrm{land}}$, exceeded 200 km. This is based on the idea that it is less likely to encounter an air-mass with a terrestrial signal when reasonable away from land. Moallemi et al. (2021) show that for pristine marine conditions, PBAP mainly originated from SSA.

A correlation analysis was performed between fluorescent PBAP and INP number concentrations, using the INP results for the LV samples. Correlations are characterised by their Spearman's rank correlation coefficient and $p$ value (Fig. C.7a,b). The data were categorised as terrestrial influenced (orange) and pristine marine cases (purple) using a similar threshold in $d_{\mathrm{land}}$ as Moallemi et al. (2021) (200 km). In addition, the number of samples, $n$, at each temperature is given in the figure (Fig. C.7c). Two criteria are used in the following to determine which correlation between $N_{\mathrm{FL}}$ (solid lines) or $N_{\mathrm{HFL}}$ (dashed lines) and $N_{\mathrm{INP}}$ is meaningful to interpret. Firstly, only correlations that contain a sufficiently large $n$, i.e. over 50 % of the maximum $n$, are considered. Secondly, a $p$ value below 0.05 (black line in Fig. C.7b) is used as an indication whether the respective correlation is significant. Both criteria are met for the $T$ range between $-13$ and $-24\,^{\circ}$C.

Looking at the correlation of $N_{\mathrm{FL}}$ under terrestrial influenced conditions (orange curves in Fig. C.7), a moderate positive correlation is found. $R_{\mathrm{S}}$ are slightly higher ($\sim$0.4) for temperature above $-18\,^{\circ}$C, the regime of biological INP, compared to colder temperatures ($R_{\mathrm{S}} \sim 0.28$). For pristine marine conditions (purple curves), $p$ values indicate significant correlations for $N_{\mathrm{INP},-17}$ and $N_{\mathrm{INP},-16}$. At both temperatures, $R_{\mathrm{S}}$ is around 0.3.

For the correlation between $N_{\mathrm{HFL}}$ and $N_{\mathrm{INP}}$ (dashed lines in Fig. C.7), only at $T$ between $-13$ and $-24\,^{\circ}$C a reasonable $n$ is found. Under terrestrial influenced conditions, $p$ value indicates the correlation to be significant for the temperature range from $-13\,^{\circ}$C to $-23\,^{\circ}$C (Fig. C.7b). Here, positive correlation is found for both the temperature regime of INP of biological ($T > -20\,^{\circ}$C) and mineral origin ($T < -20\,^{\circ}$C). A moderate positive correlation is indicated by $R_{\mathrm{S}}$, with slightly higher values for the biological INP regime (e.g. $-13$ and $-18\,^{\circ}$C). For pristine marine conditions, $p$ values indicate a significant correlation only for $T$ of $-16\,^{\circ}$C and $-17\,^{\circ}$C, with $R_{\mathrm{S}}$ values around 0.3.

In summary, variability in INP abundance is slightly better explained by the abundance of hyper-fluorescent PBAP. Positive correlation over a wide range of temperatures for terrestrial influenced conditions indicates that PBAP and INP originate from the same source. In contrast, under pristine marine conditions the PBAP abundance only explained the variability of mineral INP, hinting on long-range transport driving INP abundance on the open ocean. In conclusion, concentrations of larger particle from the APS instrument are capable of capturing the variability in INP, while the mode-fitting results are not able to do so. Furthermore, the variability in INP can be better explained by the variability in fluorescent PBAP. This hints on both INP and PBAP over the ocean having the same sources in the vicinity of land.
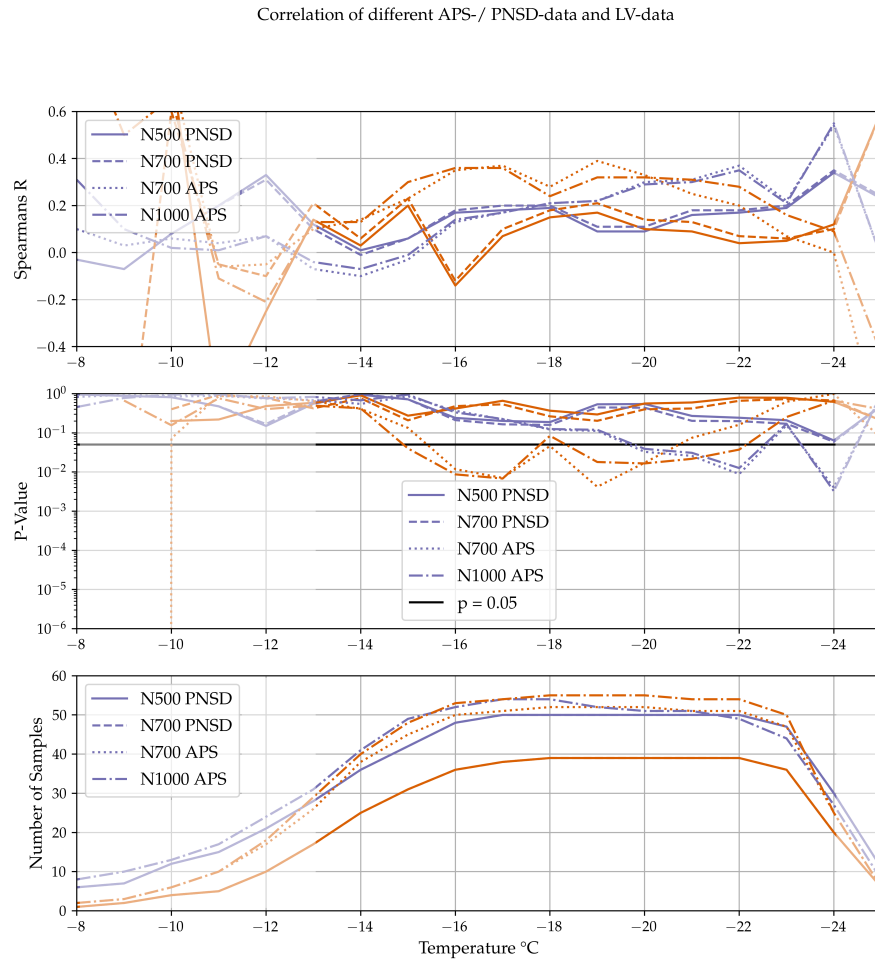
**Figure C.5:** In (a) Spearman's rank correlation coefficient and (b) respective Spearman p-value for a correlation analysis between the number concentration of aerosol particles larger than 500 nm ($N_{>500}$, solid) or larger than 700 nm ($N_{>700}$, dashed) from the total PNSD and the INP number concentration from LV sampling at different temperatures ($T$) are given. In addition, the number of particles greater than 700 nm ($N_{>700,\text{APS}}$, dotted) and 1000 nm ($N_{>1000,\text{APS}}$, dash-dotted) from the measurements of the APS instrument. Subsets of the data for pristine marine (purple) and terrestrial influenced (orange) conditions, using the distance between the RV and the distance to nearest land-mass with a threshold of 200 km. For reference, the number of samples $n$ considered for the correlation analysis is given in (c).
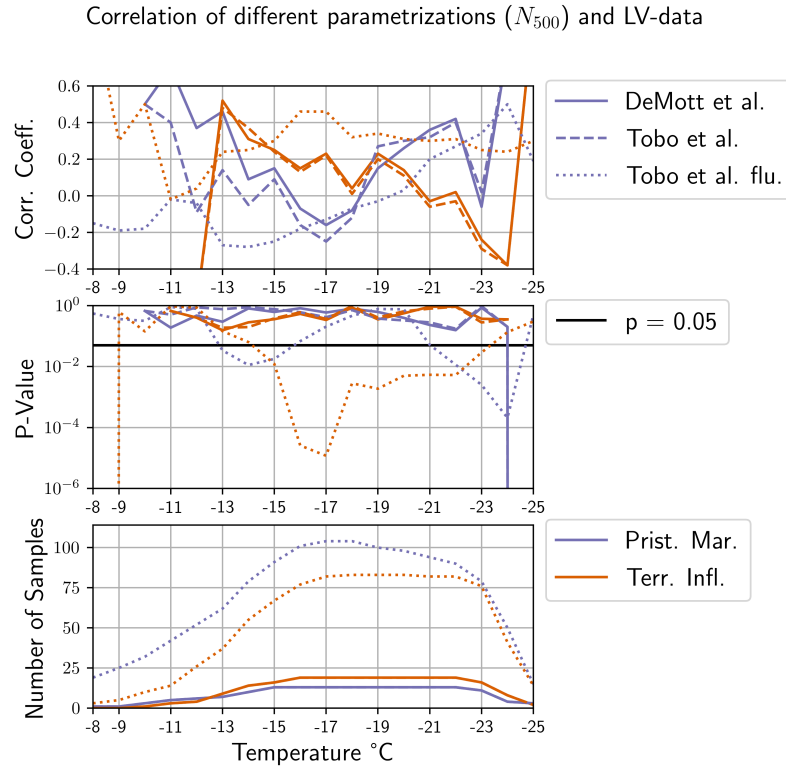
**Figure C.6:** Spearman's rank correlation coefficient values (a) and respective $p$ values (b) for a correlation analysis between the modelled INP number concentration using $N_{>500}$ and the parameterisation presented in DeMott et al. (2010) and measured INP number concentration from LV sampling at different temperatures ($T$). Subsets of the data for pristine marine (blue) and terrestrial influenced (orange) conditions, using the distance to nearest land-mass and a threshold of $200 \, \text{km}$. For reference, the number of samples $n$ for the correlation analysis is given in (c).
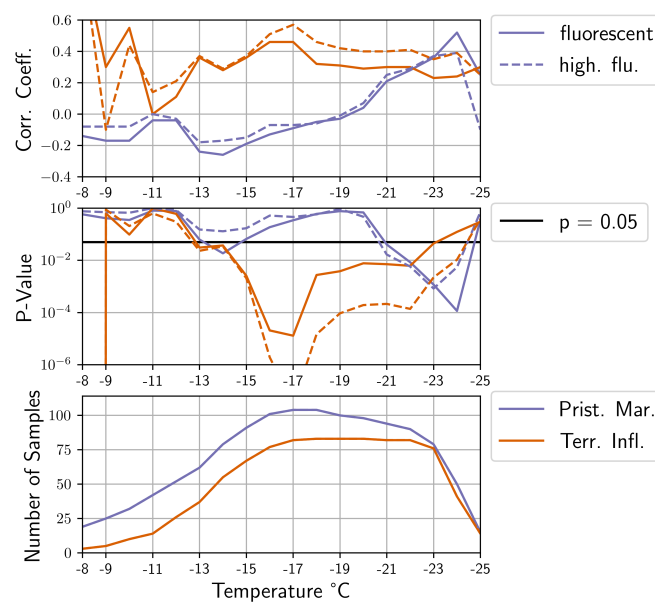
**Figure C.7:** (a) Spearman's rank correlation coefficient ($R_S$) and (b) respective Spearman p-value ($p$) for a correlation analysis between the number concentration of fluorescent ($N_{FL}$, solid) or hyper-fluorescent particles ($N_{HFL}$ dashed) and INP number concentration at different temperatures ($T$). In addition, the number of samples ($n$) is given in (c). Data on fluorescent particle measurements during ACE is available in Moallemi et al. (2021).

# Appendix D

# Case Studies

## D.1  Mertz Glacier

Some of the highest MSA mass concentration of the cruise were encountered when the RV was close to the Antarctic coast. One of those cases is when the RV reached the polynya of the Mertz Glacier around 26 January to 3 February 2017. Time-series of quantities that characterise the sampled aerosol particles and air-mass origin for the period when the RV was at Mertz Glacier are presented in Fig. D.1. In terms of air-mass origin, Fig. D.1f shows for roughly half of the investigated period that trajectories were not being available and the majority of cases with analysed trajectories show a length of 1 to 2 days. This is indicative of air-masses recently encountering precipitation events prior to reaching the RV and consequently being cut by the applied rain filter. In contrast, a few cases of backward-trajectories with the full duration (10 d) are available. As a consequence, the air-mass origin for the whole investigated period is dominated by PBL signals (Fig. D.1g). The period is characterised by a continuous, almost uninterrupted presence of a surface cyclone (Fig. D.1e), with two short interruptions surface cyclone activity (28 January and 2 February 2017). Prior to the RV arriving at the Mertz Glacier polynya, the surface signal in the air-mass origin is dominated by open ocean signals (Fig. D.1h), with short sea ice signals up to $50\,\%$ contribution. Geographically, these open ocean signals initially stem from north of 60°S (Fig. D.1i) and after 27 January from within the SO region. When the RV reaches the polynya of Mertz Glacier, the FT signal increases (Fig. D.1g) while the PBL signals are solely terrestrial (Fig. D.1h) originating from Antarctica (Fig. D.1i). The daily MSA mass concentrations during this period (Fig. D.1d) include two samples with elevated values ($>300\,\mathrm{ng\,m^{-3}}$), while mass concentrations for the remaining days are below $100\,\mathrm{ng\,m^{-3}}$. The first HV sample with elevated MSA mass concentration, the one from 28 January, coincides with distance to nearest land-mass in Fig. D.1d reaching the minimum for the investigated period, indicating the RV reaching the Mertz Glacier polynya. At 28 January, availability of a PNSD is patchy (Fig. D.1a), indicating filtering for ship exhaust air or missing instrument availability. Prior to and during 28 January, a sudden change from cold air advection (CAA) to warm air advection (WAA) is apparent (Fig. D.1e). Unavailability of trajectories (Fig. D.1g) prior and after the WAA event indicates rain falling at the RV's position in conjunction with respective frontal zones. The second day with elevated MSA mass concentration, 1 February, coincides with distance to nearest land-mass being around $100\,\mathrm{km}$ and increasing. For 1 February, PNSD in Fig. D.1a shows a short increase in particle concentration around $10\,\mathrm{nm}$ and increase in total particle number concentration (Fig. D.1b). During 1 February, air-mass origin at the RV position is characterised by CAA (Fig. D.1e) and short trajectories ($<24\,\mathrm{h}$) of purely surface signals (Fig. D.1g). Surface signals in the air-mass origin stem mostly from sea ice (Fig. D.1h) on the SO (Fig. D.1i). On 30 January, an increase in Aitken mode particle concentration is visible in the PNSD (Fig. D.1a). Simultaneously, total particle number concentration increases to $>1000\,\mathrm{cm^{-3}}$ (Fig. D.1b).

Overall, the results of the analysis regarding the air-mass origin are inconclusive in terms of a

source for the peak MSA mass concentrations. Both days that feature elevated MSA mass concentration, 28 January and 1 February 2017, are similar in terms of short backward-trajectory duration, due to precipitation, and were only within the PBL. For 28 January, PBL signals are mainly from coastal regions of Antarctica and to a smaller extend from sea ice, marginal ice zone (MIZ), and open ocean on the SO. For 1 February 2017, signals are from SO sea ice, MIZ (40–100 %), and open ocean (0–60 %). Both cases are similar in that the surface signal type is dominated by MIZ and sea ice signals. However, this is also the case for 31 January 2017, which shows a MSA mass concentration below $100\,\mathrm{ng\,m^{-3}}$.

## D.2   Ross Sea

The second case of elevated MSA mass concentrations occurred when the RV was on the Ross Sea (170°E–160°W) and close to the Antarctic sea ice edge, in the period between 5 February and 10 February 2017. In Fig. D.2, time-series of quantities characterising the sampled aerosol particles (a–e) and air-mass origin (f–i) for the period on the Ross Sea are presented. During the investigated period, MSA mass concentration increases over three consecutive days, from $100\,\mathrm{ng\,m^{-3}}$ to $300\,\mathrm{ng\,m^{-3}}$ (Fig. D.2d). On 8 February, $M_{\mathrm{MSA}}$ is below the limit of detection and PNSD (Fig. D.2a) are not available due to data filtering. Furthermore, the backward trajectories are not available for that day, indicating precipitation at the position of the RV (Fig. D.2f). On 9 February, the maximum in $M_{\mathrm{MSA}}$ for the investigated period of $400\,\mathrm{ng\,m^{-3}}$ occurred, coinciding with a distinct Aitken mode (Fig. D.2a). For that day, Fig. D.2b shows an increase in total particle number concentration and CCN number concentration. Air-mass origin shows mostly trajectories with a length below 48 h and lacking FT signals. Trajectories with a signal from the FT occurred less often and generally exhibit lengths of 96 h or longer. As for the surface type of the PBL signals, Fig. D.2g shows mostly open ocean signals, with terrestrial or iced surface signals occurring sporadically. As for geo-location of the PBL signals, Fig. D.2i shows all terrestrial signals (land and coast) to stem from Antarctica, while all maritime signals (open ocean, MIZ, and sea ice) to stem from the SO.

Overall, the increase in MSA mass concentration over the investigated period marks an interesting feature and the only parameter increasing in parallel is distance to nearest land-mass. Other parameters are highly variable throughout that period, e.g. air-mass origin is dominated by either PBL or FT signals. The development and subsequent dissipation of an distinct Aitken mode under condition of elevated MSA mass concentration marks an interesting feature.
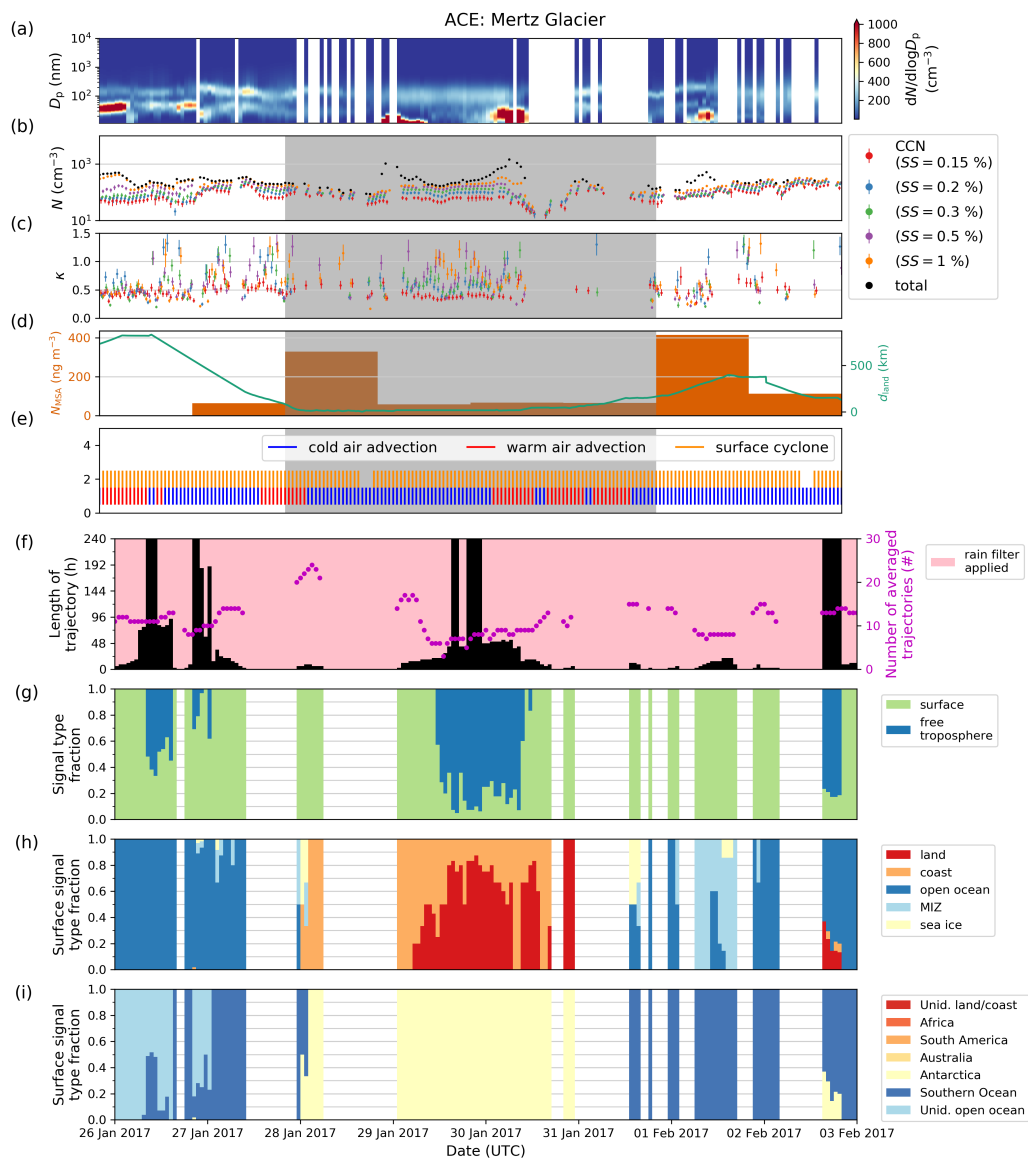
**Figure D.1:** Time series of (a) PNSD, (b) total particle number concentration ($N_{\text{total}}$, black) and CCN number concentration (color-coded), (c) hygroscopicity parameter, (d) MSA mass concentration (orange) and distance between RV's position and closest land-mass ($d_{\text{land}}$, green), (e) surface cyclone mask and cold/warm air advection mask for the period when the RV was close to Mertz Glacier. The period when distance to nearest land-mass is below 200 km is indicated (grey shading). In addition, results of the trajectory analysis regarding the surface signal including each (f) trajectory duration, (g) contribution of PBL and FT signal, (h) surface type information, and (i) geo-location information of the surface signal.
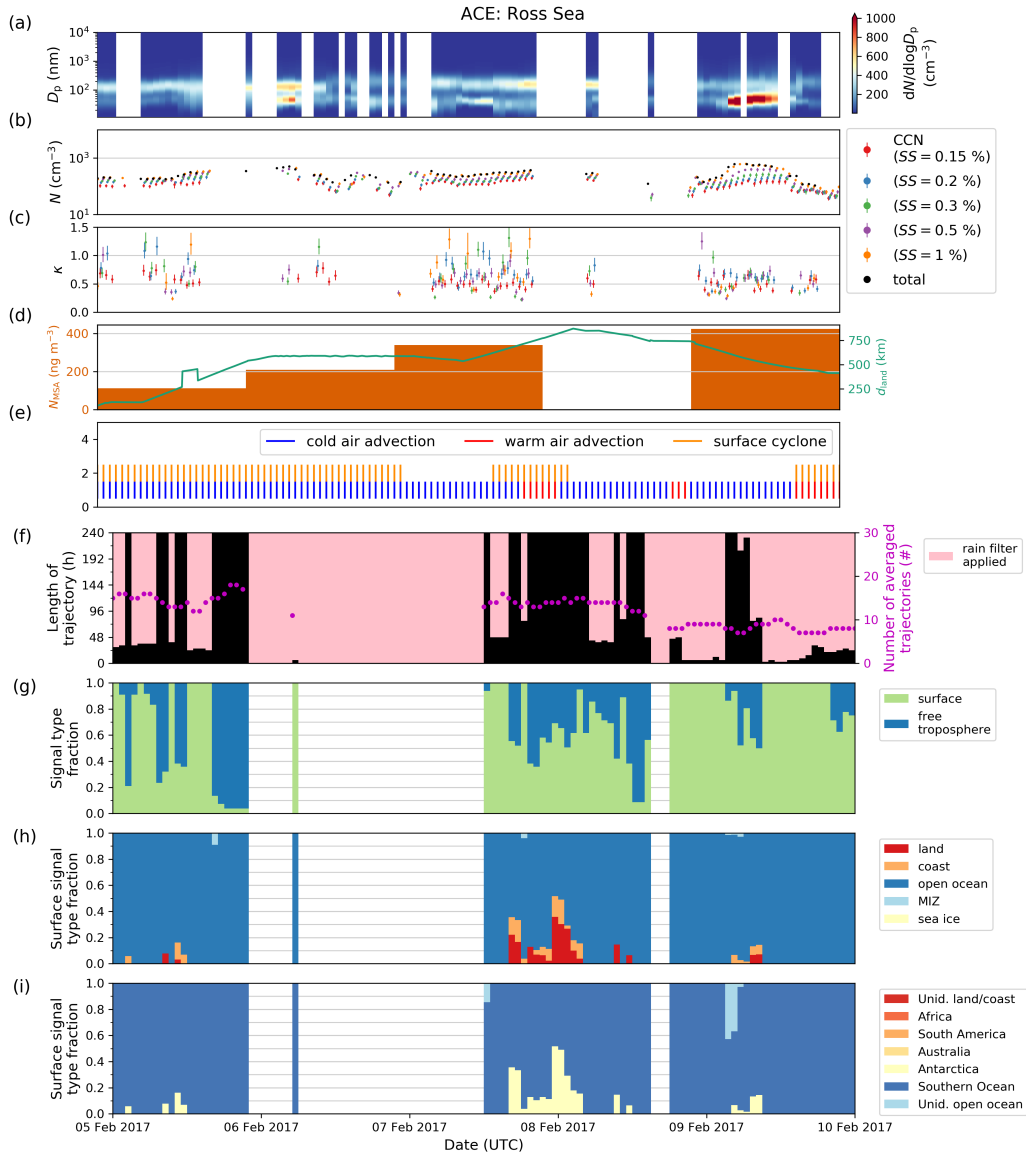
**Figure D.2:** Time series of (a) particle number size distribution (PNSD), (b) particle number concentration of total particle ($N_{total}$, black) and CCN number concentration (color-coded), (c) hygroscopicity parameter, (d) MSA mass concentration (orange) and distance between RV's position and closest land-mass ($d_{land}$, green), (e) surface cyclone mask and cold/warm air advection mask for the period when the RV was on the Ross Sea. The period when distance to nearest land-mass is below 200 km is indicated (grey shading). In addition, results of the trajectory analysis regarding the surface signal including each (f) trajectory duration, (g) contribution of PBL and FT signal, (h) surface type information, and (i) geo-location information of the surface signal.

# List of Abbreviations

| | |
|---|---|
| **ACE** | Antarctic Circum-navigation Expedition |
| **ACE-SPACE** | Study of Preindustrial-like Aerosol Climate Effects |
| **ACE-1** | $1^{st}$ Aerosol Characterisation Experiment |
| **APS** | Aerodynamic Particle Sizer |
| **BSO** | British Southern Ocean |
| **BVOC** | biological volatile organic compounds |
| **CAA** | cold air advection |
| **CAPRICORN** | Clouds, Aerosols, Precipitation, Radiation and atmospherIc Composition Over the southeRn oceaN |
| **CCN** | cloud condensation nucleus |
| **CCNC** | CCN Counter |
| **CGBS** | Cape Grim Baseline Station |
| **CHINARE** | Chinese National Antarctic and Arctic Research Expedition |
| **Chl** $a$ | chlorophyll a |
| **CPC** | Condensation Particle Counter |
| **CSV** | comma-separated values |
| **CTD** | conductivity, temperature and depth |
| **DMA** | Differential Mobility Analyser |
| **DMS** | dimethyl sulphide |
| **EC** | elemental carbon |
| **ECMWF** | European Centre for Medium Range Weather Forecasts |
| **FBF** | field blank filter |
| **FT** | free troposphere |
| **gmean** | geometric mean |
| **gSD** | geometric standard deviation |
| **HV** | high-volume |
| **IFS** | ECMWF Integrated Forcasting System |
| **INDA** | ice nucleation droplet array |
| **INP** | ice-nucleating particle |
| **IQR** | inter-quartile range |
| **LAGRANTO** | LAGRANgian analysis TOol |
| **LED** | light-emitting diode |
| **LV** | low-volume |
| **MAC** | Micro-physics of Antarctic Clouds |
| **MARCUS** | Measurements of Aerosols, Radiation, and CloUds over the Southern oceans |
| **MBL** | marine boundary layer |
| **MCS** | Monte Carlo simulation |
| **MICRE** | Macquarie Island Cloud and Radiation Experiment |
| **MIZ** | marginal ice zone |
| **MSA** | methanesulfonic acid |

| | |
|---|---|
| **NPF** | new particle formation |
| **nss** | non-sea salt |
| **OC** | organic content |
| **PBAP** | primary biological aerosol particle |
| **PBL** | planetary boundary layer |
| **PCR** | polymerase chain reaction |
| **PDF** | probability density function |
| **PEGASO** | Plankton-derived Emissions of trace Gases and Aerosols in the Southern Ocean |
| **PES** | Princess Elisabeth station |
| **PM** | pristine marine conditions |
| **PNSD** | particle number size distribution |
| **PSI** | Paul Scherrer Institute |
| **RITS** | Radiatively Important Trace Species |
| **RV** | research vessel |
| **SI** | supporting information |
| **SMPS** | Spinning Mobility Particle Analyser |
| **SO** | Southern Ocean |
| **SOCEX** | Southern Ocean Cloud EXperiment |
| **SOCRATES** | Southern Ocean Clouds, Radiation, Aerosol Transport Experimental Study |
| **SORPASSO** | Surveying Organic Reactive gases and Particles Across the Surface Southern Ocean |
| **SSA** | sea spray aerosol |
| **TI** | terrestrial-influenced conditions |
| **TROPOS** | Leibniz-Institute for Tropospheric Research |
| **VOC** | volatile organic compounds |
| **WAA** | warm air advection |
| **WSOC** | water-soluble organic carbon |

# List of Symbols

| | | |
|---|---|---|
| $A_\mathrm{n}$ | $(\mathrm{nm}^2)$ | Surface area of the INP |
| $D$ | $(\mathrm{nm})$ | Droplet diameter |
| $D_\mathrm{act}$ | $(\mathrm{nm})$ | Critical activation diameter |
| $D_\mathrm{crit}$ | $(\mathrm{nm})$ | Critical dry diameter |
| $D_\mathrm{filter}$ | $(\mathrm{mm})$ | Diameter of sampled filter |
| $D_\mathrm{p}$ | $(\mathrm{nm})$ | Dry particle diameter |
| $D_\mathrm{punchout}$ | $(\mathrm{mm})$ | Diameter of the punch-out |
| $D_\mathrm{u}$ | $(\mathrm{nm})$ | Dry diameter |
| $d_\mathrm{land}$ | $(\mathrm{km})$ | Distance to nearest land-mass |
| $e$ | $(\mathrm{kPa})$ | Water vapour pressure |
| $e_\mathrm{sat}$ | $(\mathrm{kPa})$ | Saturation vapour pressure |
| $\Delta F$ | $(\mathrm{J})$ | Activation energy for diffusion of molecules across the liquid-solid interface |
| $f$ | | Reduction factor |
| $f_\mathrm{ice}$ | | Frozen fraction |
| $\Delta G$ | $(\mathrm{J})$ | Gibbs free energy |
| $\Delta G_\mathrm{het}$ | $(\mathrm{J})$ | Gibbs free energy of heterogeneous nucleation |
| $\Delta G_\mathrm{het}^*$ | $(\mathrm{J})$ | Critical Gibbs free energy of heterogeneous nucleation |
| $\Delta G_\mathrm{hom}$ | $(\mathrm{J})$ | Gibbs free energy of homogeneous nucleation |
| $\Delta G_\mathrm{hom}^*$ | $(\mathrm{J})$ | Critical Gibbs free energy of homogeneous nucleation |
| $\Delta G_\mathrm{S}$ | $(\mathrm{J})$ | Surface term |
| $\Delta G_\mathrm{V}$ | $(\mathrm{J})$ | Volume term |
| $h$ | $(\mathrm{J\,s})$ | Planck constant |
| $j_\mathrm{hom}$ | $(\mathrm{m}^2\,\mathrm{s}^{-1})$ | Homogeneous nucleation rate coefficient |
| $j_\mathrm{het}$ | $(\mathrm{m}^2\,\mathrm{s}^{-1})$ | Heterogeneous nucleation rate coefficient |
| $k$ | | Number of active sites |
| $k_\mathrm{B}$ | $(\mathrm{J\,K}^{-1})$ | Boltzmann constant |
| $\kappa$ | | Hygroscopicity parameter |
| $M$ | $(\mathrm{\mu g\,m}^{-3})$ | Particle mass concentration |
| $M_\mathrm{MSA}$ | $(\mathrm{ng\,m}^{-3})$ | MSA mass concentration |
| $M_\mathrm{Na^+}$ | $(\mathrm{\mu g\,m}^{-3})$ | Sodium mass concentration |
| $M_\mathrm{nss\,SO_4^{2-}}$ | $(\mathrm{\mu g\,m}^{-3})$ | Non-sea salt sulphate mass concentration |
| $M_\mathrm{SO_4^{2-}}$ | $(\mathrm{\mu g\,m}^{-3})$ | Sulphate mass concentration |
| $M_\mathrm{w}$ | $(\mathrm{g\,mol}^{-1})$ | Molecular mass of water |
| $N$ | $(\mathrm{cm}^{-3})$ | Particle number concentration |
| $N_\mathrm{CCN}$ | $(\mathrm{cm}^{-3})$ | CCN number concentration |
| $N_\mathrm{FL}$ | $(\mathrm{m}^{-3})$ | Number concentration of fluorescent PBAP |
| $N_\mathrm{HFL}$ | $(\mathrm{m}^{-3})$ | Number concentration of hyper-fluorescent PBAP |
| $N_\mathrm{INP}$ | $(\mathrm{m}^{-3})$ | INP number concentration |
| $N_\mathrm{mode1}$ | $(\mathrm{cm}^{-3})$ | Total number concentration of particles in the fitted Aitken mode |

| | | |
|---|---|---|
| $N_{\mathrm{mode2}}$ | (cm$^{-3}$) | Total number concentration of particles in the fitted accumulation mode |
| $N_{\mathrm{mode3}}$ | (cm$^{-3}$) | Total number concentration of particles in the fitted sea spray mode |
| $N_{\mathrm{total}}$ | (cm$^{-3}$) | Total particle number concentration |
| $N_{>500}$ | (cm$^{-3}$) | Number concentration of aerosol particles larger than 500 nm |
| $N_{>700}$ | (cm$^{-3}$) | Number concentration of aerosol particles larger than 700 nm |
| $N_{>1000}$ | (cm$^{-3}$) | Number concentration of aerosol particles larger than 1 µm |
| $n$ | | Number of samples |
| $n^*$ | | Number of critical clusters |
| $n_{\mathrm{d}}$ | | Number of droplets |
| $n_{\mathrm{fr}}$ | | Number of frozen droplets |
| $n_{\mathrm{i/l}}$ | (m$^{-3}$) | Number density of water molecules at the interface of critical cluster and super-cooled liquid water |
| $n_{\mathrm{l}}$ | (m$^{-3}$) | Number density of molecules in the liquid phase |
| $n_{\mathrm{s}}$ | (cm$^{-2}$) | Ice-active site density |
| $n_{\mathrm{sol}}$ | | Number of moles of solute |
| $n_{\mathrm{ufr}}$ | | Number of unfrozen droplets |
| $n_{\mathrm{v}}$ | (cm$^{-3}$) | Ice-active volume density |
| PM$_1$ | | Particulate matter smaller than 1 µm |
| PM$_{10}$ | | Particulate matter smaller than 10 µm |
| PM$_{40}$ | | Particulate matter smaller than 40 µm |
| $p$ | | Spearman p-value |
| $p_{\mathrm{par}}$ | (hPa) | Pressure level of the air parcel |
| $p_{\mathrm{PBL}}$ | (hPa) | Pressure level of the PBL |
| $R$ | | Universal gas constant |
| $R_{\mathrm{S}}$ | | Spearman's rank correlation coefficient |
| $R_{\mathrm{total}}$ | (mm) | Total precipitation |
| $RH$ | (%) | Relative humidity |
| $r$ | (nm) | Cluster radius |
| $r^*$ | (nm) | Critical cluster radius |
| $\rho_{\mathrm{w}}$ | (g ml$^{-1}$) | Density of water |
| $S$ | | Saturation ratio |
| $SS$ | (%) | Level of supersaturation |
| $SS_{\mathrm{crit}}$ | (%) | Critical supersaturation |
| $\sigma_{\mathrm{i/l}}$ | (N m$^{-1}$) | Inter-facial energy between liquid and solid phase |
| $\sigma_{\mathrm{n/i}}$ | (N m$^{-1}$) | Inter-facial energy between nucleus and solid phase |
| $\sigma_{\mathrm{n/l}}$ | (N m$^{-1}$) | Inter-facial energy between nucleus and liquid phase |
| $\sigma_{\mathrm{w}}$ | (mN m$^{-1}$) | Surface tension of water |
| $T$ | (°C) | Temperature |
| $T_{\mathrm{c}}$ | (°C) | Characteristic temperature |
| $T_{\mathrm{min}}$ | (°C) | Minimum temperature |
| $t$ | (s) | Time |
| $\theta$ | (°) | Contact angle |
| $U_{10}$ | (m s$^{-1}$) | Wind speed at 10 m a. s. l. |
| $V_{\mathrm{d}}$ | (nm$^3$) | Droplet volume |
| $V_{\mathrm{flow}}$ | (m$^3$) | Volume of sampled air |
| $V_{\mathrm{ref}}$ | (m$^3$) | Reference volume |
| $V_{\mathrm{water}}$ | (mL) | Volume of washing water |
| $v$ | (m$^3$) | Liquid volume occupied by one molecule |
| $w$ | (s$^{-1}$) | Diffusive flux of water molecules across the liquid-solid interface |

# List of Figures

# List of Tables

# References

Abram, N. J., E. R. Thomas, J. R. McConnell, R. Mulvaney, T. J. Bracegirdle, L. C. Sime, and A. J. Aristarain, 2010: Ice core evidence for a 20th century decline of sea ice in the Bellingshausen Sea, Antarctica. *J. Geophys. Res.: Atmos.*, **115**, doi:10.1029/2010JD014644.

Agresti, A. and B. A. Coull, 1998: Approximate is better than "exact" for interval estimation of binomial proportions. *The American Statistician*, **52**, 119–126, doi:10.1080/00031305.1998.10480550.

Albrecht, B. A., 1989: Aerosols, Cloud Microphysics, and Fractional Cloudiness. *Science*, **245**, 1227–1230, doi:10.1126/science.245.4923.1227.

Andreae, M. and D. Rosenfeld, 2008: Aerosol–cloud–precipitation interactions. Part 1. The nature and sources of cloud-active aerosols. *Earth-Sci. Rev.*, **89**, 13–41, doi:10.1016/j.earscirev.2008.03.001.

Andreae, M. O. and H. Raemdonck, 1983: Dimethyl sulfide in the surface ocean and the marine atmosphere: a global view. *Science*, **221**, 744–747, doi:10.1126/science.221.4612.744.

Asmi, A., M. Collaud Coen, J. Ogren, E. Andrews, P. Sheridan, A. Jefferson, E. Weingartner, U. Baltensperger, N. Bukowiecki, H. Lihavainen, et al., 2013: Aerosol decadal trends–part 2: Insitu aerosol particle number concentrations at GAW and ACTRIS stations. *Atmos. Chem. Phys.*, **13**, 895–916, doi:10.5194/acp-13-895-2013.

Ayers, G., J. Cainey, R. Gillett, and J. Ivey, 1997: Atmospheric sulphur and cloud condensation nuclei in marine air in the Southern Hemisphere. *Phil. Trans. R. Soc. Lond. B*, **352**, 203–211, doi:10.1098/rstb.1997.0015.

Ayers, G. and J. Gras, 1991: Seasonal relationship between cloud condensation nuclei and aerosol methanesulphonate in marine air. *Nature*, **353**, 834–835, doi:10.1038/353834a0.

Baccarini, A., J. Dommen, K. Lehtipalo, S. Henning, R. L. Modini, M. Gysel-Beer, U. Baltensperger, and J. Schmale, 2021: Low-volatility vapors and new particle formation over the Southern Ocean during the Antarctic Circumnavigation Expedition. *Earth and Space Science Open Archive*, 31, doi:10.1002/essoar.10506899.1.

Bates, T. S., B. J. Huebert, J. L. Gras, F. B. Griffiths, and P. A. Durkee, 1998a: International Global Atmospheric Chemistry (IGAC) project's first aerosol characterization experiment (ACE 1): Overview. *J. Geophys. Res.: Atmos.*, **103**, 16297–16318.

Bates, T. S., V. N. Kapustin, P. K. Quinn, D. S. Covert, D. J. Coffman, C. Mari, P. A. Durkee, W. J. De Bruyn, and E. S. Saltzman, 1998b: Processes controlling the distribution of aerosol particles in the lower marine boundary layer during the First Aerosol Characterization Experiment (ACE 1). *J. Geophys. Res.: Atmos.*, **103**, 16369–16383, doi:10.1029/97JD03720.

Bates, T. S. and P. K. Quinn, 1997: Dimethylsulfide (DMS) in the equatorial Pacific Ocean (1982 to 1996): Evidence of a climate feedback? *Geophys. Res. Lett.*, **24**, 861–864.

Bigg, E., 1973: Ice nucleus concentrations in remote areas. *J. Atmos. Sci.*, **30**, 1153–1157, doi:10.1175/1520-0469(1973)030<1153:INCIRA>2.0.CO;2.

— 1990: Long-term trends in ice nucleus concentrations. *Atmos. Res.*, **25**, 409–415, doi:10.1016/0169-8095(90)90025-8.

Bigg, E., S. Mossop, R. Meade, and N. Thorndike, 1963: The measurement of ice nucleus concentrations by means of millipore filters. *J. Appl. Meteor.*, **2**, 266–269, doi:10.1175/1520-0450(1963)002<0266:TMOINC>2.0.CO;2.

Blanchard, D. and A. Woodcock, 1957: Bubble formation and modification in the sea and its meteorological significance. *Tellus*, **9**, 145–158, doi:10.3402/tellusa.v9i2.9094.

Boers, R., J. Jensen, and P. Krummel, 1998: Microphysical and short-wave radiative structure of stratocumulus clouds over the southern ocean: Summer results and seasonal differences. *Q. J. R. Meteorol. Soc.*, **124**, 151–168, doi:10.1002/qj.49712454507.

Boers, R., J. B. Jensen, P. B. Krummel, and H. Gerber, 1996: Microphysical and short-wave radiative structure of wintertime stratocumulus clouds over the southern ocean. *Q. J. R. Meteorol. Soc.*, **122**, 1307–1339, doi:10.1002/qj.49712253405.

Cantrell, W. and A. Heymsfield, 2005: Production of ice in tropospheric clouds: A review. *Bull. Amer. Meteor. Soc.*, **86**, 795–808.

Carslaw, K., L. Lee, C. Reddington, K. Pringle, A. Rap, P. Forster, G. Mann, D. Spracklen, M. Woodhouse, L. Regayre, et al., 2013: Large contribution of natural aerosols to uncertainty in indirect forcing. *Nature*, **503**, 67, doi:10.1038/nature12674.

Castebrunet, H., P. Martinerie, C. Genthon, and E. Cosme, 2009: A three-dimensional model study of methanesulphonic acid to non sea salt sulphate ratio at mid and high-southern latitudes. *Atmos. Chem. Phys.*, **9**, 9449–9469, doi:10.5194/acp-9-9449-2009.

Cavalieri, D. J., J. P. Crawford, M. R. Drinkwater, D. T. Eppler, L. D. Farmer, R. R. Jentz, and C. C. Wackerman, 1991: Aircraft active and passive microwave validation of sea ice concentration from the defense meteorological satellite program special sensor microwave imager. *J. Geophys. Res.: Ocean.*, **96**, 21989–22008, doi:10.1029/91JC02335.

Cavalli, F., M. C. Facchini, S. Decesari, M. Mircea, L. Emblico, S. Fuzzi, D. Ceburnis, Y. J. Yoon, C. D. O'Dowd, J.-P. Putaud, and A. Dell'Acqua, 2004: Advances in characterization of size-resolved organic matter in marine aerosol over the north atlantic. *J. Geophys. Res.: Atmos.*, **109**, doi:10.1029/2004JD005137.

Cavalli, F., M. Viana, K. E. Yttri, J. Genberg, and J.-P. Putaud, 2010: Toward a standardised thermal-optical protocol for measuring atmospheric organic and elemental carbon: the EUSAAR protocol. *Atmos. Meas. Tech.*, **3**, 79–89, doi:10.5194/amt-3-79-2010.

Chen, H., M. J. Ezell, K. D. Arquero, M. E. Varner, M. L. Dawson, R. B. Gerber, and B. J. Finlayson-Pitts, 2015: New particle formation and growth from methanesulfonic acid, trimethylamine and water. *Phys. Chem. Chem. Phys.*, **17**, 13699–13709, doi:10.1039/C5CP00838G.

Chen, Q., T. Sherwen, M. Evans, and B. Alexander, 2018: DMS oxidation and sulfur aerosol formation in the marine troposphere: a focus on reactive halogen and multiphase chemistry. *Atmos. Chem. Phys.*, **18**, 13617–13637, doi:10.5194/acp-18-13617-2018.

Clarke, A., J. Varner, F. Eisele, R. Mauldin, D. Tanner, and M. Litchy, 1998: Particle production in the remote marine atmosphere: Cloud outflow and subsidence during ace 1. *J. Geophys. Res.: Atmos.*, **103**, 16397–16409, doi:10.1029/97JD02987.

Conen, F., S. Henne, C. E. Morris, and C. Alewell, 2012: Atmospheric ice nucleators active $\geq -12°C$ can be quantified on $pm_{10}$ filters. *Atmos. Meas. Tech.*, **5**, 321–327, doi:10.5194/amt-5-321-2012.

Connolly, P., O. Möhler, P. Field, H. Saathoff, R. Burgess, T. Choularton, and M. Gallagher, 2009: Studies of heterogeneous freezing by three different desert dust samples. *Atmos. Chem. Phys.*, **9**, 2805–2824, doi:10.5194/acp-9-2805-2009.

Covert, D. S., V. N. Kapustin, P. K. Quinn, and T. S. Bates, 1992: New particle formation in the marine boundary layer. *J. Geophys. Res.: Atmos.*, **97**, 20581–20589, doi:10.1029/92JD02074.

Creamean, J. M., C. Mignani, N. Bukowiecki, and F. Conen, 2019: Using freezing spectra characteristics to identify ice-nucleating particle populations during the winter in the alps. *Atmos. Chem. Phys.*, **19**, 8123–8140, doi:10.5194/acp-19-8123-2019.

Curran, M. A., T. D. van Ommen, V. I. Morgan, K. L. Phillips, and A. S. Palmer, 2003: Ice core evidence for Antarctic sea ice decline since the 1950s. *Science*, **302**, 1203–1206, doi:10.1126/science.1087888.

Dall'Osto, M., J. Ovadnevaite, M. Paglione, D. C. Beddows, D. Ceburnis, C. Cree, P. Cortés, M. Zamanillo, S. O. Nunes, G. L. Pérez, et al., 2017: Antarctic sea ice region as a source of biogenic organic nitrogen in aerosols. *Sci. Rep.*, **7**, 6047, doi:10.1038/s41598-017-06188-x.

Davison, B., C. O'Dowd, C. Hewitt, M. Smith, R. Harrison, D. Peel, E. Wolf, R. Mulvaney, M. Schwikowski, and U. Baltenspergert, 1996: Dimethyl sulfide and its oxidation products in the atmosphere of the Atlantic and Southern Oceans. *Atmos. Env.*, **30**, 1895 – 1906, doi:10.1016/1352-2310(95)00428-9, joint 8th CAGCP and 2nd IGAC Conference on Global Atmospheric Chemistry.

de Leeuw, G., E. L. Andreas, M. D. Anguelova, C. W. Fairall, E. R. Lewis, C. O'Dowd, M. Schulz, and S. E. Schwartz, 2011: Production flux of sea spray aerosol. *Rev. Geophys.*, **49**, doi:10.1029/2010RG000349.

DeMott, P. J., T. C. Hill, R. Marchand, and S. Alexander, 2018: Macquarie Island Cloud and Radiation Experiment (MICRE) Ice Nucleating Particle Measurements Field Campaign Report. Technical report, DOE Office of Science Atmospheric Radiation Measurement (ARM) Program . . . .

DeMott, P. J., T. C. Hill, C. S. McCluskey, K. A. Prather, D. B. Collins, R. C. Sullivan, M. J. Ruppel, R. H. Mason, V. E. Irish, T. Lee, et al., 2016: Sea spray aerosol as a unique source of ice nucleating particles. *Proc. Nat. Acad. Sci. USA*, **113**, 5797–5803.

DeMott, P. J., A. J. Prenni, X. Liu, S. M. Kreidenweis, M. D. Petters, C. H. Twohy, M. Richardson, T. Eidhammer, and D. Rogers, 2010: Predicting global atmospheric ice nuclei distributions and their impacts on climate. *Proceedings of the National Academy of Sciences*, **107**, 11217–11222, doi:10.1073/pnas.0910818107.

Dusek, U., G. Frank, L. Hildebrandt, J. Curtius, J. Schneider, S. Walter, D. Chand, F. Drewnick, S. Hings, D. Jung, et al., 2006: Size matters more than chemistry for cloud-nucleating ability of aerosol particles. *Science*, **312**, 1375–1378, doi:10.1126/science.1125261.

Efraim, A., D. Rosenfeld, J. Schmale, and Y. Zhu, 2020: Satellite retrieval of cloud condensation nuclei concentrations in marine stratocumulus by using clouds as CCN chambers. *J. Geophys. Res.: Atmos.*, **125**, doi:10.1029/2020JD032409.

Fletcher, N. H., 1959: Entropy effect in ice crystal nucleation. *J. Chem. Phys.*, **30**, 1476–1482, doi:10.1063/1.1730221.

Forster, P., T. Storelvmo, K. Armour, W. Collins, J. Dufresne, D. Frame, D. Lunt, T. Maurit-sen, M. Palmer, M. Watanabe, M. Wild, H. Zhang, et al., 2021: The Earth's Energy Budget, Climate Feedbacks and Climate Sensitivity. *Climate Change 2021: The Physical Science Basis. Contribution of Working Group I to the Sixth Assessment Report of the Intergovernmental Panel on Climate Change*, V. Masson-Delmotte, P. Zhai, A. Pirani, S. Conners, C. Péan, S. Berger, N. Caud, Y. Chen, L. Goldfarb, M. Gomis, M. Huang, K. Leitzell, E. Lonnoy, J. Matthews, T. Maycook, T. Waterfield, O. Yelekçi, R. Yu, and B. Zhou, eds., Cambridge University Press, Cambridge, United Kingdom and New York, NY, USA, chapter 7, 923–1054.

Fossum, K. N., J. Ovadnevaite, D. Ceburnis, M. Dall'Osto, S. Marullo, M. Bellacicco, R. Simó, D. Liu, M. Flynn, A. Zuend, et al., 2018: Summertime primary and secondary contributions to southern ocean cloud condensation nuclei. *Sci. Rep.*, **8**, 13844, doi:10.1038/s41598-018-32047-4.

Fossum, K. N., J. Ovadnevaite, D. Ceburnis, J. Preißler, J. R. Snider, R.-J. Huang, A. Zuend, and C. O'Dowd, 2020: Sea-spray regulates sulfate cloud droplet activation over oceans. *npj Clim. Atmos. Sci.*, **3**, 1–6, doi:10.1038/s41612-020-0116-2.

Gong, X., H. Wex, M. van Pinxteren, N. Triesch, K. W. Fomba, J. Lubitz, C. Stolle, T.-B. Robinson, T. Müller, H. Herrmann, et al., 2020a: Characterization of aerosol particles at Cabo Verde close to sea level and at the cloud level–Part 2: Ice-nucleating particles in air, cloud and seawater. *Atmos. Chem. Phys.*, **20**, 1451–1468, doi:10.5194/acp-20-1451-2020.

Gong, X., H. Wex, J. Voigtländer, K. W. Fomba, K. Weinhold, M. van Pinxteren, S. Henning, T. Müller, H. Herrmann, and F. Stratmann, 2020b: Characterization of aerosol particles at Cabo Verde close to sea level and at the cloud level–Part 1: Particle number size distribution, cloud condensation nuclei and their origins. *Atmos. Chem. Phys.*, **20**, doi:10.5194/acp-20-1431-2020.

Gordon, H., J. Kirkby, U. Baltensperger, F. Bianchi, M. Breitenlechner, J. Curtius, A. Dias, J. Dommen, N. M. Donahue, E. M. Dunne, J. Duplissy, S. Ehrhart, R. C. Flagan, C. Frege, C. Fuchs, A. Hansel, C. R. Hoyle, M. Kulmala, A. Kürten, K. Lehtipalo, V. Makhmutov, U. Molteni, M. P. Rissanen, Y. Stozkhov, J. Tröstl, G. Tsagkogeorgas, R. Wagner, C. Williamson, D. Wimmer, P. M. Winkler, C. Yan, and K. S. Carslaw, 2017: Causes and importance of new particle formation in the present-day and preindustrial atmospheres. *J. Geophys. Res.: Atmos.*, **122**, 8739–8760, doi:10.1002/2017JD026844.

Gras, J. L. and M. Keywood, 2017: Cloud condensation nuclei over the southern ocean: wind dependence and seasonal cycles. *Atmos. Chem. Phys.*, **17**, 4419–4432, doi:10.5194/acp-17-4419-2017.

Grawe, S., 2019: *Coal fly ash: How sample properties and methodology influence immersion freezing results*. Ph.D. thesis, University of Leipzig.

Gysel, M. and F. Stratmann, 2014: WP3-NA3: In-situ chemical, physical and optical properties of aerosols, Deliverable D3.11: Standardized protocol for CCN measurements.
URL    http://www.actris.net/Portals/97/Publications/quality%20standards/aerosol%20insitu/WP3_D3.13_M24_CCNC_SOP_v130514.pdf

Hamilton, D. S., L. A. Lee, K. J. Pringle, C. L. Reddington, D. V. Spracklen, and K. S. Carslaw, 2014: Occurrence of pristine aerosol environments on a polluted planet. *Proc. Nat. Acad. Sci. USA*, **111**, 18466–18471, doi:10.1073/pnas.1415440111.

Hartmann, M., T. Blunier, S. Brügger, J. Schmale, M. Schwikowski, A. Vogel, H. Wex, and F. Stratmann, 2019: Variation of Ice Nucleating Particles in the European Arctic Over the Last Centuries. *Geophys. Res. Lett.*, **46**, 4007–4016, doi:10.1029/2019GL082311.

Hartmann, M., X. Gong, S. Kecorius, M. van Pinxteren, T. Vogl, A. Welti, H. Wex, S. Zeppenfeld, H. Herrmann, A. Wiedensohler, and F. Stratmann, 2021: Terrestrial or marine – indications towards the origin of ice-nucleating particles during melt season in the European Arctic up to 83.7° N. *Atmos. Chem. Phys.*, **21**, 11613–11636, doi:10.5194/acp-21-11613-2021.

Haywood, J. and O. Boucher, 2000: Estimates of the direct and indirect radiative forcing due to tropospheric aerosols: A review. *Rev. Geophys.*, **38**, 513–543, doi:10.1029/1999RG000078.

Herenz, P., H. Wex, S. Henning, T. B. Kristensen, F. Rubach, A. Roth, S. Borrmann, H. Bozem, H. Schulz, and F. Stratmann, 2018: Measurements of aerosol and CCN properties in the Mackenzie River delta (Canadian Arctic) during spring–summer transition in May 2014. *Atmos. Chem. Phys.*, **18**, 4477–4496, doi:10.5194/acp-18-4477-2018.

Herenz, P., H. Wex, A. Mangold, Q. Laffineur, I. V. Gorodetskaya, Z. L. Fleming, M. Panagi, and F. Stratmann, 2019: CCN measurements at the Princess Elisabeth Antarctica research station during three austral summers. *Atmos. Chem. Phys.*, **19**, 275–294, doi:10.5194/acp-19-275-2019.

Hinds, W., 1999: *Aerosol Technology: Properties, Behavior, and Measurement of Airborne Particles*. Wiley.

Hoose, C. and O. Möhler, 2012: Heterogeneous ice nucleation on atmospheric aerosols: a review of results from laboratory experiments. *Atmos. Chem. Phys.*, **12**, 9817–9854, doi:10.5194/acp-12-9817-2012.

Hoppel, W. and G. Frick, 1990: Submicron aerosol size distributions measured over the tropical and South Pacific. *Atmos. Env. A*, **24**, 645–659, doi:10.1016/0960-1686(90)90020-N.

Hoppel, W., G. Frick, and R. Larson, 1986: Effect of nonprecipitating clouds on the aerosol size distribution in the marine boundary layer. *Geophys. Res. Lett.*, **13**, 125–128, doi:10.1029/GL013i002p00125.

Humphries, R. S., M. D. Keywood, S. Gribben, I. M. McRobert, J. P. Ward, P. Selleck, S. Taylor, J. Harnwell, C. Flynn, G. R. Kulkarni, et al., 2021: Southern Ocean latitudinal gradients of Cloud Condensation Nuclei. *Atmos. Chem. Phys.*, **21**, 12757—-12782, doi:10.5194/acp-21-12757-2021.

Humphries, R. S., A. R. Klekociuk, R. Schofield, M. Keywood, J. Ward, and S. R. Wilson, 2016: Unexpectedly high ultrafine aerosol concentrations above east antarctic sea ice. *Atmos. Chem. Phys.*, **16**, 2185–2206, doi:10.5194/acp-16-2185-2016.

Hunter, J. D., 2007: Matplotlib: A 2D graphics environment. *Comp. Sci. Eng.*, **9**, 90–95, doi:10.1109/MCSE.2007.55.

IPCC, 2021: *Climate Change 2021: The Physical Science Basis. Contribution of Working Group I to the Sixth Assessment Report of the Intergovernmental Panel on Climate Change*. Cambridge University Press, Cambridge, United Kingdom and New York, NY, USA, In press.

Kanji, Z. A., L. A. Ladino, H. Wex, Y. Boose, M. Burkert-Kohn, D. J. Cziczo, and M. Krämer, 2017: Overview of ice nucleating particles. *Meteor. Monogr.*, **58**, 1–1, doi:10.1175/AMSMONOGRAPHS-D-16-0006.1.

Khlystov, A., C. Stanier, and S. N. Pandis, 2004: An Algorithm for Combining Electrical Mobility and Aerodynamic Size Distributions Data when Measuring Ambient Aerosol Special Issue of Aerosol Science and Technology on Findings from the Fine Particulate Matter Supersites Program. *Aerosol Sci. Tech.*, **38**, 229–238, doi:10.1080/02786820390229543.

Köhler, H., 1936: The nucleus in and the growth of hygroscopic droplets. *Trans. Faraday Soc.*, **32**, 1152–1161, doi:10.1039/TF9363201152.

Kulmala, M., L. Pirjola, and J. M. Mäkelä, 2000: Stable sulphate clusters as a source of new atmospheric particles. *Nature*, **404**, 66–69, doi:10.1038/35003550.

Landwehr, S., I. Thurnherr, N. Cassar, M. Gysel-Beer, and J. Schmale, 2020: Using global reanalysis data to quantify and correct airflow distortion bias in shipborne wind speed measurements. *Atmos. Meas. Tech.*, **13**, 3487–3506, doi:10.5194/amt-13-3487-2020.

Landwehr, S., M. Volpi, F. A. Haumann, C. M. Robinson, I. Thurnherr, V. Ferracci, A. Baccarini, J. Thomas, I. Gorodetskaya, C. Tatzelt, S. Henning, R. L. Modini, H. J. Forrer, Y. Lin, N. Cassar, R. Simó, C. Hassler, A. Moallemi, S. E. Fawcett, N. Harris, R. Airs, M. H. Derkani, A. Alberello, A. Toffoli, G. Chen, P. Rodríguez-Ros, M. Zamanillo, P. Cortés-Greus, L. Xue, C. G. Bolas, K. C. Leonard, F. Perez-Cruz, D. Walton, and J. Schmale, 2021: Exploring the coupled ocean and atmosphere system with a data science approach applied to observations from the Antarctic Circumnavigation Expedition. *Earth Syst. Dynam.*, **12**, 1295–1369, doi:10.5194/esd-12-1295-2021.

Legrand, M. and E. C. Pasteur, 1998: Methane sulfonic acid to non-sea-salt sulfate ratio in coastal antarctic aerosol and surface snow. *J. Geophys. Res.: Atmos.*, **103**, 10991–11006, doi:10.1029/98JD00929.

Lindzen, R. S., 1990: Some coolness concerning global warming. *Bull. Amer. Meteor. Soc.*, **71**, 288–299.
URL http://www.jstor.org/stable/26227522

Mace, G. G. and A. Protat, 2018: Clouds over the southern ocean as observed from the r/v investigator during capricorn. part i: Cloud occurrence and phase partitioning. *J. Appl. Meteor. Climatol.*, **57**, 1783–1803, doi:10.1175/JAMC-D-17-0194.1.

McCluskey, C., T. Hill, R. Humphries, A. Rauker, S. Moreau, P. Strutton, S. Chambers, A. Williams, I. McRobert, J. Ward, et al., 2018a: Observations of ice nucleating particles over southern ocean waters. *Geophys. Res. Lett.*, **45**, 11–989, doi:10.1029/2018GL079981.

McCluskey, C. S., J. Ovadnevaite, M. Rinaldi, J. Atkinson, F. Belosi, D. Ceburnis, S. Marullo, T. C. J. Hill, U. Lohmann, Z. A. Kanji, C. O'Dowd, S. M. Kreidenweis, and P. J. De-Mott, 2018b: Marine and terrestrial organic ice-nucleating particles in pristine marine to continentally influenced northeast atlantic air masses. *J. Geophys. Res.: Atmos.*, **123**, 6196–6212, doi:10.1029/2017JD028033.

McCoy, I. L., C. S. Bretherton, R. Wood, C. H. Twohy, A. Gettelman, C. G. Bardeen, and D. W. Toohey, 2021: Influences of recent particle formation on southern ocean aerosol variability and low cloud properties. *J. Geophys. Res.: Atmos.*, **126**, doi:10.1029/2020JD033529.

McFarquhar, G. M., C. Bretherton, R. Marchand, A. Protat, P. J. DeMott, S. P. Alexander, G. C. Roberts, C. H. Twohy, D. Toohey, S. Siems, Y. Huang, R. Wood, R. M. Rauber, S. Lasher-Trapp, J. Jensen, J. Stith, J. Mace, J. Um, E. J?rvinen, M. Schnaiter, A. Gettelman, K. J. Sanchez, C. S. McCluskey, L. M. Russell, I. L. McCoy, R. Atlas, C. G. Bardeen, K. A. Moore, T. C. J. Hill, R. S. Humphries, M. D. Keywood, Z. Ristovski, L. Cravigan, R. Schofield, C. Fairall, M. D. Mallet, S. M. Kreidenweis, B. Rainwater, J. D?Alessandro, Y. Wang, W. Wu, G. Saliba, E. J. T. Levin, S. Ding, F. Lang, S. C. Truong, C. Wolff, J. Haggerty, M. J. Harvey, A. Klekociuk, and A. McDonald, 2020: Observations of clouds, aerosols, precipitation, and surface radiation over the Southern Ocean: An overview of CAPRICORN, MARCUS, MICRE and SOCRATES. *Bull. Amer. Meteor. Soc.*, 1–92, doi:10.1175/BAMS-D-20-0132.1.

McFiggans, G., P. Artaxo, U. Baltensperger, H. Coe, M. C. Facchini, G. Feingold, S. Fuzzi, M. Gysel, A. Laaksonen, U. Lohmann, et al., 2006: The effect of physical and chemical aerosol properties on warm cloud droplet activation. *Atmos. Chem. Phys.*, **6**, 2593–2649, doi:10.5194/acp-6-2593-2006.

Minikin, A., M. Legrand, J. Hall, D. Wagenbach, C. Kleefeld, E. Wolff, E. C. Pasteur, and F. Ducroz, 1998: Sulfur-containing species (sulfate and methanesulfonate) in coastal Antarctic aerosol and precipitation. *J. Geophys. Res.: Atmos.*, **103**, 10975–10990, doi:10.1029/98JD00249.

Mitts, B. A., X. Wang, D. D. Lucero, C. M. Beall, G. B. Deane, P. J. DeMott, and K. A. Prather, 2021: Importance of Supermicron Ice Nucleating Particles in Nascent Sea Spray. *Geophys. Res. Lett.*, **48**, doi:10.1029/2020GL089633.

Moallemi, A., S. Landwehr, C. Robinson, R. Simó, M. Zamanillo, G. Chen, A. Baccarini, M. Schnaiter, S. Henning, R. L. Modini, M. Gysel-Beer, and J. Schmale, 2021: Sources, Occurrence and Characteristics of Fluorescent Biological Aerosol Particles Measured Over the Pristine Southern Ocean. *J. Geophys. Res.: Atmos.*, **126**, doi:10.1029/2021JD034811.

Modini, R. L., A. A. Frossard, L. Ahlm, L. M. Russell, C. E. Corrigan, G. C. Roberts, L. N. Hawkins, J. C. Schroder, A. K. Bertram, R. Zhao, A. K. Y. Lee, J. P. D. Abbatt, J. Lin, A. Nenes, Z. Wang, A. Wonaschütz, A. Sorooshian, K. J. Noone, H. Jonsson, J. H. Seinfeld, D. Toom-Sauntry, A. M. Macdonald, and W. R. Leaitch, 2015: Primary marine aerosol-cloud interactions off the coast of California. *J. Geophys. Res.: Atmos.*, **120**, 4282–4303, doi:10.1002/2014JD022963.

Mossop, S. and N. Thorndike, 1966: The use of membrane filters in measurements of ice nucleus concentration. i. effect of sampled air volume. *J. Appl. Meteor.*, **5**, 474–480, doi:10.1175/1520-0450(1966)005<0474:TUOMFI>2.0.CO;2.

Müller, K., S. Lehmann, D. v. Pinxteren, T. Gnauk, N. Niedermeier, A. Wiedensohler, and H. Herrmann, 2010: Particle characterization at the cape verde atmospheric observatory during the 2007 RHaMBLe intensive. *Atmos. Chem. Phys.*, **10**, 2709–2721, doi:10.5194/acp-10-2709-2010.

Murray, B. J., S. Broadley, T. Wilson, J. Atkinson, and R. Wills, 2011: Heterogeneous freezing of water droplets containing kaolinite particles. *Atmos. Chem. Phys.*, **11**, 4191–4207, doi:10.5194/acp-11-4191-2011.

Murray, B. J., K. S. Carslaw, and P. R. Field, 2021: Opinion: Cloud-phase climate feedback and the importance of ice-nucleating particles. *Atmos. Chem. Phys.*, **21**, 665–679, doi:10.5194/acp-21-665-2021.

Murray, B. J., D. O'Sullivan, J. D. Atkinson, and M. E. Webb, 2012: Ice nucleation by particles immersed in supercooled cloud droplets. *Chem. Soc. Rev.*, **41**, 6519–6554, doi:10.1039/C2CS35200A.

O'Dowd, C. D., K. Hämeri, J. Mäkelä, M. Väkeva, P. Aalto, G. de Leeuw, G. J. Kunz, E. Becker, H.-C. Hansson, A. G. Allen, et al., 2002: Coastal new particle formation: Environmental conditions and aerosol physicochemical characteristics during nucleation bursts. *J. Geophys. Res.: Atmos.*, **107**, PAR–12, doi:10.1029/2000JD000206.

O'Dowd, C. D., J. A. Lowe, M. H. Smith, B. Davison, C. N. Hewitt, and R. M. Harrison, 1997: Biogenic sulphur emissions and inferred non-sea-salt-sulphate cloud condensation nuclei in and around antarctica. *J. Geophys. Res.: Atmos.*, **102**, 12839–12854, doi:10.1029/96JD02749.

O'Shea, S. J., T. W. Choularton, M. Flynn, K. N. Bower, M. Gallagher, J. Crosier, P. Williams, I. Crawford, Z. L. Fleming, C. Listowski, et al., 2017: In situ measurements of cloud microphysics and aerosol over coastal antarctica during the mac campaign. *Atmos. Chem. Phys.*, **17**, 13049–13070, doi:10.5194/acp-17-13049-2017.

Pérez, F. and B. E. Granger, 2007: Ipython: a system for interactive scientific computing. *Comp. Sci. Eng.*, **9**, 21–29, doi:10.1109/MCSE.2007.53.

Petters, M. and S. Kreidenweis, 2007: A single parameter representation of hygroscopic growth and cloud condensation nucleus activity. *Atmos. Chem. Phys.*, **7**, 1961–1971, doi:10.5194/acp-7-1961-2007.

Piel, C., R. Weller, M. Huke, and D. Wagenbach, 2006: Atmospheric methane sulfonate and non-sea-salt sulfate records at the european project for ice coring in antarctica (epica) deep-drilling site in dronning maud land, antarctica. *J. Geophys. Res.: Atmos.*, **111**, doi:10.1029/2005JD006213.

Polen, M., T. Brubaker, J. Somers, and R. C. Sullivan, 2018: Cleaning up our water: reducing interferences from nonhomogeneous freezing of "pure" water in droplet freezing assays of ice-nucleating particles. *Atmos. Meas. Tech.*, **11**, 5315–5334, doi:10.5194/amt-11-5315-2018.

Prenni, A. J., J. Y. Harrington, M. Tjernström, P. J. DeMott, A. Avramov, C. N. Long, S. M. Kreidenweis, P. Q. Olsson, and J. Verlinde, 2007: Can ice-nucleating aerosols affect Arctic seasonal climate? *Bull. Amer. Meteor. Soc.*, **88**, 541–550, doi:10.1175/BAMS-88-4-541.

Pringle, K., H. Tost, A. Pozzer, U. Pöschl, and J. Lelieveld, 2010: Global distribution of the effective aerosol hygroscopicity parameter for ccn activation. *Atmos. Chem. Phys.*, **10**, 5241–5255, doi:10.5194/acp-10-5241-2010.

Protat, A., E. Schulz, L. Rikus, Z. Sun, Y. Xiao, and M. Keywood, 2017: Shipborne observations of the radiative effect of southern ocean clouds. *J. Geophys. Res.: Atmos.*, **122**, 318–328, doi:10.1002/2016JD026061.

Pruppacher, H. and J. Klett, 1997: *Microphysics of Clouds and Precipitation*. Kluwer Acad., Norwell, Mass., USA.

Quinn, P., D. Coffman, J. Johnson, L. Upchurch, and T. Bates, 2017: Small fraction of marine cloud condensation nuclei made up of sea spray aerosol. *Nature Geosci.*, **10**, 674, doi:10.1038/NGEO3003.

Quinn, P. K., D. J. Coffman, V. N. Kapustin, T. S. Bates, and D. S. Covert, 1998: Aerosol optical properties in the marine boundary layer during the First Aerosol Characterization Experiment (ACE 1) and the underlying chemical and physical aerosol properties. *J. Geophys. Res.: Atmos.*, **103**, 16547–16563, doi:10.1029/97JD02345.

Radenz, M., P. Seifert, H. Baars, A. A. Floutsi, Z. Yin, and J. Bühl, 2021: Automated time–height-resolved air mass source attribution for profiling remote sensing applications. *Atmos. Chem. Phys.*, **21**, 3015–3033, doi:10.5194/acp-21-3015-2021.

Raes, F., 1995: Entrainment of free tropospheric aerosols as a regulating mechanism for cloud condensation nuclei in the remote marine boundary layer. *J. Geophys. Res.: Atmos.*, **100**, 2893–2903, doi:10.1029/94JD02832.

Regayre, L. A., J. Schmale, J. S. Johnson, C. Tatzelt, A. Baccarini, S. Henning, M. Yoshioka, F. Stratmann, M. Gysel-Beer, D. P. Grosvenor, and K. S. Carslaw, 2020: The value of remote marine aerosol measurements for constraining radiative forcing uncertainty. *Atmos. Chem. Phys.*, **20**, 10063–10072, doi:10.5194/acp-20-10063-2020.

Riipinen, I., T. Yli-Juuti, J. R. Pierce, T. Petäjä, D. R. Worsnop, M. Kulmala, and N. M. Donahue, 2012: The contribution of organics to atmospheric nanoparticle growth. *Nature Geosci.*, **5**, 453–458, doi:10.1038/ngeo1499.

Roberts, G. and A. Nenes, 2005: A continuous-flow streamwise thermal-gradient ccn chamber for atmospheric measurements. *Aerosol Sci. Tech.*, **39**, 206–221, doi:10.1080/027868290913988.

Rodriguez-Ros, P., M. Galí, P. Cortés, C. M. Robinson, D. Antoine, C. Wohl, M. Yang, and R. Simo, 2020: Remote sensing retrieval of isoprene concentrations in the Southern Ocean. *Earth and Space Science Open Archive*, doi:10.1002/essoar.10502496.1.

Rosenfeld, D. and W. L. Woodley, 2000: Deep convective clouds with sustained supercooled liquid water down to -37.5°c. *Nature*, **405**, 440–442, doi:10.1038/35013030.

Sanchez, K. J., G. C. Roberts, G. Saliba, L. M. Russell, C. Twohy, J. M. Reeves, R. S. Humphries, M. D. Keywood, J. P. Ward, and I. M. McRobert, 2021: Measurement report: Cloud processes and the transport of biological emissions affect southern ocean particle and cloud condensation nuclei concentrations. *Atmos. Chem. Phys.*, **21**, 3427–3446, doi:10.5194/acp-21-3427-2021.

Sanchez-Marroquin, A., O. Arnalds, K. Baustian-Dorsi, P. Dagsson-Waldhauserova, A. Harrison, E. C. Maters, K. Pringle, J. Vergara-Temprado, I. Burke, J. McQuaid, et al., 2020: Iceland is an episodic source of atmospheric ice-nucleating particles relevant for mixed-phase clouds. *Sci. Adv.*, **6**, eaba8137, doi:10.1126/sciadv.aba8137.

Savoie, D. L. and J. M. Prospero, 1989: Comparison of oceanic and continental sources of non-sea-salt sulphate over the Pacific Ocean. *Nature*, **339**, 685–687, doi:10.1038/339685a0.

Schmale, J., A. Baccarini, I. Thurnherr, S. Henning, A. Efraim, L. Regayre, C. Bolas, M. Hartmann, A. Welti, K. Lehtipalo, F. Aemisegger, C. Tatzelt, S. Landwehr, R. L. Modini, F. Tummon, J. Johnson, N. Harris, M. Schnaiter, A. Toffoli, M. Derkani, N. Bukowiecki, F. Stratmann, J. Dommen, U. Baltensperger, H. Wernli, D. Rosenfeld, M. Gysel-Beer, and K. Carslaw, 2019: Overview of the Antarctic Circumnavigation Expedition: Study of Preindustrial-like Aerosols and Their Climate Effects (ACE-SPACE). *Bull. Amer. Meteor. Soc.*, **0**, null, doi:10.1175/BAMS-D-18-0187.1.

Schmale, J., S. Henning, B. Henzing, H. Keskinen, K. Sellegri, J. Ovadnevaite, A. Bougiatioti, N. Kalivitis, I. Stavroulas, A. Jefferson, et al., 2017: Collocated observations of cloud condensation nuclei, particle size distributions, and chemical composition. *Sci. Data*, **4**, 170003, doi:10.1038/sdata.2017.3.

Schmale, J., J. Schneider, E. Nemitz, Y. S. Tang, U. Dragosits, T. D. Blackall, P. N. Trathan, G. J. Phillips, M. Sutton, and C. F. Braban, 2013: Sub-antarctic marine aerosol: dominant contributions from biogenic sources. *Atmos. Chem. Phys.*, **13**, 8669–8694, doi:10.5194/acp-13-8669-2013.

Seinfeld, J. H. and S. N. Pandis, 2006: *Atmospheric Chemistry and Physics: From Air Pollution to Climate Change*. John Wiley & Sons, New York, NY, USA.

Sorooshian, A., M.-L. Lu, F. J. Brechtel, H. Jonsson, G. Feingold, R. C. Flagan, and J. H. Seinfeld, 2007: On the source of organic acid aerosol layers above clouds. *Env. Sci. Tech.*, **41**, 4647–4654, doi:10.1021/es0630442.

Sprenger, M. and H. Wernli, 2015: The LAGRANTO Lagrangian analysis tool – version 2.0. *Geosci. Model Dev.*, **8**, 2569–2586, doi:10.5194/gmd-8-2569-2015.

Thurnherr, I., H. Wernli, and F. Aemisegger, 2020: [Dataset] 10-day backward trajectories from ECMWF analysis data along the ship track of the Antarctic Circumnavigation Expedition in austral summer 2016/2017. *Zenodo*, doi:10.5281/zenodo.4031705, version 1.0.

Tobo, Y., A. J. Prenni, P. J. DeMott, J. A. Huffman, C. S. McCluskey, G. Tian, C. Pöhlker, U. Pöschl, and S. M. Kreidenweis, 2013: Biological aerosol particles as a key determinant of ice nuclei populations in a forest ecosystem. *J. Geophys. Res.: Atmos.*, **118**, 10100–10110, doi:10.1002/jgrd.50801.

Tomasi, C. and A. Lupi, 2016: Primary and Secondary Sources of Atmospheric Aerosol. *Atmospheric Aerosols: Life Cycles and Effects on Air Quality and Climate*, Wiley Online Library, chapter 1, 1–86.

Turner, S. M., M. J. Harvey, C. S. Law, P. D. Nightingale, and P. S. Liss, 2004: Iron-induced changes in oceanic sulfur biogeochemistry. *Geophys. Res. Lett.*, **31**, doi:10.1029/2004GL020296.

Twomey, S., 1974: Pollution and the planetary albedo. *Atmos. Environ.*, **8**, 1251–1256, doi:10.1016/0004-6981(74)90004-3.

Uetake, J., T. C. Hill, K. A. Moore, P. J. DeMott, A. Protat, and S. M. Kreidenweis, 2020: Airborne bacteria confirm the pristine nature of the southern ocean boundary layer. *Proc. Nat. Acad. Sci. USA*, doi:10.1073/pnas.2000134117.

Vali, G., 1971: Quantitative evaluation of experimental results an the heterogeneous freezing nucleation of supercooled liquids. *J. Atmos. Sci.*, **28**, 402–409, doi:10.1175/1520-0469(1971)028<0402:QEOERA>2.0.CO;2.

van Pinxteren, M., S. Barthel, K. W. Fomba, K. Müller, W. Von Tümpling, and H. Herrmann, 2017: The influence of environmental drivers on the enrichment of organic carbon in the sea surface microlayer and in submicron aerosol particles–measurements from the atlantic ocean. *Elementa: Science of the Anthropocene*, **5**, 35, doi:10.1525/elementa.225.

Vergara-Temprado, J., A. K. Miltenberger, K. Furtado, D. P. Grosvenor, B. J. Shipway, A. A. Hill, J. M. Wilkinson, P. R. Field, B. J. Murray, and K. S. Carslaw, 2018: Strong control of southern ocean cloud reflectivity by ice-nucleating particles. *Proc. Nat. Acad. Sci. USA*, **115**, 2687–2692, doi:10.1073/pnas.1721627115.

Walton, D. and J. Thomas, 2018: Cruise Report - Antarctic Circumnavigation Expedition (ACE) 20th December 2016 - 19th March 2017.

Weingartner, E., S. Nyeki, and U. Baltensperger, 1999: Seasonal and diurnal variation of aerosol size distributions (10< D< 750 nm) at a high-alpine site (Jungfraujoch 3580 m asl). *J. Geophys. Res.: Atmos.*, **104**, 26809–26820, doi:10.1029/1999JD900170.

Welti, A., E. K. Bigg, P. J. DeMott, X. Gong, M. Hartmann, M. Harvey, S. Henning, P. Herenz, T. C. J. Hill, B. Hornblow, C. Leck, M. Löffler, C. S. McCluskey, A. M. Rauker, J. Schmale, C. Tatzelt, M. van Pinxteren, and F. Stratmann, 2020: Ship-based measurements of ice nuclei concentrations over the Arctic, Atlantic, Pacific and Southern oceans. *Atmos. Chem. Phys.*, **20**, 15191–15206, doi:10.5194/acp-20-15191-2020.

Welti, A., K. Müller, Z. L. Fleming, and F. Stratmann, 2018: Concentration and variability of ice nuclei in the subtropical maritime boundary layer. *Atmos. Chem. Phys.*, **18**, 5307–5320, doi:10.5194/acp-18-5307-2018.

Wex, H., L. Huang, W. Zhang, H. Hung, R. Traversi, S. Becagli, R. J. Sheesley, C. E. Moffett, T. E. Barrett, R. Bossi, et al., 2019: Annual variability of ice-nucleating particle concentrations at different arctic locations. *Atmos. Chem. Phys.*, **19**, 5293–5311, doi:10.5194/acp-19-5293-2019.

Wex, H., C. Jentsch, S. Mertes, E. Freney, and F. Stratmann, 2020: Varitations in off-line filter sampling and analysis of Ice Nucleating Particle measurements. *European Aerosol Conference*, Aachen, Germany.

Wiedensohler, A., W. Birmili, A. Nowak, A. Sonntag, K. Weinhold, M. Merkel, B. Wehner, T. Tuch, S. Pfeifer, M. Fiebig, A. M. Fjäraa, E. Asmi, K. Sellegri, R. Depuy, H. Venzac, P. Villani, P. Laj, P. Aalto, J. A. Ogren, E. Swietlicki, P. Williams, P. Roldin, P. Quincey, C. Hüglin, R. Fierz-Schmidhauser, M. Gysel, E. Weingartner, F. Riccobono, S. Santos, C. Grüning, K. Faloon, D. Beddows, R. Harrison, C. Monahan, S. G. Jennings, C. D. O'Dowd, A. Marinoni, H.-G. Horn, L. Keck, J. Jiang, J. Scheckman, P. H. McMurry, Z. Deng, C. S. Zhao, M. Moerman, B. Henzing, G. de Leeuw, G. Löschau, and S. Bastian, 2012: Mobility particle size spectrometers: harmonization of technical standards and data structure to facilitate high quality long-term observations of atmospheric particle number size distributions. *Atmos. Meas. Tech.*, **5**, 657–685, doi:10.5194/amt-5-657-2012.

Wilson, J. C. and B. Y. Liu, 1980: Aerodynamic particle size measurement by laser-doppler velocimetry. *J. Aerosol Sci.*, **11**, 139–150, doi:10.1016/0021-8502(80)90030-0.

Yan, J., J. Jung, Q. Lin, M. Zhang, S. Xu, and S. Zhao, 2020a: Effect of sea ice retreat on marine aerosol emissions in the southern ocean, antarctica. *Sci. Tot. Env.*, **745**, 140773, doi:10.1016/j.scitotenv.2020.140773.

Yan, J., J. Jung, M. Zhang, F. Bianchi, Y. J. Tham, S. Xu, Q. Lin, S. Zhao, L. Li, and L. Chen, 2020b: Uptake selectivity of methanesulfonic acid (msa) on fine particles over polynya regions of the ross sea, antarctica. *Atmos. Chem. Phys.*, **20**, 3259–3271, doi:10.5194/acp-20-3259-2020.

Yan, J., M. Zhang, J. Jung, Q. Lin, S. Zhao, S. Xu, and L. Chen, 2020c: Influence on the conversion of DMS to MSA and Sulphate in the Southern Ocean, Antarctica. *Atmos. Env.*, **233**, 117611, doi:10.1016/j.atmosenv.2020.117611.

Young, T., 1805: III. An essay on the cohesion of fluids. *Philos. Trans. Roy. Soc. London*, 65–87.

Zobrist, B., T. Koop, B. Luo, C. Marcolli, and T. Peter, 2007: Heterogeneous ice nucleation rate coefficient of water droplets coated by a nonadecanol monolayer. *J. Phys. Chem. C*, **111**, 2149–2155, doi:10.1021/jp066080w.

# List of publications

## First author publications (part of this thesis)

**Tatzelt, C.**, Henning, S., Welti, A., Baccarini, A., Hartmann, M., Gysel-Beer, M., van Pinxteren, M., Modini, R. L., Schmale, J., and Stratmann, F.: Circum-Antarctic abundance and properties of CCN and INP, *Atmos. Chem. Phys. Discuss.* [preprint], doi:10.5194/acp-2021-700, in review (accepted 14 June 2022), 2021.

In this study, I performed the CCN and INP analysis, data evaluation, visualisation, and interpretation as well as the writing of the manuscript. Silvia Henning and Frank Stratmann were involved in the discussion, interpretation, and writing of the manuscript. Martin Gysel-Beer and Frank Stratmann provided the in situ instrumentation. Silvia Henning, André Welti, Andrea Baccarini, Julia Schmale, and Markus Hartmann performed the measurements during the cruise itself. Manuela van Pinxteren provided the analysis of sodium and MSA of the filter samples and interpretation of said analysis. Robin L. Modini provided the mode-fitted size distributions. All authors proofread the final version of the manuscript.

## Co-author publications (not part of this thesis)

Schmale, J., Baccarini, A., Thurnherr, I., Henning, S., Efraim, A., Regayre, L., Bolas, C., Hartmann, M., Welti, A., Lehtipalo, K., Aemisegger, F., **Tatzelt, C.**, Landwehr, S., Modini, R. L., Tummon, F., Johnson, J. S., Harris, N., Schnaiter, M., Toffoli, A., Derkani, M., Bukowiecki, N., Stratmann, F., Dommen, J., Baltensperger, U., Wernli, H., Rosenfeld, D., Gysel-Beer, M., and Carslaw, K. S.: Overview of the Antarctic Circumnavigation Expedition: Study of Preindustrial-like Aerosols and Their Climate Effects (ACE-SPACE), *Bull. Amer. Meteor. Soc.*, **100(11)**, 2260–2283, doi:10.1175/BAMS-D-18-0187.1, 2019.

In this study, I provided the CCN and INP data. I helped preparing the paper and provided feedback on the draft.

---

Regayre, L. A., Schmale, J., Johnson, J. S., **Tatzelt, C.**, Baccarini, A., Henning, S., Yoshioka, M., Stratmann, F., Gysel-Beer, M., Grosvenor, D. P., and Carslaw, K. S.: The value of remote marine aerosol measurements for constraining radiative forcing uncertainty, *Atmos. Chem. Phys.*, **20**, 10063–10072, doi:10.5194/acp-20-10063-2020, 2020.

In this study, I provided the CCN data for ACE. I helped preparing the paper and provided feedback on the draft.

---

Welti, A., Bigg, E. K., DeMott, P. J., Gong, X., Hartmann, M., Harvey, M., Henning, S., Herenz, P., Hill, T. C. J., Hornblow, B., Leck, C., Löffler, M., McCluskey, C. S., Rauker, A. M., Schmale, J., **Tatzelt, C.**, van Pinxteren, M., and Stratmann, F.: Ship-based measurements of

ice nuclei concentrations over the Arctic, Atlantic, Pacific and Southern oceans, *Atmos. Chem. Phys.*, **20**, 15191—15206, doi:10.5194/acp-20-15191-2020, 2020.

In this study, I provided the INP data for ACE. I helped preparing the paper and provided feedback on the draft.

___

Landwehr, S., Volpi, M., Haumann, F. A., Robinson, C. M., Thurnherr, I., Ferracci, V., Baccarini, A., Thomas, J., Gorodetskaya, I., **Tatzelt, C.**, Henning, S., Modini, R. L., Forrer, H. J., Lin, Y., Cassar, N., Simó, R., Hassler, C., Moallemi, A., Fawcett, S. E., Harris, N., Airs, R., Derkani, M. H., Alberello, A., Toffoli, A., Chen, G., Rodríguez-Ros, P., Zamanillo, M., Cortés-Greus, P., Xue, L., Bolas, C. G., Leonard, K. C., Perez-Cruz, F., Walton, D., and Schmale, J.: Exploring the coupled ocean and atmosphere system with a data science approach applied to observations from the Antarctic Circumnavigation Expedition, *Earth Syst. Dynam.*, **12**, 1295–1369, doi:10.5194/esd-12-1295-2021, 2021.

For this study, I provided the CCN and INP data for ACE, as well as data on the ionic composition. I wrote section A3.1 (LV5-Distance to land) and helped proofread the manuscript.

# PhD commission

**Prof. Dr. Hartmut Herrmann (chair)**
Department Chemistry of the Atmosphere,
Leibniz Institute for Tropospheric Research, Leipzig, Germany
hartmut.herrmann@tropos.de

**Prof. Dr. Johannes Quaas**
Institute for Meteorology, University of Leipzig, Leipzig, Germany
johannes.quaas@uni-leipzig.de

**JP Dr. Heike Kalesse-Los (supervisor)**
Institute for Meteorology, University of Leipzig, Leipzig, Germany
heike.kalesse@uni-leipzig.de

# Supervision commission

**Dr. Frank Stratmann**
Department Experimental Aerosol and Cloud Microphysics,
Leibniz Institute for Tropospheric Research, Leipzig, Germany
frank.stratmann@tropos.de

**Dr. Silvia Henning**
Department Experimental Aerosol and Cloud Microphysics,
Leibniz Institute for Tropospheric Research, Leipzig, Germany
silvia.henning@tropos.de

**Dr. Manuela van Pinxeren**
Department Chemistry of the Atmosphere,
Leibniz Institute for Tropospheric Research, Leipzig, Germany
manuela.vanpixteren@tropos.de

# Acknowledgements

To Frank and Silvia: Thank you for your supervision, guidance, and support. I am glad you believed in me and helped me grow, on a professional and personal level.

To Prof. Herrmann, Prof. Quaas, and JP Kalesse-Los: Thank you for your technical and strategic guidance as part of my doctoral committee.

To my co-authors: Thank you for all your hard work and the insights you provide me into your respective field of expertise.

To all participants of ACE: thank you for all your efforts in gathering data from the Southern Ocean. Especially thank you to all of you that I was lucky to meet, for sharing your impressions and experiences. A special thank you to all partners within ACE-SPACE, in particular our PI Julia Schmale who went the extra mile in every regard.

To the members of the cloud group: Thank you for the warm welcome into the world of cloud microphysics and all the countless (off-)topical discussions in the chestnut cove. Thank you Sarah, Xianda, and Silvio for providing the nicest office experience. Thank you Mareike, Markus, and André for their work during ACE and the stories they shared. Further, thank you to everyone in the ice-lab, especially Jasmin, Olivia, and Riccarda for helping with the INP analysis. Thank you Oliver for helping with the correlation analyses.

To all fellow PhD students at TROPOS and LIM: Thank you for the enlightening PhD seminars and extra-institutional activities. Especially Roxana, Teresa, and Diego for all the sunny coffee breaks. Further, I am grateful for the insightful, extra-topical meetings with fellow PhD students at UFZ, organised by *do-it*.

To the environmental action group at TROPOS: Thank you for the fruitful brainstorming sessions and meetings. We kicked off quite something there in the wake of F4F.

Ich möchte mich auch ganz herzlich bei meiner Familie bedanken, vor allem für die Liebe, Unterstützung und das immer-ein-offenes-Ohr-Haben.

To Augusta again: Thank you for everything.

# Colophon

This document was created using LaTeX via Overleaf.

All data processing was performed using *Python* (version 2.7.14) on *Ipython* (version 5.4.1; Pérez and Granger, 2007).

All scientific figures were created using *Matplotlib* (Hunter, 2007). Additional figures were created using GIMP.

Where possible, colourblind-safe colour maps from ColorBrewer (version 2.0) were used.